Analysis of Low-frequency solar Radio Bursts from the solar Corona and their space weather implications

By

Ndacyayisenga Theogene

A thesis submitted in fulfillment of the requirements for the degree of

Doctor of Philosophy in Physics (Space Science)

Department of Physics

School of Science

College of Science and Technology

University of Rwanda

August 2025

Copyright

© 2025 Ndacyayisenga Theogene
All rights reserved. No part of this thesis may be reproduced, stored in a retrieval system, or transmitted in any form or by any means, electronic, mechanical, photocopying, recording, or otherwise, without prior written permission of the author.

Declaration

I declare that this dissertation contains my work except where acknowledged, and it has been passed through the antiplagiarism system and found to be compliant and this is the approved version of the PhD Thesis: **Analysis of Low-Frequency Solar Radio Bursts from the Solar Corona and their Space Weather Implications**.

Ndacyayisenga Theogene, Reg. No: 221030262 Date: October 3, 2025

Name, Registration Number, and signature of the PhD candidate

The PhD Thesis Supervisory Team of Mr. Ndacyayisenga Theogene

Prof. Jean Uwamahoro Date: October 3, 2025

Name and signature of the Main Supervisor

Assistant Prof. K. Sasikumar Raja Date: October 3, 2025

Name and signature of the Cosupervisor

Dr. Jean Claude Uwamahoro Date: October 3, 2025

Name and signature of the Cosupervisor

Dedication

This dissertation is dedicated to my beloved wife and sons whose endless affection, prayers and wishes have been a great source of comfort for me during my whole education period and my life.

Acknowledgments

First, I would like to thank the Almighty GOD, who is the source of all wisdom and knowledge. He has always given me hope and strength in every difficulty that I have encountered throughout my endeavour; without Him, I would not have completed this doctorate. May His name be glorified forever and ever.

I want to sincerely thank my supervisors, Prof. Jean Uwamahoro, Dr. Jean Claude Uwamahoro and Ass. Prof. K. Sasikumar Raja, for their unwavering encouragement, enormous expertise, and assistance throughout my Ph.D. study. This assistance helped me stay on track and make steady progress in scientific studies. They provided me with the necessary tools and skills in this scientific field.

I am grateful to the staff of the Physics Department School of Science, College of Science and Technology of the University of Rwanda for their kind assistance.

I am thankful to the Rwanda Astrophysics, Space, and Climate Science Research Group (RASCRG) for having fully supported my studies, thanks to its collaboration (Grant No. ISP/RWA: 01) with the International Science Programme (ISP) funded by the Swedish International Development Cooperation Agency (SIDA).

Last but not least, I would like to express my deepest gratitude to my beloved wife, Mrs. Claudine Nyirakamana, who has always inspired me with her endless love and unconditional support during the time of writing this dissertation.

ABSTRACT

Space Weather is the term used to describe changes in the space environment around Earth, often occurring within a day or less, driven by solar activity. The most powerful effects arise when massive bursts of solar material known as Coronal Mass Ejections (CMEs) and their shock waves interact with Earth's magnetic field. The extent of impact depends on the speed, size, and magnetic strength of these CMEs. Solar flares also modify the amount of solar radiation reaching Earth's atmosphere, affecting its lower layers. High-energy particles from the Sun, known as solar energetic particles (SEPs), are also a major concern for astronauts traveling to the Moon and beyond. Solar radio observations are essential for space weather research, as solar radio bursts (SRBs) originate from regions where solar flares erupt, SEPs are accelerated, and CMEs are launched. SRBs arise from different altitudes in the solar atmosphere and span wavelengths from millimeters to decameters. Coronal properties such as electron density, magnetic field strength, and turbulence affect the generation of SRBs and vary with both the solar cycle phase and overall solar activity. This study investigated low-frequency SRBs and their space weather implications during the progression of Solar Cycle 25 (SC 25).

Initially, type II SRBs were analyzed alongside their impact on the ionosphere, particularly enhancements in total electron content (TEC) measured through the rate of TEC index (ROTI). Observations were primarily conducted using the Compound Astronomical Low-cost Low-frequency Instrument for Spectroscopy and Transportable Observatory (CALLISTO). A dataset of 32 type II bursts was used to estimate shock and Alfvén speeds, ranging from 504 to 1282 km/s and 368 to 826 km/s, respectively, at heliocentric distances of 1 – 2 solar radii ($R_\odot$). The ambient magnetic field strength, ranging from 7.8 to 0.7 G over this radial span, was modeled as $B(r) = 6.07r^{-3.96}$ G. The analysis showed that 19 of the 32 type II bursts were directly associated with radio blackouts and polar cap absorption events. For the first time, type II bursts were demonstrated to be reliable indicators of subsequent ionospheric irregularities in TEC. ROTI-based assessments revealed that diurnal TEC variability was influenced by the strength of associated solar flares and SEPs, with observed longitudinal variations linked to GPS station locations.

In the second part of the study, 35 geomagnetic storms ($Dst \leq -50$ nT) were analyzed to characterize magnetic activity during SC 25. Correlation between SRBs and geomagnetic disturbances confirmed intense magnetic activity during the cycle's ascending phase. The time delay between

SRBs and CME-driven magnetospheric impacts ranged from 48 to 120 hours, with an average of 79 hours, highlighting the potential of solar radio emissions as forecasting tools. The analysis confirms that space weather responses to geomagnetic storms exhibit event-specific variability, yet ionospheric storm activity remains a persistent feature, independent of geomagnetic storm magnitude.

The third part examined the relationship between SRBs and large SEP events, focusing on their terrestrial impacts. This analysis covered three solar cycles (1997 – 2024) and 122 large SEP events were analyzed. Statistical results showed that SC 25 behaves similarly to SC 23 and exhibits higher activity than SC 24 regarding large SEP occurrences. Velocity dispersion analysis (VDA) revealed that 35 of the 122 SEP events were released either before or concurrently with the peaks of associated GOES X-ray solar flares, without any time lag. The observed correlation between SRBs and SEP events provides insights into the behavior of particle populations driven by solar flares and CMEs. WAVES/STEREO dynamic spectra indicated that 76% of SRBs extended into interplanetary space, demonstrating the dynamics of associated shocks and electron beams propagating along open or quasi-open magnetic field lines.

As a whole, this study underscored the value of SRBs observation for a better understanding of the Sun – Earth interaction dynamics. The ascending phase of SC 25 has been comprehensively monitored and characterized, paving the way for future advancements in space weather modeling and forecasting.

LIST OF PUBLICATIONS

A list of my publications to date is provided below. It is formatted as follows: authors, years, title, journal, volume number, and page number.

1. **Theogene Ndacyayisenga**, J. Uwamahoro, J. C. Uwamahoro, Daniel I. Okoh, K. Sasikumar Raja, A. B. Rabiu, C. Kwisanga, and C. Monstein (2024). Low-frequency solar radio type II bursts and their association with space weather events during ascending phase of solar cycle 25. *A*nnales Geophysae, vol. 42, Page: 312 – 329. https://doi.org/10.5194/angeo-42-313-2024.

2. **Theogene Ndacyayisenga**, J. Uwamahoro, K. Sasikumar Raja, J. C. Uwamahoro, C. Kwisanga and C. Monstein (2024). An Assessment of Solar Cycle 25 progress through observation of SRBs and associated Geomagnetic Storms. *Advances in Space Research*, **73**, Pages 6274 – 6287. https://doi.org/10.1016/j.asr.2024.03.006.

3. **Theogene Ndacyayisenga**, J. Uwamahoro, J. C. Uwamahoro, C. Kwisanga and C. Monstein (2024). Large Solar Energetic Particles and Solar Radio Emissions during Cycle 25. A comparative analysis of trends and characteristics with cycles 23 and 24. *Advances in Space Research*, https://doi.org/10.1016/j.asr.2024.11.060.

Contents

List of Tables

List of Figures

LIST OF ACRONYMS

ACE	Advanced Composition Explorer
AIA	Atmospheric Imaging Assembly
AR	Active Region
AU	Astronomical Unit
CALLISTO	Compound Astronomical Low frequency Low cost Instrument for Spectroscopy and Transportable Observatory
CH	Coronal Hole
CIR	Corotating Interaction Region
CME	Coronal Mass Ejection
SF	Solar Flare
DH	Decametric – Hectometric
Dst	Disturbed storm time
ERNE	Energetic and Relativistics Nuclei and Electron
GLE	Ground Level Enhancement
GMS	Geomagnetic Storm
GNSS	Global Navigation Satellite System
GOES	Geostationary Operational Environmental Satellite
GPS	Global Positioning Satellite
HCS	Heliospheric Current Sheet
HED	High Energy Detector
HF	High Frequency
HMF	Heliospheric Magnetic Field
HMI	Heliospheric Magnetic Imager
HSS	High Speed Stream
IMF	Interplanetary Magnetic field

IP	Interplanetary
Kp	Planetary K index
LASCO	Large Angle Spectroscopic Coronagraph
MHD	Magnetohydrodynamic
NOAA	National Oceanic and Atmospheric Administration
OSF	Open Solar Flux
PCAE	Polar Cap Absorption Event
ROTI	Rate of TEC Index
SC	Solar Cycle
SDO	Solar Dynamic Observatory
SECCHI	Sun Earth Connection Coronal and Heliospheric Investigation
SEP	Solar Energetic Particle
SOHO	Solar and Heliospheric Observatory
SRB	Solar Radio Burst
STEREO	Solar Terrestrial RElation Observation
SW	Solar Wind
SYM-H	SYMetric disturbance in Horizontal field near the equator
TEC	Total Electron Content
TECU	TEC Units
UT	Universal Time
VDA	Velocity Distribution Analysis
VHF	Very High Frequency

LIST OF SYMBOLS

$R_\odot$	Solar Radius
$M_\odot$	Solar Mass
$L_\odot$	Solar Luminosity
G	Gauss
n_p	proton number
m_p	proton mass
Hz	Hertz
MHz	Mega-Hertz
f_p	plasma frequency
N_e	electron density
SFU	Solar Flux Unit
V	Speed
r	heliocentric distance
M_A	Alfvén Mach number
V_A	Alfvén speed
V_S	Shock speed
B	Magnetic field strength
B_z	Component of IMF in Z-direction
$\mathring{A}$	Angstron
MeV	Mega electron Volt
$\frac{df}{dt}$	frequency drift rate
ϵ	solar wind energy input

Chapter 1

General Introduction

1.1 Background

Solar radio bursts (SRBs) are important indicators of solar activity, as they are associated with the sporadic acceleration of large flows of solar plasma triggered by the release of energy stored in magnetic fields [1]. Solar activity refers to the dynamic phenomena occurring on the Sun, driven by its magnetic field. It is indicated by the presence of sunspots (dark regions observed on the solar surface), where a large number of sunspots corresponds to solar maximum, while few or no sunspots indicate solar minimum. Sunspots exhibit an 11-year periodicity in their occurrence, known as the 11-year solar cycle. Figure 1.1 presents a concept map illustrating the solar cycle. SRB emissions from the Sun generally follow a similar pattern or trend in occurrence across the phases of the 11-year solar cycle [3]. The radio observations of bursts provide valuable information about solar plasma properties in the corona through which the bursts propagate [4]. In decimetre – metre wavelength ranges, the SRBs are classified into five different types namely type I through V based on their drift speed and morphology in the dynamic spectra [5]. The rest of this study focused on type II, type III and type IV bursts due to their relevance to space weather phenomena. Type II bursts are characterized by a slow drift from high to low frequencies over time in dynamic spectra, and they usually occur near the peak of associated solar flares (SFs) [6]. In metric wavelengths, solar radio type II bursts are produced by magnetohydrodynamic (MHD) shock waves driven by SFs, coronal mass ejections (CMEs), and fast plasma flows in magnetic reconnection zones. The dynamics of the middle and higher solar corona are studied using the physical parameters derived from metric solar radio type II bursts (e.g., drift rate, duration, starting frequencies). Solar radio type III bursts are fast drift bursts from high to low frequencies in dynamic spectra. They are frequent during the years of high solar activity and are characteristic of electron beams moving along open magnetic field lines [7]. They are released when SFs use

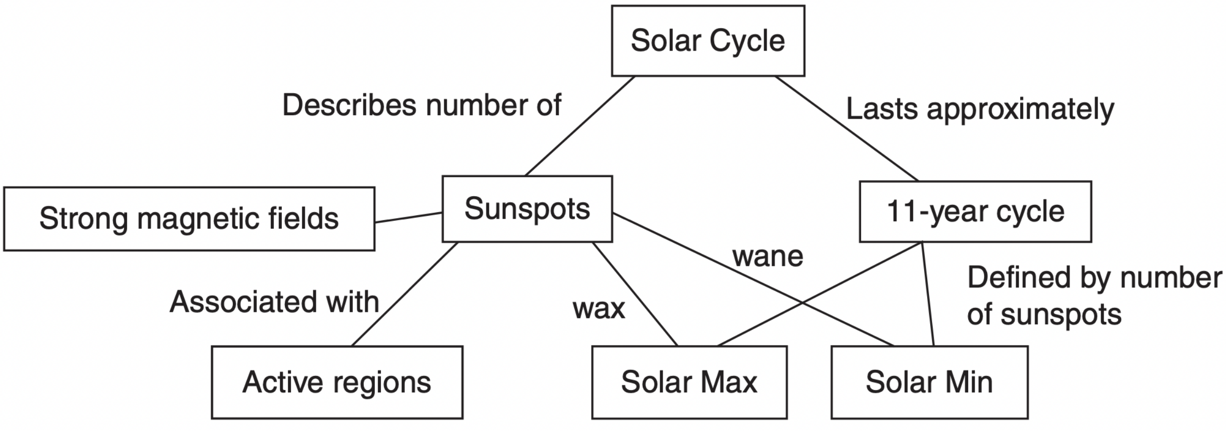

Figure 1.1: A concept map of the solar cycle illustrating how this tool graphically organizes ideas, terms, and concepts. Each box represents a concept, linked by descriptors to definitions, related topics, or to new concepts with their definitions [2].

the plasma process to deliver fast-moving electron beams into the heliosphere [8]. CMEs are frequently accompanied by broadband continuum emissions at decimetric and metric wavelengths, known as type IV radio bursts [9], which can come from stationary or moving sources and use a variety of emission modes [10]. These bursts can be traced using ground-based and space-borne solar radio spectrometers within a wide frequency band [1]. The most pertinent burst types for space weather research are types II, III, and IV since they have strong correlations with space weather hazards such as radio blackouts, solar energetic particle (SEP) storms, and geomagnetic occurrences [4].

Space weather refers to the short-term modulation of the near-Earth space environment by solar activity, typically over time scales of days or less [11]. Space weather originates from the Sun, where a combination of solar events takes place, such as differential rotation, convection, and the dynamo mechanism. The elements of space weather close to Earth's environment include: (i) abrupt magnetospheric compression [12, 13]; (ii) ring current intensification and the occurrence of geomagnetic storms and auroras [14, 15, 16]; (iii) modifications to ionospheric electric fields and currents [17, 18, 19, 20]; (iv) Heating and expansion of the high-latitude upper atmosphere, leading to thermospheric storms [21, 22, 23]; and (v) variations in ionospheric density and temperature, referred to as ionospheric storms [24, 25, 26, 27, 28, 29]. The interaction between SF radiation and ionospheric constituents causes an immediate rise in the ionosphere's overall electron density. The degree of total electron content (TEC) enhancement in the ionospheric region depends on the SF classes [30]. Ionospheric TEC anomalies are typically suppressed by SEP acceleration during the peak of an X-ray SF [31]. The effective flare radiation flux determines how quickly TEC changes over time [32]. The ionospheric D-layer absorbs and blocks high-frequency radio waves, causing significant radio blackouts due to increases in TEC [30]. Radio waves in the ionosphere are used for wireless communication, and radio blackouts affect GPS devices and other wireless communication networks. The National Oceanic and Atmospheric Administration (NOAA) classifies the radio blackouts into five categories as described in Kumar and Singh [33]. Ionospheric disturbances significantly impact Global Navigation Satellite System (GNSS) signals and high-frequency communications. The rate of change of TEC (ROT), expressed in TECU/min ($1\ TECU = 10^{16}\ electrons/m^2$) is an index based on the temporal rate of distinct phase changes in dual-frequency GNSS signals transiting the same ionospheric parcel [34]. ROTI, derived from the standard deviation of ROT, characterizes small-scale irregularities in line-of-sight electron concentration [35]. Significant irregularities are signatures of high solar activity, during which radio interference may affect high-frequency communications, global positioning systems, and other technologies, compared to periods of low solar activity (solar minimum). However, during solar minimum, the primary source of energetic particles in the heliosphere is co-rotating interaction regions (CIRs) [36]. CIRs form when a fast-moving stream of solar wind escapes a coronal hole (CH) and interacts with the Sun's previously produced slow-moving solar wind. This interaction accelerates particles due to shocks, creating a compression area that rotates around the Sun [37]. Another impact on space weather due to explosive events is the production of geomagnetic storms

(GMSs). Geomagnetic storms are transient disturbances in the Earth's magnetosphere caused by interactions of solar phenomena such as coronal holes, SFs, or CMEs [38]. These storms disrupt the intricate processes linking the magnetosphere, ionosphere, and thermosphere. Intense geomagnetic storms ($Dst \leq -100\,nT$) are particularly significant as they can severely affect space missions, high-frequency communications, low-frequency navigation systems, and power grid infrastructures. A GM occurs when strong and long-lived southward interplanetary magnetic fields (IMF) ($B_z \leq -10\,nT$) persist for several hours, enabling effective energy transfer via magnetic reconnection between the solar wind and the Earth's magnetosphere [39].

Solar activity and variations in related parameters affect both interplanetary space and geospace. Consequently, a sequence of processes is triggered, with effects observable at Earth's surface, as illustrated in Figure 1.2. To mitigate these adverse impacts, it is crucial to develop a thorough physical understanding of the process chain, which relies on a combination of observations, data analysis, interpretation, and theoretical or empirical modeling. Solar activity in the current Solar Cycle 25 (SC 25) has exceeded earlier forecasts, with the monthly average sunspot number and F10.7 cm radio flux reaching much higher values than initially predicted [41]. This may indicate the end of the long – term decline in solar activity observed over the past four cycles [42]. After two decades of predominantly mild geomagnetic conditions, SC 25 has shown an increased frequency of eruptive solar events and is likely to produce further geomagnetic storms and potentially severe space weather. In this context, the present study analyzed low-frequency SRBs associated with solar storm events and their implications for space weather as SC 25 progresses.

1.2 Statement of the Research problem

Our current understanding of space weather is still evolving and remains insufficient for reliably predicting solar eruptions [11]. Gaining a comprehensive understanding of the evolution of solar eruptions and constructing a complete picture of the sequence of events from the Sun to the Earth requires the integration of multiwavelength observations, typically obtained from both space-based and ground-based instruments [43]. Solar activity is inherently unpredictable due to the complex magnetic dynamics that propagate from the Sun to Earth. Forecasters depend on early warning observations, one of which is solar radio monitoring from space. However, improving the accuracy of such forecasts requires broader observational coverage, particularly through ground-based radio telescopes.

Of particular interest are low-frequency SRB observations from instruments such as the extended Compound Astronomical Low-frequency Low-cost Instrument for Spectroscopy and Transportable Observatory (e-CALLISTO, https://e-callisto.org/) [44, 45, 46], complemented by space missions. These SRBs are especially valuable because they originate from the same regions of the solar atmosphere where geo-effective disturbances such as solar flare energy releases, particles are accelerated, and CME initiation are likely to occur. This link is supported by the fact that most low-frequency emissions are generated through plasma emission mechanisms [4]. Low-frequency

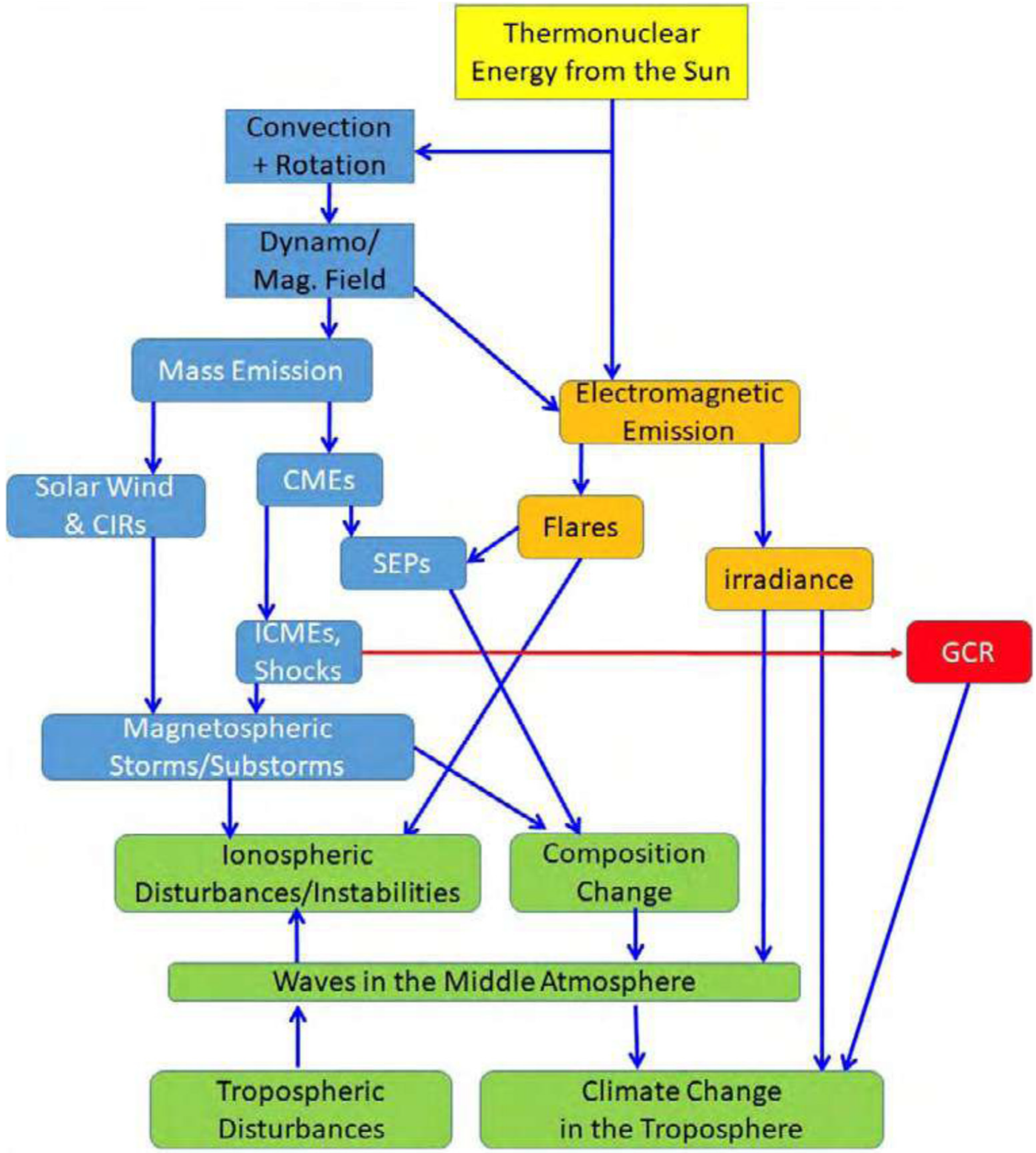

Figure 1.2: Schematic illustrating the primary elements in the chain of physical processes governing solar–terrestrial interaction [40].

SRBs are useful for studying CMEs up to 3 solar radii ($R_\odot$) by enabling the imaging of type II, III, and IV radio bursts during the CME acceleration phase [47, 48, 49]. Additionally, these observations provide insights into electron density and height in the solar corona and allow for the derivation of magnetic field strength [50, 51, 52, 53, 54, 55, 56, 57, 58, 59, 60]. Given that SC 25 was predicted to be stronger than Solar Cycle 24 with some estimates suggesting up to a 30% increase in strength [61, 62]; it became essential to monitor SC 25 activity using low-frequency SRB observations and to assess their implications for space weather forecasting.

1.3 Motivation of the study

Several physical processes associated with space weather such as SFs, SEP events, CMEs, and IP shocks give rise to radio emissions from the solar atmosphere into the IP medium [63, 64, 11]. As SC 25 progresses toward its predicted peak in 2025, more intense space weather conditions were expected, including increased atmospheric drag, intense geomagnetic storms, and more frequent large SEP events compared to those observed during solar minimum phases [65]. Observational data indicated that the number of halo CMEs during the rising phases of SCs 23, 24, and 25 were comparable [66]. Furthermore, forecasts suggested that SC 25 would likely be somewhat stronger than cycle 24. This expected increase in solar activity provided strong motivation to focus the study on SC 25.

1.4 Objective of the study

The main objective of the study was to assess the strength of solar activity as SC 25 progresses, using SRB observations and examining their space weather implications. The specific objectives that supported this main goal were:

- To use low-frequency solar radio type II bursts to diagnose solar activity and associated space weather during the ascending phase of SC 25.
- To analyze geomagnetic activity during the rising phase of SC 25 and its relationship to solar radio emissions.
- To investigate the correlation between solar radio emissions and large SEP events during the ascending phase of SC 25.

1.5 Scope

The study was limited to analyzing low-frequency SRBs as SC 25 progresses, along with their space weather implications. Specifically, recent radio dynamic spectra from e-CALLISTO below 400 MHz and from space missions in the 1–14 MHz range were considered.

1.6 Rationale of the study

SRBs are key indicators of space weather hazards, including radio blackouts, SEP events, and geomagnetic storms. These phenomena significantly impact Earth's atmosphere, disrupting communications, broadcasting, meteorological services, power grids, and satellite-based navigation systems. Accordingly, continuous solar monitoring is critical for timely hazard prediction and mitigation.

This study investigates the utility of SRBs as predictive markers for space weather, supporting the development of early-warning systems. It addresses observational limitations by integrating terrestrial and space-based data, overcoming ionospheric constraints at low frequencies and gaps in space-borne coverage. Furthermore, it examines whether distinct SRB patterns characterize the early phase of SC 25, offering insights for future solar cycle forecasting. Through this approach, the research advances understanding of solar activity and space weather phenomena, contributing to global space science initiatives.

1.7 Structure of the content

This thesis comprises of six chapters, which include an introductory part and a conclusion at the end of each chapter.

1. **Chapter –1: General Introduction**. It is an introductory chapter that describes the research domain, problem, motivation, and objectives of the research.
2. **Chapter 2: Theory and Literature Review.** This chapter discusses the theory and literature related to solar-terrestrial interaction. The Sun, as the primary driver of space weather, is described in detail, followed by an overview of solar activity manifestations namely active regions, sunspots, solar flares, coronal mass ejections, solar energetic particles, solar wind, corotating interaction regions, and geomagnetic storms. The space weather monitoring system is introduced, and solar radio emissions are thoroughly explained, along with the ionospheric background.
3. **Chapter 3: Data and Methods**, describes the data sources and the methods used to process them; arranged according to the objectives of the study.
4. **Chapter – 4** gives and discusses the results of monitoring solar activity using low-frequency solar radio emissions and associated solar storm events. It is build with all the results published in the three papers.
5. **Chapter 5: Space Weather Implications** is primarily about the description of the implications of the low-frequency SRBs analyzed on space weather and their potential for future forecasting.
6. **Chapter – 6** explains the summary and conclusions of the work carried out. Also, future scope of the work and possible recommendations are described in this chapter.

Chapter 2

Theory and Literature Review

The Sun is the major source of heat and light energies in our solar system. The former interacts with the Earth's atmosphere by means of the solar wind (SW). The structure of SW and its constituents undergo disturbances resulting from the interaction of CMEs, leading to ionospheric and magnetospheric disturbances. This section reviews the basics of the Sun and its activity.

2.1 The Sun

The Sun is an ordinary star of spectral type G2V with absolute magnitude of 4.8 and apparent maginitude -27 [67]. G2 means that it is a G-type star of hotness two. G-type stars have prominent H and K lines of Calcium and a yellow appearance. V denotes the luminosity class and it is a class of main-sequence stars. The Sun is brighter than 85% of the stars in our Galaxy [68]. However, it is the only star we have in our immediate vicinity and it is the source of most of the energy that controls physical phenomena in our space environment [67].

The Sun is a magnetically active star, exhibiting fluctuations over timescales that range from fractions of a second to billions of years. The Sun's magnetic field is mainly dipolar and aligned to the rotation axis. Each hemisphere has an opposite dominant polarity as shown in the left-hand panel of Figure 2.1. The middle panel of Figure 2.1 shows the differential rotation of the convection zone which winds up the field lines [69]. The right-hand panel indicates the breaking up of the magnetic loops forming sunspots on the solar surface. The magnetic fields of the Sun play a dominant role in the solar cycle [70].

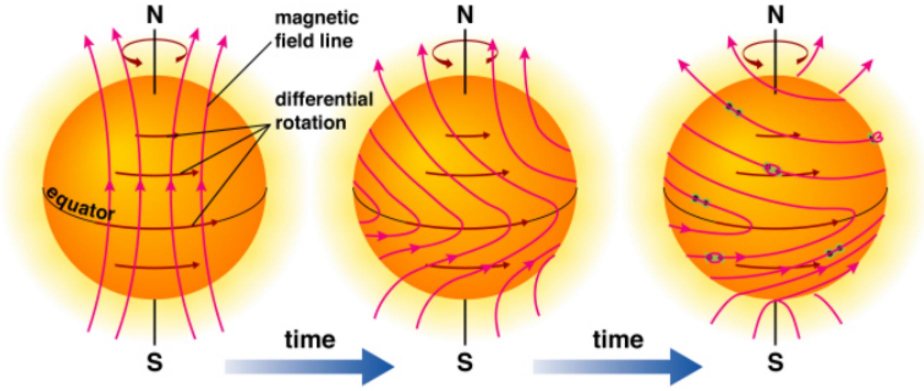

Figure 2.1: Solar magnetic field. Left-hand panel shows the Sun's bipolar field. Middle panel: The magnetic field is being twisted by differential rotation. Right-hand panel: Loops of magnetic field begin to break the surface forming sunspots [69].

2.1.1 General properties and solar parameters

The basic properties of the Sun are known from observations. The Sun is a typical star born 4.5×10^9 years ago. It is a plasma in nature consisting of 92.2% hydrogen and 7.8% helium while 0.1% represents other elements such as Oxygen, Carbon and Nitrogen. The Sun is located at mean distance from Earth of 0.983 – 1.017 AU (1 $AU = 1.5 \times 10^8$ km), with mass, $M_\odot = 1.99 \times 10^{30}\ kg$ (332946 times Earth's mass) – over 99% of the total mass of the solar system. The solar radius is $R_\odot$ = 695,700 km giving a volume of $1.412 \times 10^{27}\ cm^3$ (1.3 million Earths). The visible solar surface (photosphere) has a temperature of 5785 K while its crown has a temperature of $\sim 2 \times 10^6\ K$ with emitted radiation (Luminosity), $L_\odot = 3.86 \times 10^{26}$ W ($3.86 \times 10^{33}\ ergs^{-1}$) [71, 72, 73, 74]. The Sun rotates differentially (see Figure 2.1), it uses 26.8 days at equator (30.8 days at 60° latitude). Due to the dynamo process, magnetic activity may be produced by solar differential rotation [75, 76]. Magnetic phenomena including sunspots, prominences, and brightenings in the solar atmosphere are produced by the twisting of the magnetic field caused by the Sun's differential rotations [77, 78]. The highest magnetic fields in sunspots are typically located within their central black regions or umbrae, where the field is nearly vertical and has typical intensities ranging from 2.5 to 4kG [e.g., 79].

2.1.2 The solar structure

The Sun is not a rigid body but a giant mass of incandescent gas. It is structured into layers with identifiable boundaries. The layers of the Sun are grouped into inner structure and outer structure known as the solar atmosphere. Figure 2.2 illustrates the solar structure with its distinguished layers. The internal structure of the Sun is divided into three layers defined by how energy is transferred through them [80]. At the center is the core where the energy of the Sun is produced by thermo-nuclear fusion of hydrogen to helium. The core is surrounded by the radiation zone followed by the convection zone. Figure 2.3 (a) depicts the cross-section of the internal structure of the Sun and Figure 2.3 (b) indicates the variation of the physical parameters such temperature, density and pressure of the solar interior. The solar atmosphere consists of three layers defined by

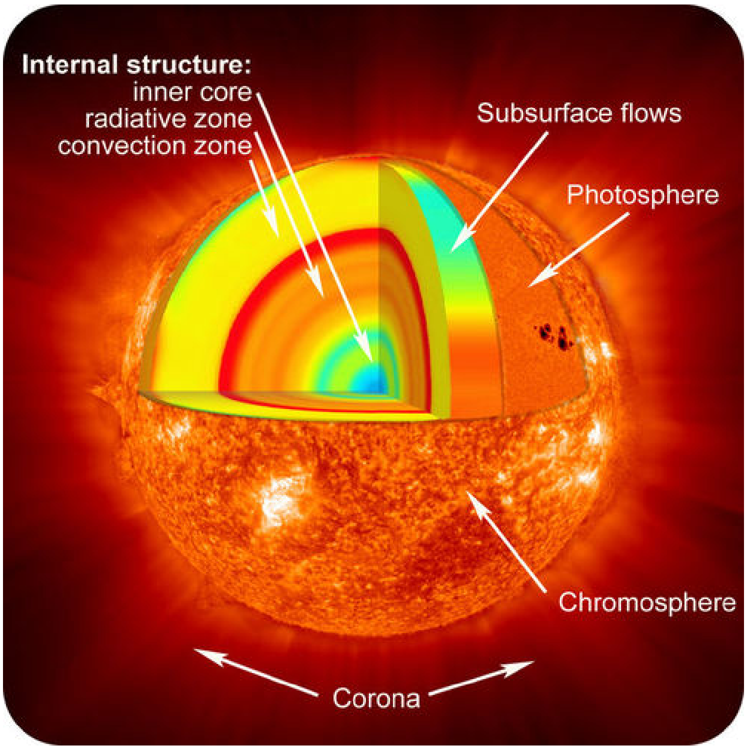

Figure 2.2: Distinguished layers of the Solar structure. Credit: NASA/Goddard.

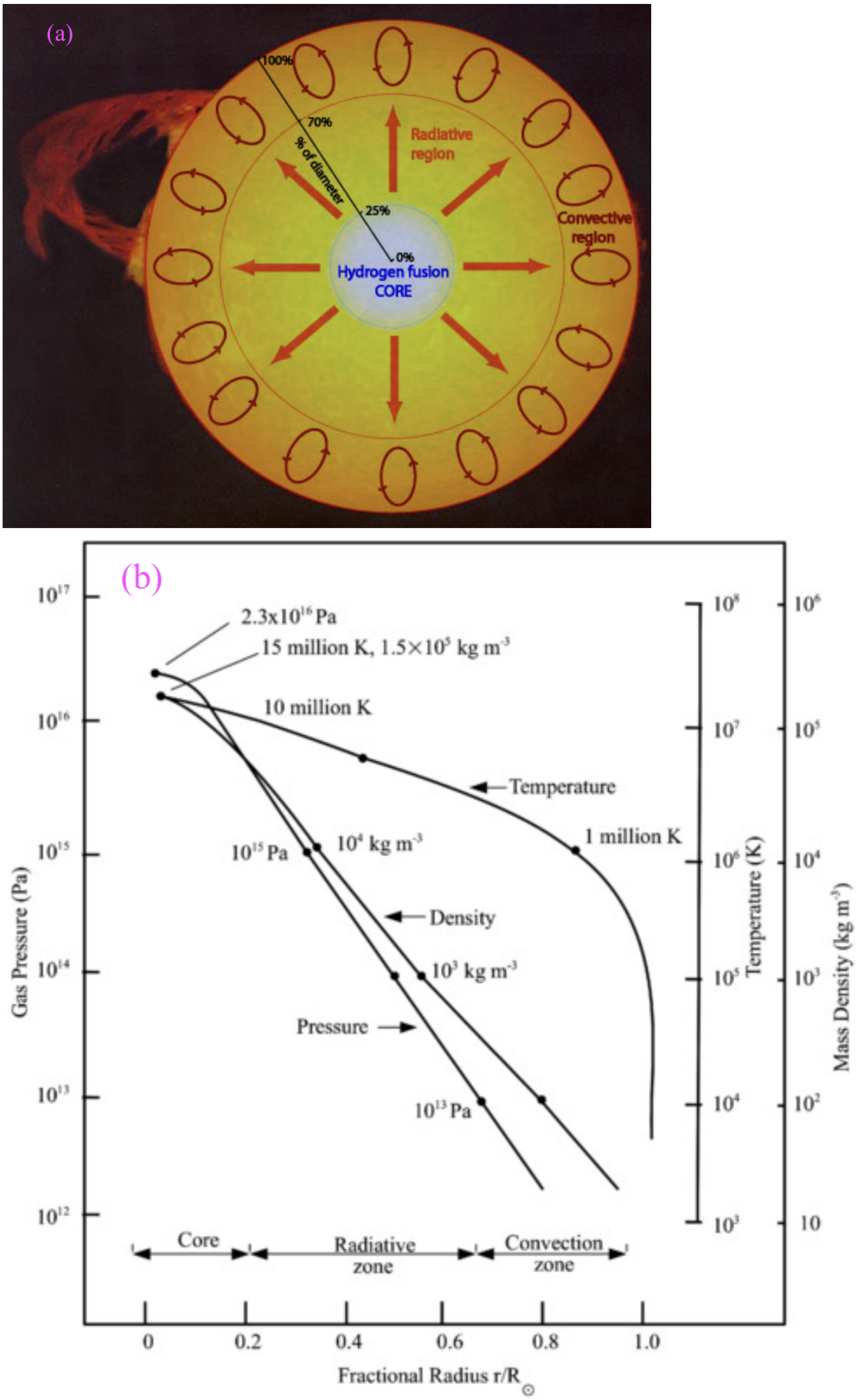

Figure 2.3: (a) A cross-section of the internal structure of the Sun. The energy generated by thermo-nuclear fusion at the core is transported as electromagnetic radiation in the radiation zone while the convective currents in the convection zone transfer the energy to outer parts of the Sun [81]. (b) the variation of temperature, density and pressure of solar interior [82].

their temperature and density, namely, the photosphere, the chromosphere and the corona (refer Figure 2.2). At the top of the convection zone is the photosphere which is the visible solar surface and is covered by granular pattern outlining the turbulent convection cells where the sunlight is emitted [83]. Above the photosphere comes the chromosphere which is about 1500 km thick and is characterized by a temperature higher than that of the photosphere (about 10000 K compare with 5800 K of the photosphere). The chromosphere is a rarer and transparent medium with a density of $10^{17}\ m^{-3}$ [83, 2]. The outer layer of the solar atmosphere is the Sun's crown known as the solar corona. This layer is well observed during the solar eclipse using coronagraphs. It is characterized by a very high temperature (a couple of million degrees), low density but fully ionized plasma [67]. The solar corona is the layer where most of solar explosive phenomena such as active regions for solar flares, coronal mass ejections and radio emissions take place.

2.2 The solar activity and Space weather

The solar activity is characterized by a variety of solar phenomena such as active regions, sunspots, SFs, CMEs and SEPs. The effects of these phenomena on the IP space and on near-Earth's atmosphere is known as space weather. The following subsections briefly discuss the solar phenomena and their subsequent impacts on space weather.

2.2.1 Active regions

The active regions (ARs) refer to the totality of observable phenomena in a 3D volume represented by the extension of the magnetic field from the photosphere to the corona, as revealed by emissions spanning a wide range of wavelengths from radio to X-rays and γ-rays accompanying and following the emergence of strong twisted magnetic flux from the photosphere through the chromosphere to the corona [84]. The NOAA assigns a number to an AR if and only if it has at least one visible sunspot in white light. ARs are the primary cause of a wide range of solar activity phenomena, from minor brightenings and jets to large flares and CMEs.

2.2.2 Sunspots

Sunspots are the locations of strong magnetic field that appear dark on the solar surface. They are usually found in pairs with opposite magnetic polarities within ± 30 degrees of the equator. They are made up of a central dark region called the umbra, which has a typical diameter of 10,000 to 20,000 km, and a brighter region called the penumbra, which has a typical width of 5,000 to 7,000 km [85]. Their typical lifespan is a few days, but it can range from a few weeks to a few months.

2.2.3 Solar Cycle

Solar activity variability leads to the formation of solar cycles, characterized by periodic changes in sunspot numbers [83]. While commonly described as an 11-year cycle, this period represents an average rather than a fixed duration [86]. Cyclic behavior is evident across nearly all solar magnetic phenomena, from small-scale ephemeral regions to large-scale CMEs, with solar cycle signatures detected from the Sun's interior to the heliosphere's outermost boundaries [87]. Moreover, the 11-year periodicity in the number of sunspots and other solar activity is believed to originate from MHD dynamo action at the base of the convection zone [88, 89, 90].

2.2.4 Solar Flares

The solar flares (SFs) represent the sudden and explosive release of energy ($\sim 10^{19} - 10^{25}\ J$) from a localized AR of the Sun in form of electromagnetic radiation across the entire spectrum [91]. SFs affect all layers of the solar atmosphere by heating the plasma to tens of millions of kelvin and accelerating electrons, protons and heavier ions to near the speed of light [92]. They are frequent when magnetic energy builds up in the solar atmosphere is suddenly released. Figure 2.4 displays a flaring region on the solar surface during a sudden release of magnetic energy. Flare emission in the visible domain has been well documented in visible chromospheric lines such as the Balmer and Ca II K lines [93, 94, 95]. In rare situations, SFs can produce enhanced emission at the visible continuum in addition to the enhanced spectral lines created in the chromosphere and above. These flares are known as white-light flares [96]. Thus, white-light (WL) flares are those whose emissions are observable in the optical continuum [97, 98]. The study of WL flares is difficult due to their short duration and low contrast, making observations from Earth infrequent and of poor quality.

Figure 2.4: Schematic diagram of a flaring region from active region on the solar surface. The red and blue lines indicate the magnetic field lines carrying the solar material off the surface. Credit: NASA Marshall Space Flight Center.

2.2.5 Coronal Mass Ejections

The coronal mass ejection (CME) is a large-scale explosion of magnetized plasma from the solar surface. CMEs eject tremendous amount of materials and magnetic fields into heliosphere and they are sources of major geomagnetic storms and IP shocks [e.g., 99, 100]. CMEs are characterized by their speeds, angular widths, and central position angles in the sky plane. Their speeds are often fairly constant over the first few solar radii ($R_\odot$) and range between 300 and 3,000 km/s [101].

The mass and kinetic energy of a CME lie in the range of $5 \times 10^{12} - 5 \times 10^{13}$ kg and $10^{23} - 10^{24}$ J, respectively. A typical CME has a three part structure consisting of a cavity of low electron density, a dense core (the prominence, which appears as a bright region on coronagraph images) embedded in this cavity, and a bright leading edge. Figure 2.5 illustrates an example of a typical CME observed on 10 September 2017 by Large Angle Spectroscopic Coronagraph [LASCO, 102] onboard the Solar and Heliospheric Observatory [SOHO, 103]. CMEs are usually associated with other solar phenomena such as SFs, filament eruptions, shocks, SRBs, and SEPs. Low-frequency SRBs are produced by non-thermal electrons accelerated during the solar eruption process and are associated with CMEs. Such bursts are of particular interest because they are associated with energetic CMEs that propagate through the IP medium and, if Earth-directed, have an impact on the Earth's environment [104]. Solar observations showed that CMEs that appear to surround the occulting disk of the observing cronagraphs are known as halo CMEs (HCMEs) and have the highest probability of impacting the Earth's magnetosphere [105] when they orginate from the visible solar disc and are Earth-directed. Halo CMEs are more energetic than other CMEs with average speed of ~ 1000 km/s, and are very important in space weather research [106]. Full halo CMEs (FHCMEs) have an apparent width $W = 360°$, while partial halo CMEs have a width of $120° < W < 360°$. Halo CMEs occurring on the frontside of the Sun are a potential source of geomagnetic storms because they can directly impact Earth's magnetosphere with high kinetic energy [107, 108]. The geoeffectiveness of HCMEs is determined by the presence of a southern component of the magnetic field in the sheath and/or ejecta regions. Geoeffectiveness is defined as a CME's ability to cause a geomagnetic storm. HCMEs associated with intense geomagnetic storms ($Dst \leq -100$ nT) are generally located within a longitude range of $\pm 45°$ (average longitude $\sim W10$), whereas non-geoeffective halos ($Dst > -50$ nT) had a broad longitude distribution

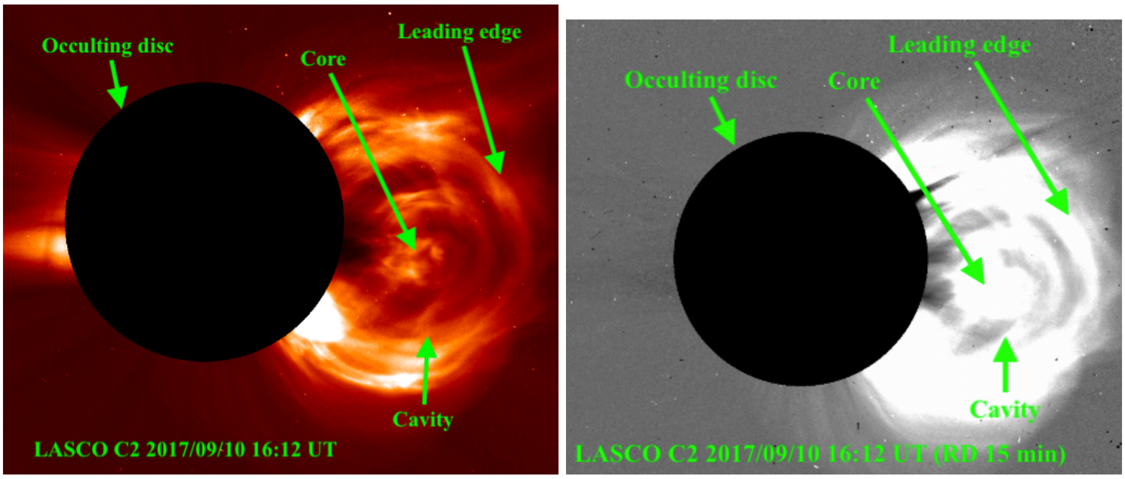

Figure 2.5: A huge coronal mass ejection of 10 September 2017 taken with the Large Angle Spectrometric Coronagraph (LASCO) on the Solar and Heliospheric Observatory (SOHO). (a) Original image in the LASCO C2 field of view and (b) its corresponding 15 minute running difference image. The black area corresponds to the occulting disk of the space-borne telescope, called coronagraph, that blocks intense sunlight and permits the tenuous, million-degree corona to be seen. The three essential parts of the CME are indicated in both images.

(±90°) [108].

2.2.6 Solar Energetic Particles

Solar energetic particles (SEPs) are primarily energetic protons, electrons, and heavy ions that are energized during solar coronal eruptive events such as SFs and CMEs. SEPs are the most dangerous aspects of space weather because they cause increased radiation dose rates for humans in space and high altitudes in the atmosphere, as well as changes in the ionosphere, which cause a variety of effects, including high frequency radio blackouts on polar airline routes [e.g., 109, 110, 111, 112].

2.2.7 The Solar Wind

Plasma from the solar corona, the Sun's heated, extended atmosphere, is continuously expelled under pressure and is known as the solar wind (SW) [113]. The heliosphere, an interstellar bubble shaped by the Sun that stretches far beyond the outer planets, is sculpted by the SW. A fundamental component of space weather [114], the heliospheric magnetic field is created when the out-flowing SW plasma pulls the coronal magnetic field with it. It is also the only stellar magnetic field that can be measured directly. For decades, two types of SW have been identified at solar minimum: fast wind from coronal holes and slow wind from streamer belt regions [115]. Figure 2.6 shows the basic types of the SW and their solar sources in the solar atmosphere. The

SW is supersonic, traveling from the Sun to Earth in about 4 days with an average speed of 400 km/s. Table 2.1 summarizes the SW mean properties at the Earth's orbit, namely in the ecliptic plane at a heliocentric distance of 1 AU. While SW velocity and density are greatly variable, particle flow remains rather stable. The SW flow pulls the coronal magnetic field outward, causing previously closed loops to 'open' and contribute to the heliospheric magnetic field (HMF). The

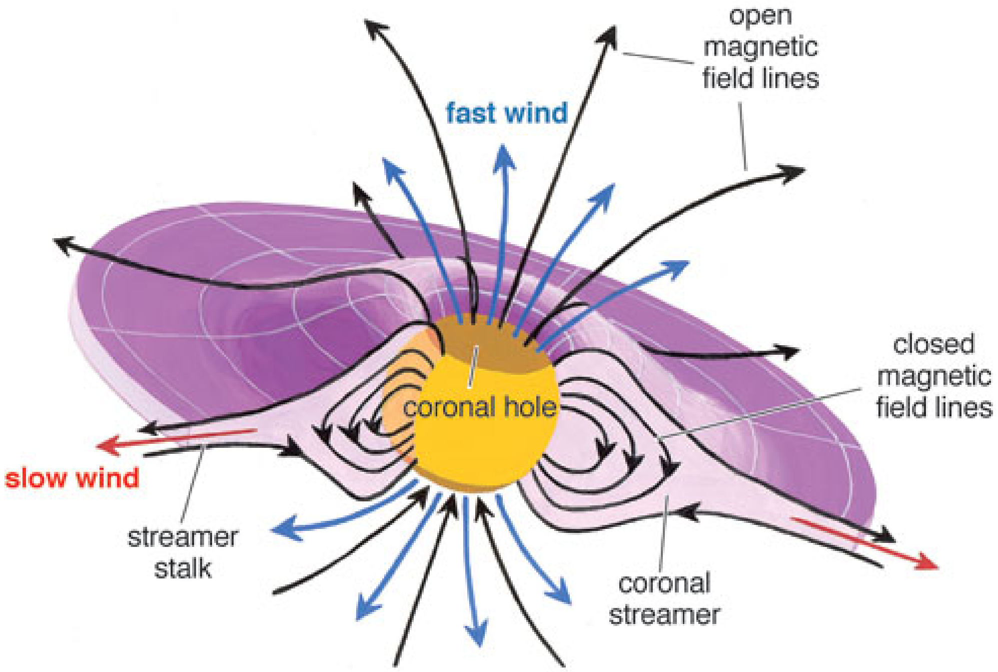

Figure 2.6: Fast wind blows out from the coronal holes (open field lines). Slow wind – from the coronal streamers, above the closed field lines and along the heliospherical current sheet.

Table 2.1: Averaged solar wind parameters at 1 AU during solar activity minimum conditions, compiled by Schwenn [116].

Parameter	**Low speed wind (LSM)**	**Fast wind (HSS)**
Flow speed v_p	$250 - 400 kms^{-1}$	$400 - 800 kms^{-1}$
Proton density n_p	10.7 cm^{-3}	3.0 cm^{-3}
Proton flux density $n_p v_p$	$3.7 \times 10^8 cm^{-2} s^{-1}$	$2.0 \times 10^8 cm^{-2} s^{-1}$
Proton temperature T_p	3.4×10^4 K .	2.3×104K
Electron temperature T_e	1.3×10^5 K	1×10^5 K
Momentum flux density	$2.12 \times 10^8 dynecm^{-2}$	$2.26 \times 10^8 dynecm^{-2}$
Total energy flux density	$1.55 ergcm^{-2} s^{-1}$	$1.43 ergcm^{-2} s^{-1}$
Helium content n He /n p	2.5%, variable	3.6%, stationary

HMF pervades the solar system and defines the magnetic effect of the Sun, also known as the heliosphere. The ”open solar flux” (OSF) is the integrated coronal magnetic flux that contributes to the HMF (i.e., the total coronal flux that passes through the source surface). The strength of the Sun’s dipolar magnetic field component [117] determines the magnitude of the OSF since it decays more slowly with distance from the Sun than the higher-order magnetic field moments. When OSF from separate coronal holes (or from different regions of the same coronal hole) converges, a helmet streamer forms, as illustrated schematically in Figure 2.7. If OSF from coronal holes of opposite polarity converges, large helmet streamers are produced [118, 119, 120]. Thus, helmet streamers will contain the sunward edge of the heliospheric current sheet (HCS, [121]), which surrounds the Sun. Streamers form a ”belt” around the Sun. Smaller ”pseudostreamers” [122] are formed instead when flux from coronal holes with the same polarity converges. The Sun’s mass loss rate can be estimated using the particle flow [123]:

$$\frac{dM_\odot}{dt} \simeq n_p \mu m_p 4\pi \left(1AU\right)^2 > 10^9 kg/s \tag{2.1}$$

where $M_\odot$ stands for the solar mass, n_p is the proton number density, μ is the velocity and m_p is the proton mass, respectively. This means that the Sun loses over a million tonnes of mass every second through the SW. The Sun’s mass ($M_\odot \simeq 2 \times 10^{30}$ kg) makes this loss insignificant.

2.2.8 Corotating interactive regions (CIRs)

During a solar minimum, another form of solar/coronal event dominates. During this phase, coronal holes have grown from their polar locations to stretch into, and sometimes across, the equatorial regions. These solar regions emit fast (750 – 800 km/s) and tenuous plasma. These regions appear to ”corotate” with the Sun due to their long lifespan and slow evolution [123]. The interaction of this fast wind with slower, denser streamer wind, forming a corotating interaction region (CIR), produces geoeffective field compressions and deflections [83]. Three significant

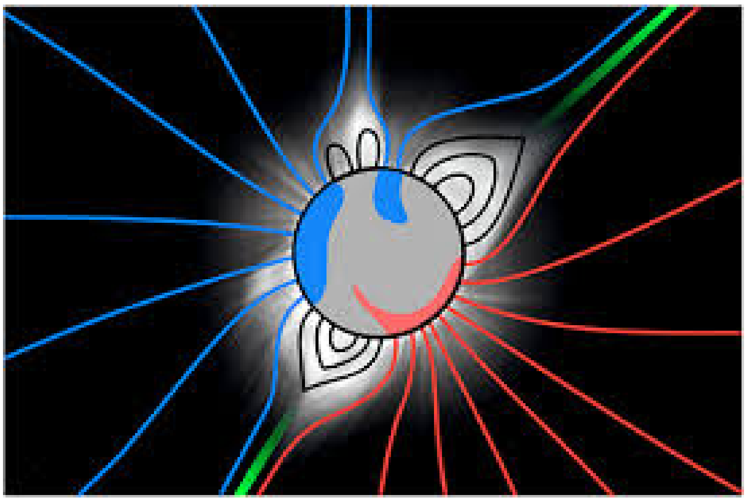

Figure 2.7: Background: A white-light eclipse view of the corona, with brighter areas indicating higher plasma density. Foreground: A schematic of the coronal magnetic field in the sky. The blue and red lines represent inward and outward polarity open solar flux. Coronal holes are indicated by the blue and red darkened patches on the solar disc. Closed coronal loops are indicated by the black lines. The green line represents the point at which the heliospheric current sheet intersects with the sky. It is contained between two (dipolar) helmet streamers. A third ”pseudostreamer” near the northern pole (top of the image) is formed by the convergence of open flux with the same polarity and hence lacks a current sheet. Image and description adapted from [120].

effects of these structures and the shocks they cause are as follows: first, they may act as barriers to cosmic rays, preventing them from penetrating the inner heliosphere; second, they accelerate particles to extremely high energies; and third, they cause disturbances at Earth [124].

2.2.9 Geomagnetic storms

Geomagnetic storms are large-scale disturbances resulting from interactions between the Earth's magnetic field and magnetized plasma ejected from the Sun, during which significant amounts of energy are transferred to the magnetosphere. Although the effects of geomagnetic storms vary depending on the characteristics of each event, several common outcomes are typically observed. These include compression of the dayside magnetosphere [125, 126], strengthening of magnetospheric currents [127, 128], variations in the radiation belts such as particle depletion and enhancement [129, 130, 131], increased particle precipitation in auroral regions [132, 133], and alterations in ionospheric dynamics and geomagnetically induced currents on Earth's surface [134, 135]. This widespread and rapid transfer of energy can significantly affect technological systems, leading to satellite malfunctions, communication outages [136], radio signal interference, GPS disruptions, and increased radiation exposure that may endanger high-altitude and high-latitude missions.

Geomagnetic storms are typically classified based on their impact on the magnetosphere, which is assessed by analyzing disturbances recorded by ground-based magnetometers at various latitudes around the Earth. These measurements are processed into indices, such as the Disturbance Storm Time (Dst) index. The Dst index reflects low-latitude, ground-level magnetic perturbations recorded at four observatories: Hermanus (South Africa), Kakioka (Japan), Honolulu (Hawaii), and San Juan (Puerto Rico). It serves as a proxy for the strength and development of the magnetospheric ring current and is widely used to determine the severity of geomagnetic storms [14, 83]. Generally, the more negative the Dst value, the more intense the geomagnetic storm. Figure 2.8 illustrates the magnitude of the Dst variation during the large geomagnetic storm that occurred between 10 and 12 October 2024.

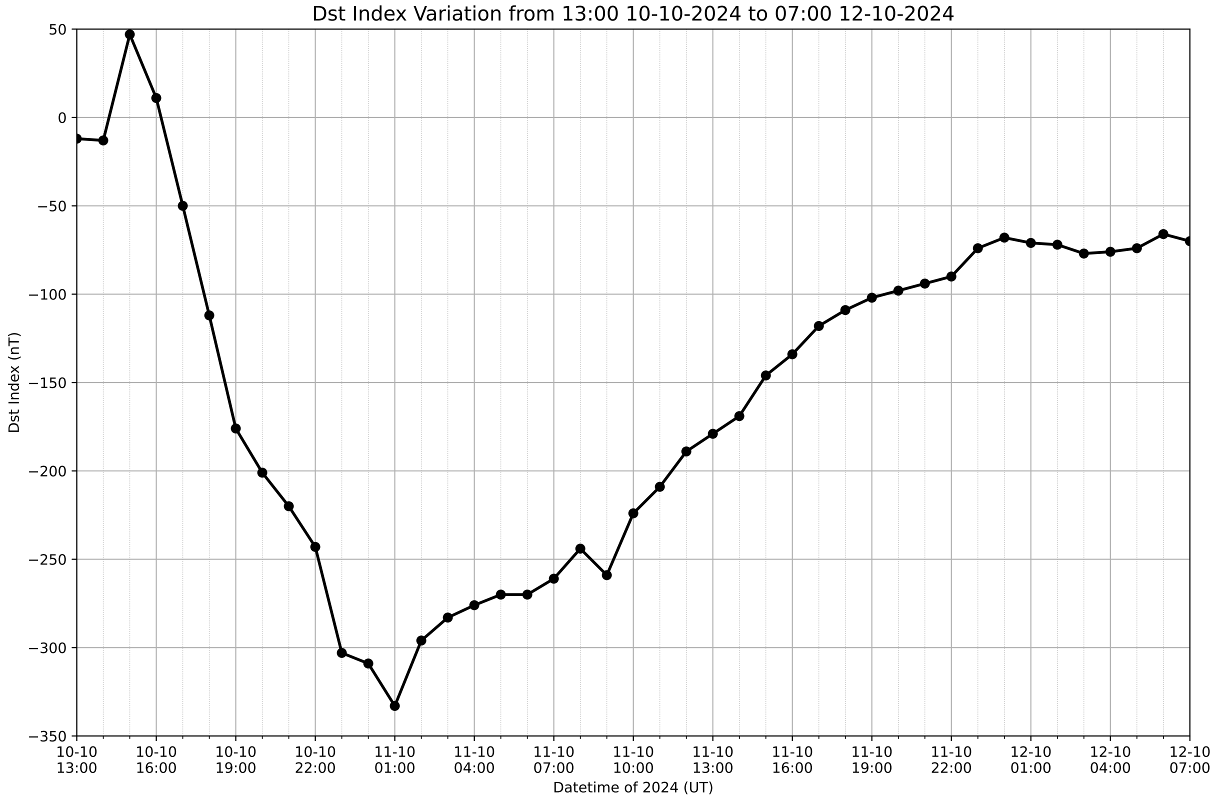

Figure 2.8: An intense geomagnetic storm took place on 10 – 12 October 2024, reaching a minimum Dst of - 335 nT.

2.3 Space Weather Monitoring

The study of conditions in the space environment that can affect life on Earth particularly the increasingly sophisticated technologies that are part of modern society is referred to as space weather. Solar radio observations are important for understanding these phenomena because they are typically triggered by events in the solar atmosphere, such as flares, CMEs, and shocks, which generate electromagnetic and particle radiation that can impact Earth [4]. Space weather is monitored through direct measurements from both ground- and space-based facilities. Geomagnetic indices, derived from various ground-based magnetometers, are used to quantify the effects of solar phenomena on Earth's magnetic environment. For a detailed description of geomagnetic indices and their physical significance, see, Menvielle and Marchaudon [137] and Menvielle et al. [138], and references therein. All information about these indices is also available on the following websites: http://isgi.unistra.fr/ and/or http://wdc.kugi.kyoto-u.ac.jp/. The Sun-Earth Connection Coronal and Heliospheric Investigation (SECCHI [139]) on the Solar TErrestrial Relations Observation

(STEREO) [140, 141] spacecraft allows for direct observation of CMEs. With current technological advancements, space scientists are now able to predict space weather hazards. For example, at the Solar Influences Data Analysis Center (SIDC) in Brussels, Belgium, software for the automatic detection and tracking of halo CMEs has been developed using white-light coronagraph images from SOHO/LASCO (see: `http://sidc.oma.be/cactus`) [102]. Other space missions include Advanced Composition Explorer (ACE) [142], Geostationary Operational Environment Satellite (GOES), Magnetospheric Multiscale [143] and many others. The relationship between various Space Weather processes that originate from the Sun and their impacts are depicted in Figure 2.9 [144]. Certain processes originate and develop in IP space. ARs [84] and coronal holes (CHs [145]) are the two main solar sources of space weather. On the solar surface, ARs are a complicated collection of sunspot magnetic fields of different polarity. The magnetic loops that extend above the surface are coupled to the different magnetic polarities. Changes in the magnetic field interconnections (magnetic reconnection) cause magnetic annihilation and a sudden release of energy in the form of a SF as a result of the growth of the AR substructure and underlying subsurface dynamics [146, 147]. Most Space Weather effects have solar origins that are primarily connected to a few major classes of phenomena: the solar eruptive phenomena, such as CMEs, SFs, and erupt filaments, are associated with the dynamic processes of magnetic field reconfiguration, or magnetic reconnection, and energy release in ARs of the Sun. Variabilities in solar irradiance

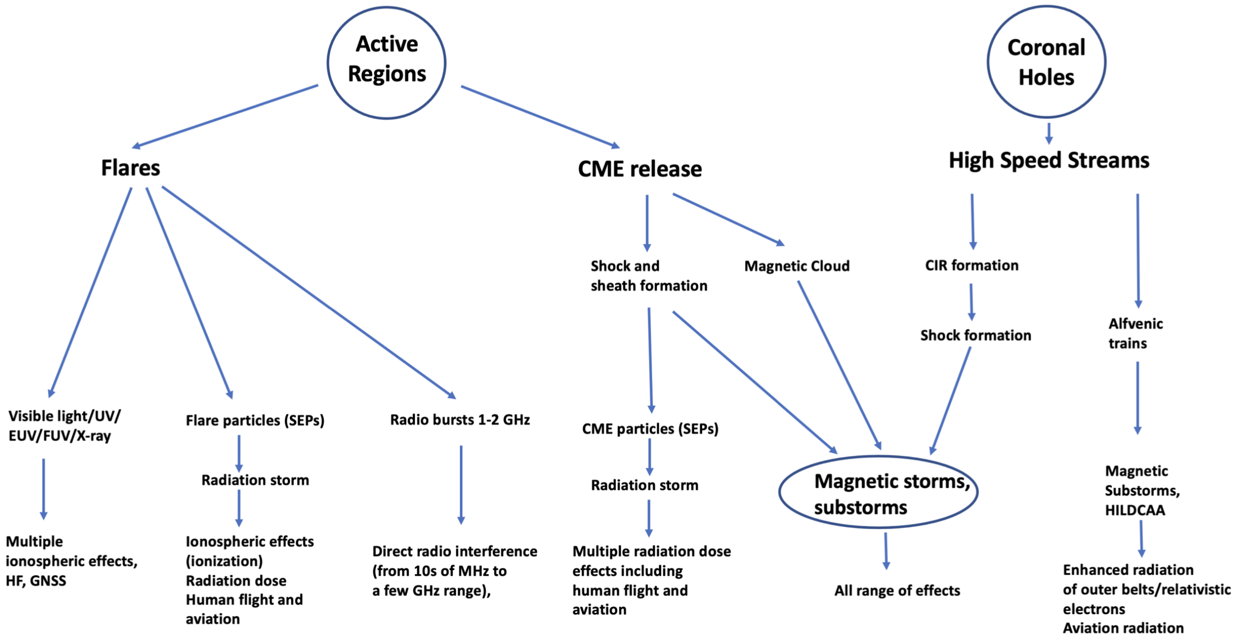

Figure 2.9: The relationship between the primary space weather processes solar eruptive processes and high speed SW and the effects and impacts of space weather (note that while most energetic eruptions from active regions are responsible for CMEs and flare events, filament eruptions in quiet regions and at polar coronal hole boundaries can also be a contributing factor). Due to their intimate relationship with eruptive processes, several Space Weather events and impacts may occur simultaneously, but they may also occur separately, for example, radiation storms and geomagnetic storms [144].

resulting from magnetic convection and 27-day solar rotation, including significant spectral bands of ultraviolet (UV, 120 – 400 nm) and extreme ultraviolet (EUV, 10 –120 nm) emissions; solar coronal holes from which high speed streams (HSSs) of SW emanate. In IP space, HSSs interact with slow-moving streams to form large-scale compressive structures known as CIRs [148]. Figure 2.10 illustrates space weather impacts on ground- and space-based technology. Solar radio observations of bursts relevant to space weather are also made by ground- and space-based radio telescopes. Many ground-based radio telescopes have been built to improve SRBs observation, these include the Radio Solar Telescope Network (RSTN) operated by U.S. Air Force [149], the Hiraiso Radio Spectrograph (HiRAS) in Japan [150], ARTEMIS-IV in Greece [151], IZMIRAN in Russia [152], Gauribidanur Low-frequency Solar Spectrograph (GLOSS) in India [153], e-CALLISTO. In decameter wavelength: Nançay Decametre Array [154], the Ukrainian T-shape Radio telescope model 2, UTR-2 [155, 156], the Ukrainian Radio Interferometer of NASU, URAN [157, 158], and many others (https://www.astro.gla.ac.uk/users/eduard/cesra/?page_id=187). Two space missions provide radio observations below the ionospheric cutoff. That is the WAVES

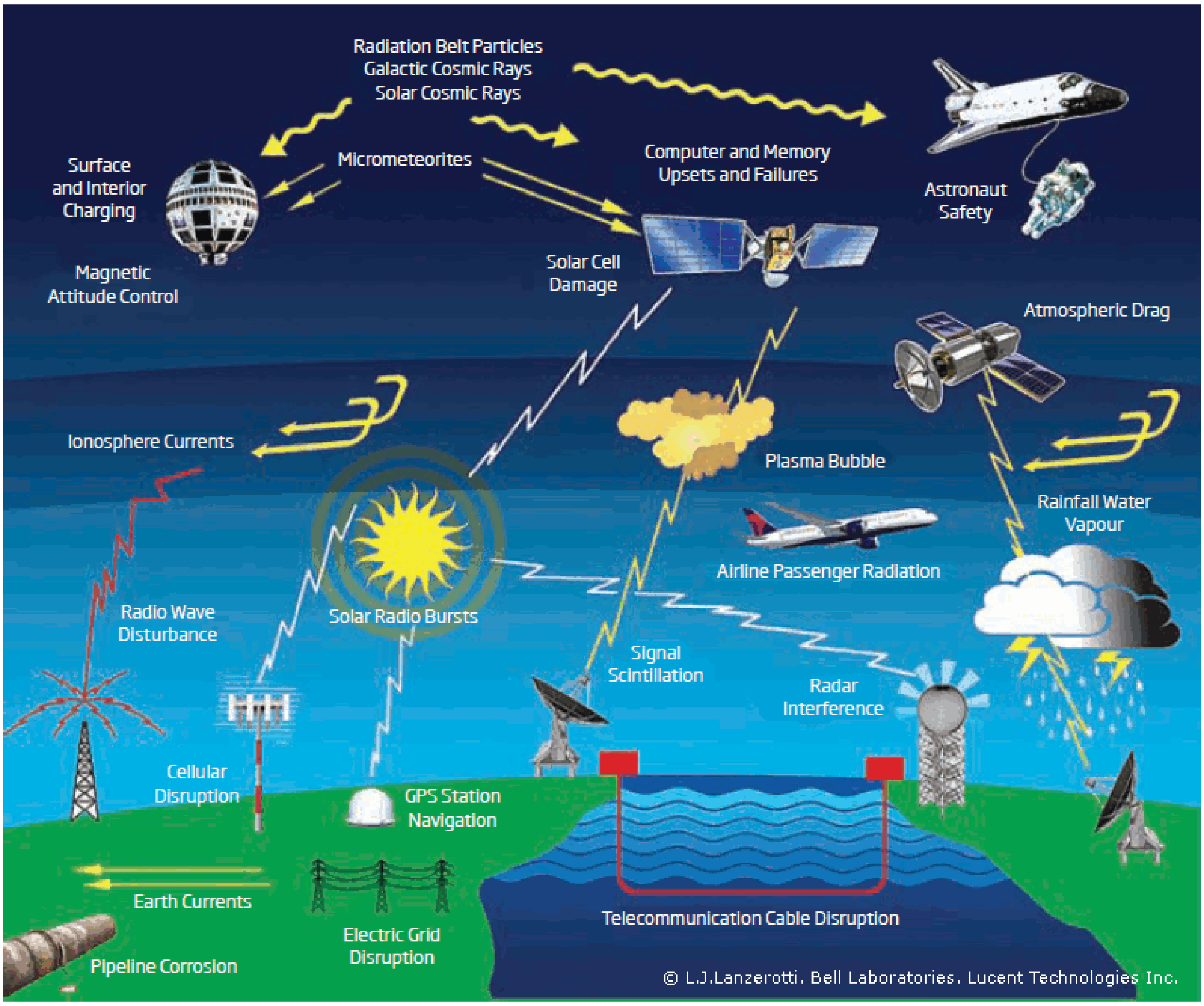

Figure 2.10: Illustration of various solar-terrestrial impacts on ground- and space based technology. Source: https://www.sansa.org.za/2021/11/05/an-inside-view-how-the-24-7-operational-space-weather-centre-will-work/.

onboard WIND spacecraft [159] and WAVES onboard STEREO specraft [140, 141]. Predicting the space weather impact of solar events before the first signature of the solar event is observed is currently impossible. SRBs, on the other hand, are among the first signs of an eruptive event in the solar corona [160].

2.4 Solar Radio Bursts

Radio emissions from the solar atmosphere to IP space are caused by a variety of physical phenomena with space weather implications [e.g., flares, SEPs, CMEs and shocks, 63, 64, 11]. This section discusses emission mechanisms and classifications of SRBs.

2.4.1 Radio Emission Mechanisms

Different emission mechanisms are responsible for producing different wavelengths of the radio and microwave bands across the electromagnetic spectrum. These radio emission mechanisms are primarily dominated by free electrons, either in a thermal or non-thermal distribution. Based on the phase association of these electrons with the emitted photons, radio emission is further classified as coherent or incoherent in nature. The study focused on the coherent emission mechanism which consists of photons that are emitted in phase from accelerated electrons and work together to initiate the emission. This mechanism includes electron – cyclotrom maser [161] and plasma emission. The rest of the study involved the plasma emission mechanism because of its relationship with radio parameters.

Plasma emission is a coherent emission mechanism that generates electromagnetic radiation from Langmuir waves. The involvement of Langmuir waves, produced by fast electrons, is the key feature; thus, the emission occurs at the plasma frequency (f_p) or its second harmonic ($2f_p$). Melrose [162] and Tsytovich and ter Haar [163] summarize the proposed plasma emission mechanism, although refinements and modifications continue to be proposed [e.g., 164, 165, 166]. Figure 2.11 illustrates the stages of the plasma emission mechanism. Electron beam propagating through the coronal or SW plasma generates Langmuir waves, which evolve by either decaying to ion-sound waves or scattering off plasma ions, both of which generate backwards propagating (negative wavenumber) Langmuir waves. These may then combine with a wave from the forwards spectrum to produce an electromagnetic wave with twice the plasma frequency. Alternatively, an ion-sound wave and a Langmuir wave may interact, or a Langmuir wave may be directly scattered by an ion into an electromagnetic wave, both of which produce emission at the local plasma frequency (f_p). The formula below can be used to estimate the plasma frequency (f_p)

$$f_p = \frac{e}{2\pi}\sqrt{\frac{N_e}{\epsilon_0 m}} \tag{2.2}$$

where, N_e is the electron density of the medium [m^{-3}], e is the charge of the electron [$\approx 1.60217 \times 10^{-19}$ C], m is the mass of the electron [$\approx 9.1 \times 10^{-31}$ kg], ϵ_0 is the permittivity of the free space

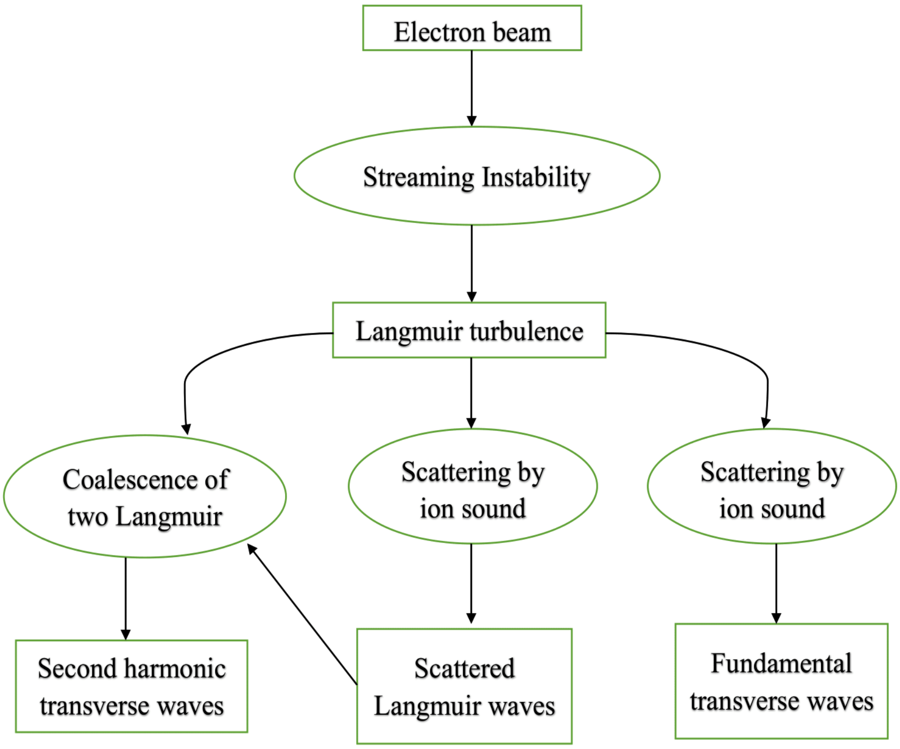

Figure 2.11: The stages of the plasma emission mechanism (adapted from [165]).

[$\approx 8.8542 \times 10^{-12}\ F/m$]. By plugging in these values in Equation 2.2 leads to

$$\begin{aligned} f_p[Hz] &= 8.98 \times \sqrt{N_e[m^{-3}]} \\ &= 8.98 \times 10^3 \sqrt{N_e[cm^{-3}]} \end{aligned} \tag{2.3}$$

2.4.2 Radio bursts characteristics and classification

The study of SRBs is fascinating because the various types reveal different information about the processes involved [167, 168]. There is a wealth of literature on SRBs. General overviews are provided in Krueger [169], McLean and Labrum [5], Zheleznyakov [170], while the theoretical background is given in Befki [171], Benz [172], Kaplan and Tsytovich [173], Melrose [162, 174], Rybicki and Lightman [175], Zheleznyakov [176]. The various events produce radio emissions with varying spectral flux densities and at varying coronal heights. In radio astronomy and solar radio astronomy, the Jansky ($1\ Jy = 10^{-26}\ Wm^{-2}Hz^{-1}$) and solar flux unit ($1\ SFU = 10^4\ Jy$) units of flux density are used. The pioneers of solar radio astronomy established the classification of solar radio bursts. There are five types of solar radio bursts. Types I-V bursts are named after Wild and McCready [177], Boischot [178], and Wild et al. [179], respectively. Table 2.2 summarizes the characteristics of these types of radio bursts, with a detailed explanation provided by Warmuth and Mann [167], and the dynamic radio spectra of various solar radio bursts shown below were obtained using e-CALLISTO.

Table 2.2: Characteristics of solar radio bursts classes. Source: https://www.sws.bom.gov.au/World_Data_Centre/1/9/3.

TYPE	CHARACTERISTICS	DURATION	FREQUENCY RANGE	ASSOCIATED PHENOMENA
I	Short, narrow-bandwidth bursts, usually occur in large numbers, with underlying continuum	Single burst: $\sim 1\ s$ Storm: hours – days	80 – 200 MHz	CMEs, flares, eruptive prominences
II	Slow frequency drift bursts Usually accompanied by (usually stronger intensity) second harmonic	3– 30 minutes	Fundamental: 20 – 150 MHz	Flares, proton emission, magnetohydrodynamic shockwaves
III	Fast frequency drift bursts Can occur singularly, in groups, or storms (often with underlying continuum). Can be accompanied by second harmonic	Single burst: 1 – 3 s Group: 1 - 5 minutes Storm: minutes – hours	10 KHz – 1 GHz	Flares, CMEs
IV	**Stationary Type IV**: Broadband continuum with fine structure	Hours – days	20 MHz – 2 GHz	Flares, proton emission
	Moving Type IV: Broadband, slow frequency drift, smooth continuum	30 – 2 hours	20 – 400 MHz	Eruptive prominences, magnetohydrodynamic shockwaves
	Flare continua: Broadband, smooth continuum	3 – 45 minutes	25 – 200 MHz	Flares, proton emission
V	Smooth, short-lived continuum Follow some type III bursts Never occur in isolation	1 - 3 minutes	10 – 200 MHz	Same as type III bursts

2.4.3 Type I bursts

Type I emissions, also known as noise storms, are made up of a continuous component and short-duration, narrowband bursts i.e., $\Delta f/f \leq 1$, that can occur together or separately [180]. They are highly polarized ($\sim 100\%$) in the O-mode and appear to be at the fundamental of the local plasma frequency. Melrose [181] proposed a model with fundamental emission and negligible second harmonic. A summary of the theory of Type I storms is given in Kundu and Gergely [182], while a summary of previous attempts to explain solar noise storms is provided in [183].

2.4.4 Type II bursts

First identified by Payne-Scott et al. [184], type II radio bursts are some of the most intense solar radio emissions detected at metric wavelengths [e.g., 177]. These emissions are now widely understood to be triggered by MHD shock waves produced by SFs, CMEs, or rapid plasma flows within magnetic reconnection regions [e.g., 185, 186, 187, 188, 189, 59, 190, 47, 191]. MHD shocks have been observed in connection with type II radio bursts across a range of wavelengths: metric (m) [e.g., 177, 192, 193, 194], decametric-hectometric (DH) [51], and kilometric (km) [195]. At metric wavelengths, type II bursts serve as the earliest indicators of shock formation in the solar corona and can be detected by ground-based telescopes operating in the 300–30 MHz frequency range. However, due to the Earth's ionospheric cutoff, radio waves below a certain frequency cannot reach the ground, making it necessary to use space-based instruments to detect

DH-range type II emissions. For example, the WIND/WAVES instrument detects type II bursts across 20 kHz to 14 MHz, covering DH and km wavelengths [196, 197, 198]. These shock waves are used to classify the different types of type II bursts. The connection between CMEs and metric type II bursts (m-type II) remains controversial [199, 200, 201], though Sheeley et al. [202] supported the hypothesis that m-type II bursts are caused by blast waves. Vršnak [203] discovered a strong relationship between SF characteristics and radio type II parameters. Figure 2.12 presents an example of the dynamic spectrum of a solar radio m-type II burst event observed by the CALLISTO station in RWANDA on 22 August 2015. The event began at 06:52 UT and ended at 06:58 UT, lasted 6 minutes. According to the dynamic spectrum, it was observed within the frequency range of 73 - 44 MHz. The event was linked to an M1.4 flare class that occurred at 06:49 UT and was located on the solar disc at 15S20E. It was also linked to a CME that occurred at 07:12 UT with a speed of 643 km/s and a height of $r = 1.5\ R_{\odot}$ ($R_{\odot} = 695700\ km$) [204]. The physical characteristics of m- type II radio bursts, such as drift rate, starting frequency, and duration, provide insights into the dynamics of the middle and upper solar corona. Electron beams accelerated by shock waves driven by CMEs generate type II bursts in the DH and km wavelength ranges [e.g., 205, 196, 206]. Halo CMEs associated with DH-type II bursts are generally more energetic and have a greater impact on Earth than those linked to m-type II bursts [207, 208, 209]. According to Reiner et al. [210], there is a correlation between the speeds of DH-type II radio bursts and the velocities of associated CMEs. Pohjolainen et al. [211] hypothesized that wide-band type II bursts are linked to fast halo CMEs. They found that 72% (18 out of 25 events) of these

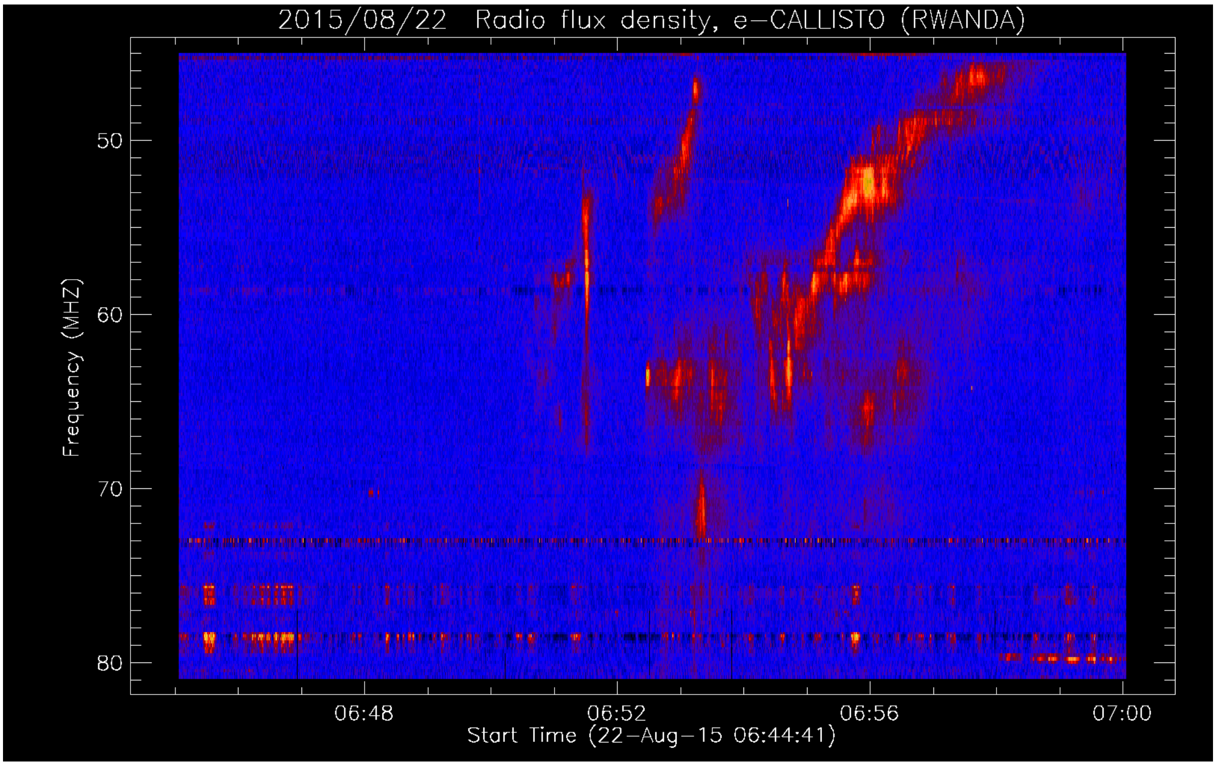

Figure 2.12: The dynamic spectrum of 22 August 2015 solar radio type II burst observed by CALLISTO station in RWANDA which is part of global e-CALLISTO network. The type II burst shows a clear band splitting of fundamental and second hormonic.

bursts occurred at heights corresponding to the leading edge of the CME, suggesting that they were produced by the bow shock in front of the CMEs. The remaining events were discovered to have much lower heights than the CME fronts, revealing a different type of height-time evolution. Type II dynamic spectra contain two or more lanes [e.g., 212]. The lower and upper frequency bands are emissions at the fundamental (f_p) and second harmonic ($2\ f_p$) of the local plasma frequency, which is given by Equation 2.3. Sometimes the type II lane is observed with band splits in both fundamental and harmonic. Band splitting is caused by plasma emission from upstream and downstream shock regions [213, 214, 203]. This assumption has recently been confirmed by Zimovets et al. [215] and Zucca et al. [216].

2.4.4.1 Estimating CMEs Speed from Associated solar Radio Type II Bursts

Assuming that the burst was emitted at plasma (fundamental, f_p, and second harmonic, $2\ f_p$) frequency, the electron density in the corona decreases as a function of radial distance r, the drift rate ($\frac{df}{dt}$) of type II burst can be deduced and used to estimate the speed of CMEs (i.e. speed of shock waves). Previous studies have described methods for estimating the speed of CMEs from associated radio type II bursts observations [e.g., 217, 218, 219]. The first derivative of Equation 2.3 gives

$$\begin{aligned}
\frac{df_p}{dr} &= 8.98 \times 10^3 \times \frac{d\sqrt{n}}{dr} \\
&= 8.98 \times 10^3 \times \frac{dn^{1/2}}{dr} \\
&= 8.98 \times 10^3 \times \frac{1}{2} \times N^{-1/2} \times \frac{dn}{dr} \\
&= 8.98 \times 10^3 \times \frac{1}{2\sqrt{n}} \times \frac{dn}{dr} \\
&= 8.98 \times 10^3 \times \frac{\sqrt{n}}{2n} \times \frac{dn}{dr} \\
\frac{df_p}{dr} &= \frac{f_p}{2n}\frac{dn}{dr} \qquad (2.4)
\end{aligned}$$

Because the plasma frequency f_p of a particular SRB is a function of radial distance r and time t, the chain rule can be used to calculate the speed as shown below.

$$\frac{df_p}{dt} = \frac{df_p}{dr}\frac{dr}{dt} \qquad (2.5)$$

The expression $\frac{dr}{dt}$ in Equation 2.5 is the speed of the CMEs, V. Substituting Equation 2.4 into Equation 2.5 and assuming that the shock moves parallel to the coronal density of particles, we get

$$\frac{1}{f_p}\frac{df_p}{dt} = \frac{V}{2}\frac{1}{n}\frac{dn}{dr} \qquad (2.6)$$

In Equation 2.6, the expression $\frac{1}{n}\frac{dn}{dr}$ represents the scale height L_n^{-1}. If the corona density model is provided, the expression for this quantity can be obtained. Assume a density model of the form

$n = n_0 r^{-\alpha}$, where r is in $R_\odot$ [104], then

$$\begin{aligned}\frac{dn}{dr} &= n_0(-\alpha)r^{-\alpha-1}\\ &= n_0(-\alpha)r^{-\alpha} \times \frac{1}{r}\\ &= n_0 r^{-\alpha}(-\alpha)\frac{1}{r}\\ \frac{dn}{dr} &= -\alpha\frac{n}{r} \end{aligned} \tag{2.7}$$

The scale height can be obtained by rearranging Equation 2.7 and gives

$$\frac{1}{n}\frac{dn}{dr} = L_n^{-1} = -\frac{\alpha}{r} \tag{2.8}$$

Substituting Equation 2.8 into Equation 2.6 we get

$$\frac{1}{f_p}\frac{df_p}{dt} = -\frac{V}{2}\frac{\alpha}{r} \tag{2.9}$$

Rearranging Equation 2.9, the speed of exciting agency (CMEs) V, is finally given by

$$V = -\frac{2r}{\alpha}\frac{1}{f_p}\frac{df_p}{dt} \tag{2.10}$$

where r is the shock formation height, α is a fitted empirical index of density variation over the heliocentric distance, f is the starting frequency, and $\frac{df_p}{dt}$ is the frequency drift rate. The negative sign in Equation 2.10 cancels out the negative sign of drift rate, and the speed of CMEs becomes positive. The electron density decreases with heliocentric distance from the Sun, according to the power-law: $\mathrm{n_e(r)} \propto \mathrm{r}^{-\alpha}$. Three different density models given by Newkirk [118], Saito et al. [220] and Leblanc et al. [221] described the variation of the electron density in the corona and IP medium. With these models, it has been observed that within $1-3\ \mathrm{R}_\odot$, the electron density is directly proportional to r^{-6} in the corona and directly proportional to r^{-2} beyond few tens of $R_\odot$. For metric type II bursts, $\alpha \sim 6$ when $r < 2R_\odot$ [104]; for decametric and hectometric type II bursts, $\alpha \sim 4$ when $2R_\odot < r < 3R_\odot$; and for interplanetary type II bursts (i.e., $r > 5R_\odot$), $\alpha \sim 2$ [222]. Note that α decreases with increasing distance from the Sun.

The number of energetic electrons moving upward or downward in the solar corona is governed by Newkirk's model, $n(r) = 4.2 \times 10^{4+\frac{4.32}{r}}$ [223]. This model describes the density behavior in the corona above quiet equatorial regions, where sources of metric type II bursts are expected [224]. By rearranging Equation 2.6, the speed of CME is given by the following equation

$$V = 2\left(\frac{1}{n}\frac{dn}{dr}\right)^{-1}\frac{1}{f_p}\frac{df_p}{dt} \tag{2.11}$$

The expression $\frac{dn}{dr}$ in Equation 2.11 can be obtained as follows,

$$\begin{aligned}
\frac{dn}{dr} &= \frac{d\left(4.2 \times 10^{4+\frac{4.32}{r}}\right)}{dr} \\
&= \frac{d\left(4.2 \times 10^{4} \times 10^{\frac{4.32}{r}}\right)}{dr} \\
&= 4.2 \times 10^{4} \frac{d\left(10^{\frac{4.32}{r}}\right)}{dr} \\
&= 4.2 \times 10^{4} \times \left(\frac{-4.32 \ln 10}{r^2}\right) \times 10^{\frac{4.32}{r}} \\
&= -4.32 \ln 10 \times 4.2 \times 10^{4+\frac{4.32}{r}} \times \frac{1}{r^2} \\
\frac{dn}{dr} &= -4.32 \ln 10 \times n \times \frac{1}{r^2} \qquad (2.12)
\end{aligned}$$

Using Equation 2.12, the term $\left(\frac{1}{n}\frac{dn}{dr}\right)^{-1}$ in Equation 2.11 gives

$$\left(\frac{1}{n}\frac{dn}{dr}\right)^{-1} = \left(\frac{-4.32 \ln 10}{r^2}\right)^{-1} = -\frac{r^2}{4.32 \ln 10} = -0.1 r^2 (R_\odot) \qquad (2.13)$$

For metric type II bursts at $r \sim 1.5\ R_\odot$, the scale height $\left(\left(\frac{1}{n}\frac{dn}{dr}\right)^{-1}\right)$ is equal to $1.575 \times 10^5\ km$. Up on substituting Equation 2.13 in Equation 2.11, the CME speed can be calculated from

$$V = -0.2 r^2 \frac{1}{f_p}\frac{df_p}{dt} \qquad (2.14)$$

2.4.4.2 Computation of Coronal Magnetic Field from observation of Solar Radio Type II Bursts

Metric type II (M-type II) bursts typically exhibit the fundamental emission band (hereafter F-band) and the harmonic emission band (hereafter H-band), which are frequently split into two parallel lanes [193]. There have been several interpretations proposed for band-splitting that account for magnetic, Doppler, and geometrical effects [169]. Smerd et al. [213] proposed an explanation based on emission from the upstream and downstream shock regions, revealing a potentially useful tool for estimating the coronal Alfvén speed and magnetic field. Mann et al. [225] and Mann et al. [226] investigated the relative instantaneous bandwidth of m- type II bursts. The relative bandwidths ranged from 0.1 to 0.7, with the distribution maximum around 0.3, and the values were found to be positively correlated with the radio source velocity. Using the upstream/downstream interpretation, it was determined that the shocks that cause m- type II bursts are either weak supercritical quasi-parallel or subcritical quasi-perpendicular fast-mode MHD shocks. The instantaneous bandwidth (BDW) of a particular m-type II radio burst and due to the plasma frequency's relationship with electron density ($f \propto \sqrt{N}$), one finds that:

$$BDW = \frac{f_u - f_l}{f_l} = \frac{f_u}{f_l} - 1 = \sqrt{\frac{N_u}{N_l}} - 1 \tag{2.15}$$

where $\mathrm{f_u}$ and $\mathrm{f_l}$ denote the upper and lower frequencies, respectively of the fundamental emission band. N_U and N_l are the electron densities in the upstream and downstream region, respectively. Figure 2.13 shows an example of m-type II radio burst of 19 August 2022 for which $\mathrm{f_u}$ and $\mathrm{f_l}$ are acquired from the fundamental frequency band. The value of BDW can directly be linked to the density jump across the shock if the interpretation in terms of upstream/downstream emission is accepted. Using Equation 2.15 the density jump (χ) can be expressed as:

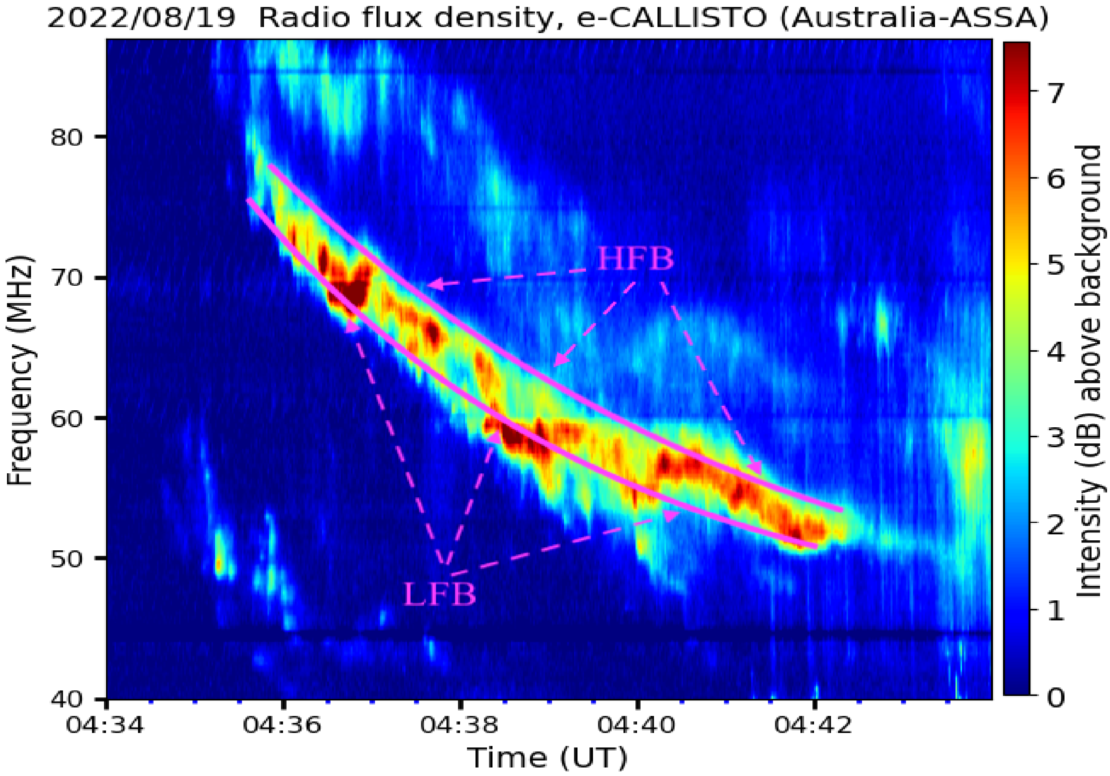

Figure 2.13: The determination of f_u and f_l at the fundamental frequency band's upper and lower frequency branches (HFB and LFB, respectively) during the m-type II burst on 19 August 2022. Lines that follow emission ridges and define the f_u and f_l represent the HFB and LFB of the fundamental band, respectively.

$$\chi = \frac{N_u}{N_l} = (BDW + 1)^2 \tag{2.16}$$

providing an estimate of the compression behind the shock front [e.g., 227, 228, 229, 52, 230]. By assuming low plasma ratio ($\beta \to 0$) for a perpendicular shock in the corona [227, 228, 229], the density jump allows one to compute the Alfvén Mach number (M_A) using Rankine-Hugoniot approximation

$$M_A = \sqrt{\frac{\chi(\chi+5)}{2(4-\chi)}} \tag{2.17}$$

The Alfvén velocity is directly related to the shock speed (Equation 2.10) as

$$V_A = \frac{V}{M_A} \tag{2.18}$$

In the region surrounding a CME, the ambient magnetic field strength (B) of the plasma can be estimated using the relation [e.g., 228, 52, 231]

$$B[G] = 5.1 \times 10^{-5} \times f_l[MHz] \times V_A[km/s] \tag{2.19}$$

2.4.5 Type III bursts

Among solar radio emissions, radio type III bursts are the most dominant. They are fast drift bursts ($\sim 100\ MHz/s$, in metric wavelength) from high to low frequencies in the dynamic spectrum, lasting only a few seconds on average [e.g., 232, 233]. Type III bursts begin at GHz frequencies in powerful SFs [234]. According to Reid and Ratcliffe [232], type III radio bursts are thought to be produced by energetic electron beams that are accelerated during flares and travel through IP space along open magnetic field lines. At the local plasma frequency, the electron beams drive Langmuir waves, some of which undergo electromagnetic radiation conversion at the fundamental frequency and/or its second harmonic. Type III bursts are divided into three categories: isolated bursts lasting 1-3 seconds, groups lasting 10 minutes, and storms lasting several hours. Figure 2.14 illustrates an example of isolated type III burst and a group of type III burst occurred in succession on 24 August 2015 by CALLISTO based in Rwanda.

2.4.6 Type IV bursts

Solar radio type IV bursts are broadband continuum emissions from the solar atmosphere at decimetric-decametric wavelengths, as first classified by Boischot [178], while the flare continuum is their higher frequency counterpart. The dynamic spectra of some events show that the two continuum bursts are indistinguishable. It has been proposed that the two bursts are produced by the same radiation mechanism [e.g., 235, 236]. Type IV radio bursts are classified into two types: moving type IV bursts (IVm) and stationary type IV bursts (IVs) [237]. Stationary type IV bursts are produced by magnetic structures that are typically located above active regions; they frequently exhibit significant fine structure [238, 239]. The source model of solar type IV bursts consists of two interacting loops separated by one spatial order of magnitude. Moving type IV bursts [235] are emitted from meter wave continuum sources that are thought to move outwards at velocities of the order of 100 –1000 km/s; their spectrum is often featureless and can last for more than 10 minutes. Some of them appear after type II bursts and may be caused by energetic electrons produced in the wake of the type II shock. Others could be caused by energetic electron populations trapped in expanding magnetic arches or plasmoids, which are blobs of dense plasma with their own magnetic field [240, 241]. Figure 2.15 depicts an example of a stationary type IV

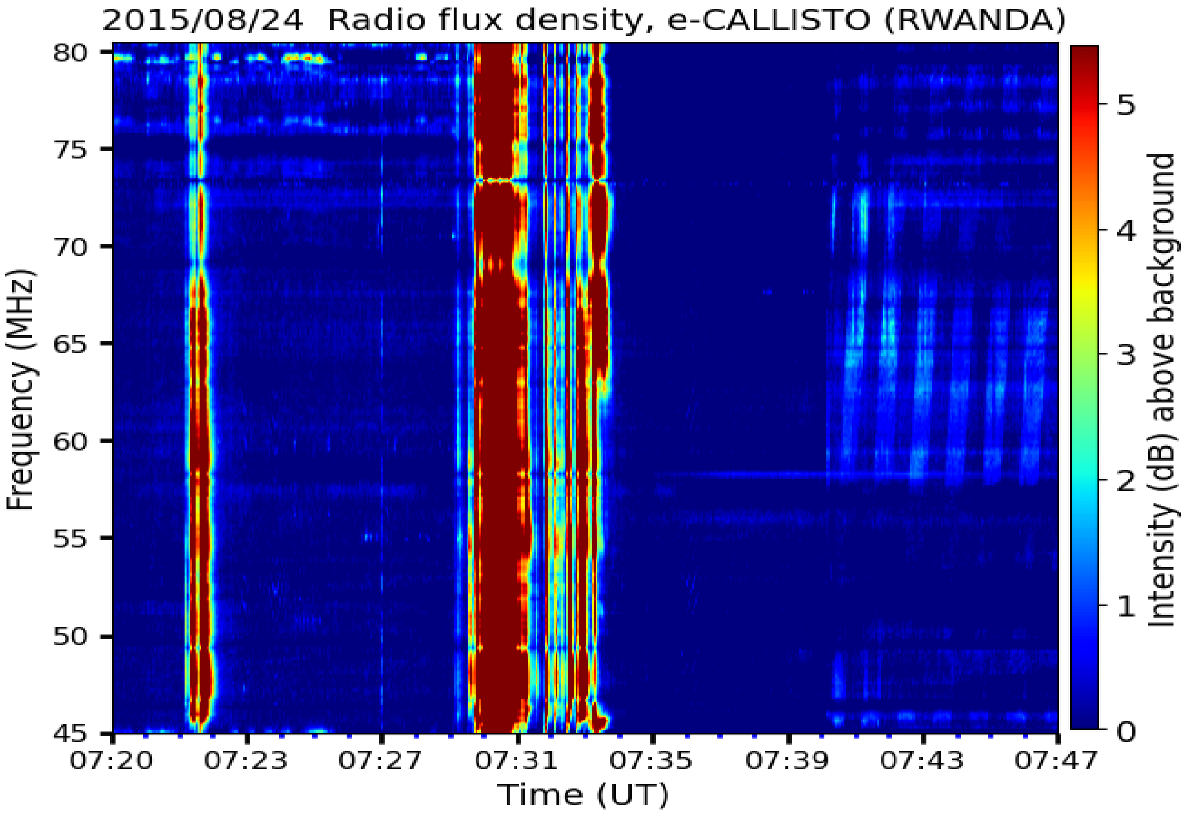

Figure 2.14: Dynamic spectrum of 24 August 2015 type III radio bursts. An isolated type III burst at 07:22 UT followed by a group of type III bursts observed at 07:30 UT by CALLISTO Rwanda. The one at 07:22 UT occurred during the decaying phase of a C6.7 flare (started, peaked, and ended at 07:08, 07:12 and 07:15 UT, respectively). A group of type III bursts at 07:30 UT is triggered by a M5.6 flare in its rise phase (started at 07:26 UT, peaked at 07:33 UT and ended at 07:35 UT, respectively).

bursts observed by the CALLISTO at Badary observatory (SSRT), Siberia, Russian Federation on 7 March 2012. Many mechanisms for radio emission have been proposed, the most common of which are synchrotron and gyrosynchrotron emissions [e.g., 242, 243], plasma emission [e.g., 244, 245], and electron cyclotron maser emission [e.g., 246, 247].

2.4.7 Type V bursts

Type V bursts are low-frequency, wide-bandwidth continuum emissions that last one to three minutes. They immediately follow type III bursts or groupings of type III bursts [179]. The average duration of type V bursts ranges from 40 s at 200 MHz to 200 s at 20 MHz. Type V bursts are located at the same height as earlier type III bursts. Type V sources, on the other hand, are usually a few tenths of a solar radius or more away from type III sources. In addition, the source size of type V radiation is generally larger than that of type III radiation, and it grows significantly as frequency decreases [248].

2.5 The Earth's Ionosphere

The ionosphere is the part of the Earth's atmosphere where ionizing radiation (primarily from solar ultraviolet and x-ray emissions) causes electrons to exist in sufficient quantities to interfere with

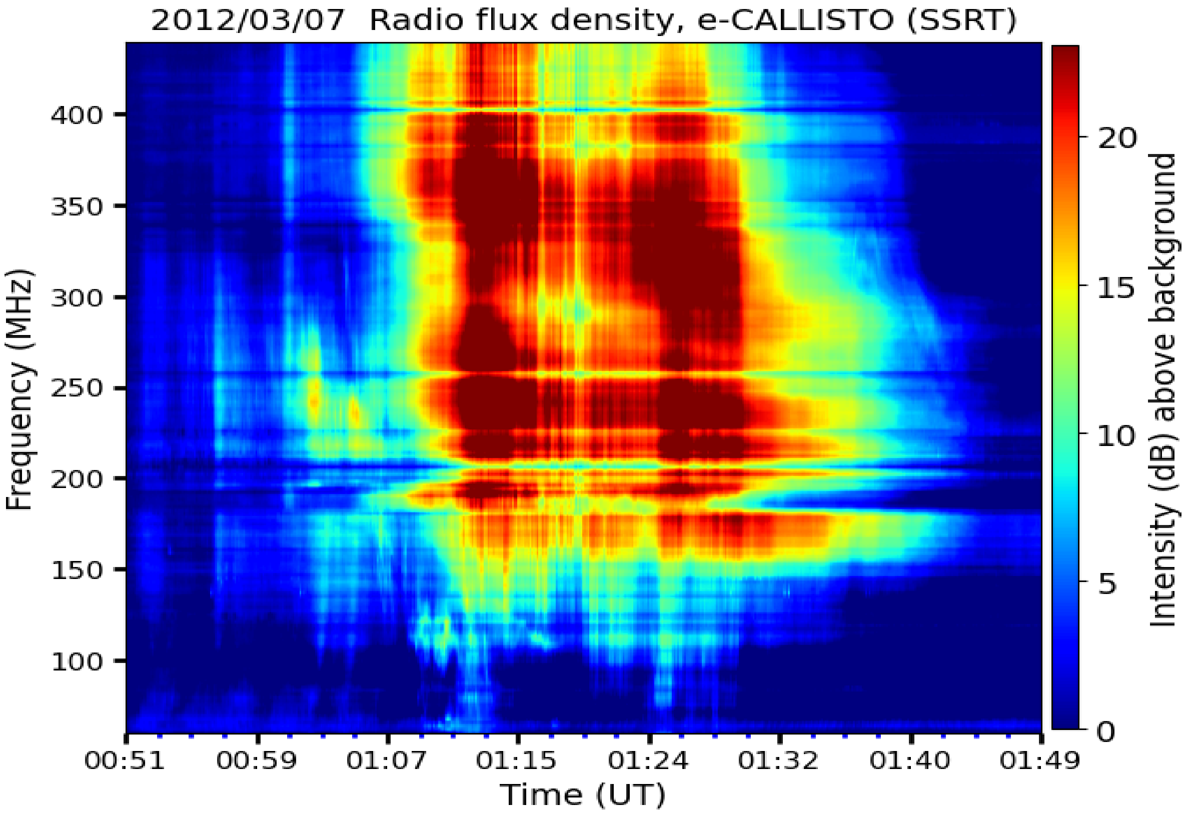

Figure 2.15: A broad type IV solar burst with a very high intensity detected at Badary observatory (SSRT site), Siberia, Russian Federation on 7 March 2012 from 1:00 UT to 1:50 UT.

radio wave propagation [249]. It has no fixed boundaries but is usually thought to exist between 50 and 1000 km altitude [250] and is controlled by the Sun. The ionosphere is influenced by a variety of chemical and dynamical processes that occur in the thermosphere, magnetosphere, and lower atmosphere [251]. It is divided into layers that are denoted as D, E, F1, and F2 based on their heights and chemical compositions within the atmosphere. Figure 2.16 depicts the ionospheric layers and the main variability caused by solar activity. However, ionization in the ionospheric layers is primarily determined by the Sun and its activity. The F2 layer is most important for radio propagation through the ionosphere because it has the highest electron density [252]. The state and behavior of the ionosphere are described using the ionospheric total electron content (TEC) as a key parameter that is discussed in the next section.

2.6 Total Electron Content (TEC)

Total electron content (TEC) is the density of electrons integrated along the signal path from transmitter to the receiver (Equation 2.20); it is measured in TEC units (TECU), with 1 TECU equivalent to 10^{16} free electrons per m^2 [101].

$$\int_R^S N_e \, ds \tag{2.20}$$

The TEC of the ionosphere is widely used in studies of the near-Earth plasma environment. Several studies have shown that GPS observations of TEC can help researchers understand the

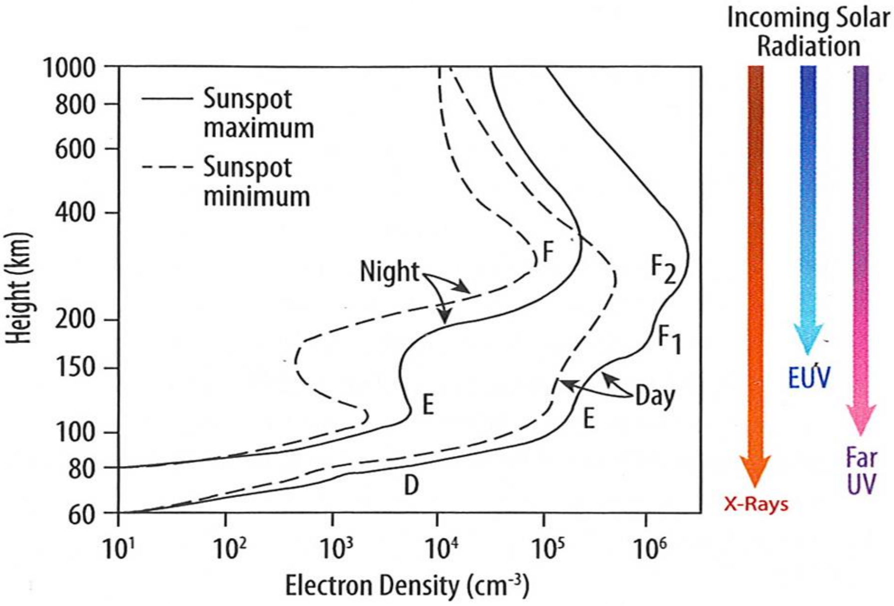

Figure 2.16: Major ionospheric layers. Courtesy from Bosinger et al. [253]

characteristics of ionospheric variations during geomagnetic storms [e.g., 254]. TEC has diurnal, seasonal, solar cycle, and geographical variations [255]. Solar activity can result in typical magnetospheric and ionospheric conditions. X – ray flares and radio bursts can disrupt GPS navigation by appearing as broadband noise [256, 257]. Rapid changes in solar activity, such as SFs, can cause a series of disturbances in the terrestrial upper atmosphere, resulting in abrupt variations in the ionospheric TEC [258]. The largest gradients and ionospheric disturbances in the TEC are typically present during positive ionospheric storms [259]. SRBs are abrupt increases in radio energy from the Sun that interfere with the receiver's ability to track the GPS satellite signal, which is dependent on TEC [260]. SRBs, on the other hand, are generally wide-band interfering radio sources from the Sun that cause increases in the receiver's spectral noise density, No. During the SRB, the satellite's carrier power, C, remains constant [261].

2.7 Summary

This chapter briefly described the Sun as the engine driving space weather. It also detailed radio emissions and their characteristics, and concluded with an overview of space weather effects and their monitoring.

Chapter 3

Research Data and Methodology

This chapter describes the data sources, the instruments used for observations, and the methodology employed to analyze the data in this study.

3.1 Observational data of Solar Radio Bursts

Radio observations of solar bursts were made using both ground-based radio telescopes and space-based radio missions.

3.1.1 Ground Observations

In this study, solar radio type II, type III, and type IV bursts in the form of dynamic spectra (plots of intensity as a function of frequency and time) were used. During SC 25, the dynamic spectra from the e-CALLISTO spectrometers (https://e-callisto.org/) were the main focus. CALLISTO was conceived and developed by the Radio and Plasma Physics Group (PI: Christian Monstein) at ETH Zurich, Switzerland, as a new concept for solar radio spectrographs [44]. All CALLISTO spectrometers around the world form the extended CALLISTO (e-CALLISTO) network, a global network of frequency-agile SRB spectrometers. The primary goal of e-CALLISTO is to provide 24-hour monitoring of metric and decametric SRBs [45]. The total frequency range of CALLISTO spans from 20 MHz to 870 MHz [44]. The e-CALLISTO system has proven to be a useful tool for tracking solar activity by determining types of solar radio emission from solar eruptions [262]. One of the special features of the e-CALLISTO network is that, through the cooperation of many nations, the Sun can be monitored 24 hours on daily basis, and all the data are collected remotely and stored in an online database [263]. Figure 3.1 illustrates the global distribution of CALLISTO spectrometers that form e-CALLISTO network used in this study. The e-CALLISTO

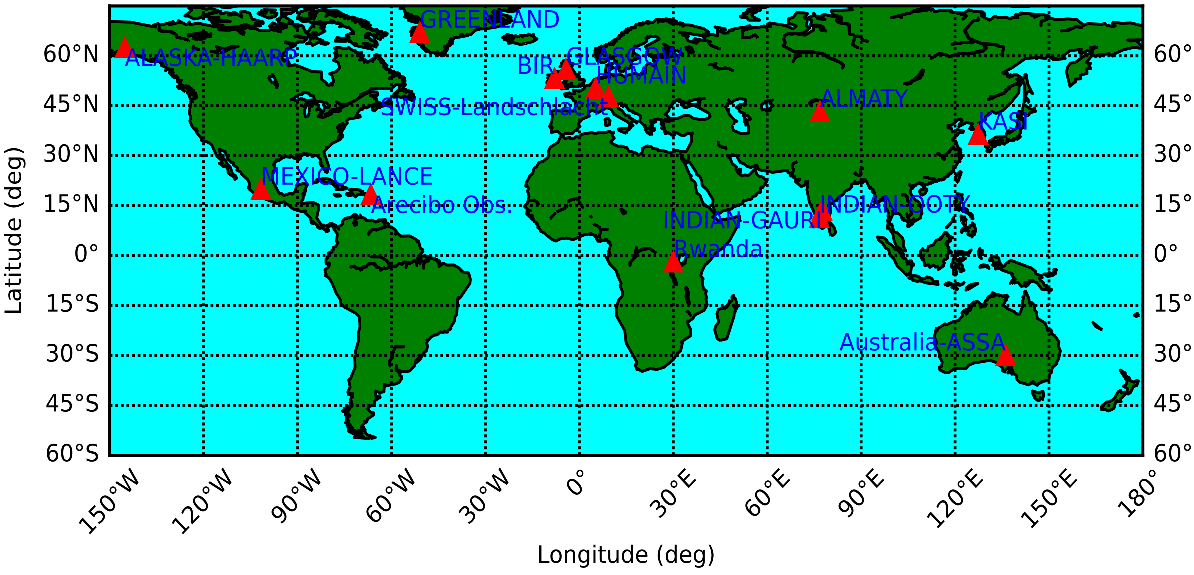

Figure 3.1: Worldwide distribution of a portion of the radio spectrographs in the e-CALLISTO network used for this study. The network also includes spectrograph in Rwanda.

network provides dynamic spectra in FITS format. By navigating the quick-look section on the e-CALLISTO website, the desired FITS files were downloaded and subsequently processed using Python scripts to create 2 – D dynamic spectra and to record key radio parameters, namely the time range, the start and end frequencies.

To address the first objective, the study began by downloading 32 radio type II bursts with clear morphology, each detected by one spectrometer among others, between May 2021 and December 2022. SRBs exhibit several characteristics such as frequency drift rates, frequency range, and duration, etc., that can be used to investigate various aspects of the middle and/or upper corona. The frequency drift rate was estimated from dynamic spectra using the following equation

$$\frac{df}{dt}[MHz/s] = \left|\frac{\Delta f[MHz]}{\Delta t[s]}\right| = \left|\frac{f_s - f_i}{t_s - t_i}\right| \tag{3.1}$$

where f_i stands for the starting frequency, f_s for the stopping frequency, t_i is the initial time, and t_s is the stopping time. Equation 2.10 relates the drift rate of m - type II radio burst to both the density gradient in the solar corona and the shock speed of the source that causes it [56]. Shock parameters associated with these type II radio events were computed using Equations 2.10 to 2.19 and their shock formation heights were estimated using the empirical relation found in [56] given as

$$f(r) = 307.87r^{-3.78} - 0.14 \tag{3.2}$$

For the second and third objectives, the study began with samples of geomagnetic storms and SEPs, respectively. The next step involved analyzing the radio parameters such as start and end frequencies, durations, frequency ranges, and, where applicable, estimated drift rates. The third objective required a comparative analysis of three consecutive solar cycles, for which dynamic spectra from the Community of European Solar Radio Astronomers (CESRA, https://www.astro.gla.ac.uk/users/eduard/cesra/?page_id=181) were accessed.

3.1.2 Space–based radio observation

To complement the ground-based observations with space-based counterparts, dynamic spectra in Common Data Format (CDF) from the Radio and Plasma Wave Investigation (WAVES) instrument onboard the Wind spacecraft [WAVES/Wind, 159] and Solar Terrestrial Relations Observatory [STEREO, 264] missions were used. WAVES/Wind includes several sensitive radio receivers that cover a frequency range from 4 kHz to 14 MHz, providing information on both decametric – hectometric (DH) and kilometric (km) type II bursts. The 2 to 20 MHz gap between ground-based and space-borne observations has long been a major impediment to understanding the relationship between coronal and interplanetary (IP) shocks. The WAVES instrument has effectively bridged this gap. It uses three receivers to detect radio emissions across different spectral ranges: Radio Receiver Band 2 (RAD2: 13.825–1.075 MHz), Radio Receiver Band 1 (RAD1: 1040–20 kHz), and the Thermal Noise Receiver (TNR: 245–4 kHz). The spectral range of the RAD1 receiver begins in the hectometric range (288.5 m) and extends into the kilometric domain (15 km), while the RAD2 spectral range corresponds to wavelengths from 21.7 to 279 m (DH wavelength range). The data were accessed from: https://spdf.gsfc.nasa.gov/pub/data/wind/. The STEREO/WAVES (SWAVES) experiment on the STEREO spacecraft measures the radio spectrum at frequencies ranging from a few kHz to 16 MHz, enabling the tracking of radio disturbances from the Sun to Earth [265]. The STEREO/WAVES system consists of a fixed High Frequency Receiver (HFR), a Low Frequency Receiver (LFR), and a Time Domain Sampler (TDS). Data were obtained from: https://solar-radio.gsfc.nasa.gov/data/. The CDF files were processed using python scripts to generate 2-D dynamic spectra and in some cases were plotted together with FITS files from the e-CALLISTO.

3.2 Solar Flare Observation

The Geostationary Operational Environmental Satellites (GOES) observes the Sun and Earth from geosynchronous orbit, with an orbital period equal to the Earth's rotation period. The primary instrument onboard GOES is the X-ray telescope with the X-ray Sensor (XRS) unit, which provides solar X-ray fluxes in the wavelength bands of 1 – 8 Å and 0.5 – 4 Å. The X-ray spectrometers on the GOES spacecraft (1 - 8 Å band) are used to classify SFs. SFs are classified using the letters A, B, C, M, and X when its peak flux falls between 10^{-8} and 10^{-4} Wm^{-2} at a distance of 1 AU from the Sun. For this study, the required SF parameters included start and peak times, flare class, source active region number, and solar source location. These parameters were obtained from GOES at: https://www.ngdc.noaa.gov/stp/space-weather/solar-data/solar-features/solar-flares/x-rays/goes/xrs/, for the third objective, and from the more recent archive at: https://www.lmsal.com/solarsoft/latest_events_archive.html. Both sources are also accessible via the SolarMonitor website: https://solarmonitor.org/. In this study, if a radio burst was present between the onset and end times of a flare, it was considered flare-associated; otherwise, it was treated as non-flare-associated.

3.3 White-light Observations

The first evidence of the solar corona's existence was provided by solar eclipses. During these events, the Moon's disk blocks the bright solar surface, revealing the visible outer atmosphere, which appears as streamers and plumes extending far from the Sun. Until the early 20th century, solar eclipses were the only feasible method for observing the corona. The first coronagraph telescope was developed by French astronomer Bernard Lyot in 1939, enabling continuous observation of the corona [266]. All modern coronagraphs i.e., space-based instruments that observe the corona over a wide height range, are fundamentally based on Lyot's original design.

3.3.1 SOHO LASCO

The Large Angle and Spectrometric Coronagraph [LASCO, 102], is a set of three coronagraphs (C1, C2 and C3) onboard the Solar and Heliospheric Observatory [SOHO, 103] located at Lagrangian point 1. The LASCO field of view (FOV) is able to detect CMEs in white-light corona and track their propagation over a long distance. It takes the images of the solar corona from 1.1 to 30 $R_\odot$: LASCO/C1 has a FOV range of 1.1 – 3.0 $R_\odot$, LASCO/C2 has a FOV range of 1.5 – 6.0 $R_\odot$, and LASCO/C3 has a FOV range of 3.7 - 30 $R_\odot$ beyond the C2 FOV. The CME parameters (onset times and linear speeds) were obtained from LASCO/SOHO catalog, generated and maintained at the CDAW Data Center by NASA and the Catholic University of America at: https://cdaw.gsfc.nasa.gov/CME_list/.

3.3.2 STEREO/SECCHI

The STEREO consists of two nearly identical spacecraft, STEREO-Ahead and STEREO-Behind, which travel ahead of and behind Earth in its orbit. Each spacecraft moves away from Earth at a rate of 22° per year, effectively orbiting the Sun in opposite directions. Both spacecraft carry an identical set of instruments known as the Sun-Earth Connection Coronal and Heliospheric Investigation (SECCHI), which includes two coronagraph imagers: COR1 and COR2 [139]. The combination of COR1-A and COR2-A with COR1-B and COR2-B provides a stereoscopic view of the solar corona and transient events occurring within a heliocentric distance of 1.4 to 15 $R_\odot$. COR1 was designed to detect the weak light of the solar corona despite the presence of scattered light from the much brighter solar photosphere. COR1 coronagraphs routinely provide images of the corona at heights ranging from 1.5 $R_\odot$ to 4 $R_\odot$, where the transition from closed to open coronal structures occurs [139]. A linear polarizer is used in the coronagraph to block scattered light and capture the polarized brightness signal from the solar corona.

Among various types of data provided by the STEREO/SECCHI spacecraft, COR2 coronagraph images are the most commonly used for CME analysis. COR2 is an externally occulted Lyot coronagraph, based on the highly successful LASCO C2 and C3 designs. Like COR1, COR2 is designed to observe weak coronal signals in visible light and has FOV ranging from 2.5 to 15 $R_\odot$ [139]. For recent data that are not available in the CDAW data, the onset times and linear speeds of CMEs from STEREO/SECCHI were accessed via the Solar Eruptive Event Detection System (SEEDs, http://spaceweather.gmu.edu/seeds/). A CME is considered associated with a SF if its onset occurs within one hour of the flare's onset. Similarly, the association between SRBs and CMEs is confirmed based on time coincidence, with a time window of approximately one hour from the onset of the radio burst. Running difference images from SOHO/LASCO and STEREO/SECCHI were generated using the Helioviewer software (http://www.helioviewer.org) , which retrieves original images directly from the source and operates online (https://gs671-suske.ndc.nasa.gov/).

3.3.3 The Atmospheric Imaging Assembly

With a spatial resolution of $0.6''$ and a temporal resolution of 12 seconds, the Atmospheric Imaging Assembly (AIA) on board the Solar Dynamics Observatory [SDO; 267] consists of four Cassegrain telescopes capable of capturing full-disk visible, ultraviolet (UV), and extreme ultraviolet (EUV) images of the transition region and corona up to $0.5\ R_\odot$ above the photosphere. The telescopes provide imaging in seven extreme ultraviolet passbands centered on the spectral lines of Fe XVIII (94 Å), Fe VIII/XXI (131 Å), Fe IX (171 Å), Fe XII/XXIV (193 Å), Fe XIV (211 Å), He II (304 Å), and Fe XVI (335 Å). One of the telescopes observes longer wavelengths at C IV (1600 Å), the nearby continuum at 1700 Å, and a broadband visible filter centered on 4500 Å, offering full temperature coverage from 5×10^3 K to 2×10^7 K. SDO/AIA images allow us to observe jets and their source regions with both high temporal and spatial resolution [268]. In this study, spectrograms from the Helioseismic and Magnetic Imager [HMI, 269, 270] onboard SDO were overlaid with AIA/SDO images at specific wavelengths to characterize the solar source locations of eruptive events, processed using the SunPy software (https://sunpy.org/).

3.4 GNSS TEC Data

The first objective was extended to include the analysis of space weather disturbances on bursty days in terms of ionospheric TEC. To address the need for ionospheric TEC, database archives, including GPS data from ground-based GPS receiver stations worldwide, were used. These archives include the UNAVCO Archive of GNSS Data (https://www.unavco.org/) and the African Geodetic Reference Frame (AFREF) database (http://afrefdata.org/). Figure 3.2 maps the geographic locations of some GNSS stations used in the current study for a reference. The GNSS stations were randomly selected based on the currently available data from the equatorial, mid-, and high-latitude regions. As GPS data are usually provided in Receiver Independent EXchange (RINEX) format, TEC were derived from Rinex files using the GPS TEC software version 3 developed at Boston college, assuming a thin shell ionosphere at the altitude of 350 km. Details on the software used to derive TEC are provided in Seemala and Valladares [271], Uwamahoro et al. [272], and references therein. The software calculates the vertical TEC from observational data using a suitable mapping function, given by:

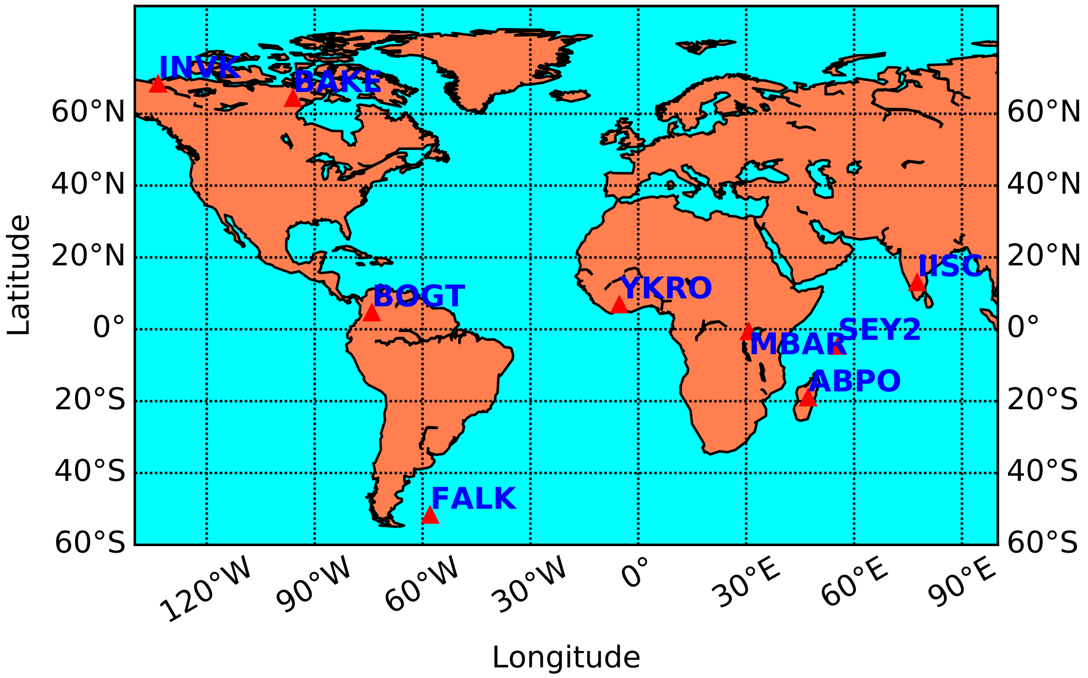

Figure 3.2: Geographic locations of some GNSS stations used for this study (FALK: Falkland, Islands; ABPO: Madagascar; MBAR: Uganda; SEY2: Seychelles; IISC: India; YKRO: Ivory coast; BOGT: Colombia; BAKE: Canada and INVK: Canada).

$$S(E) = \frac{1}{\cos(z)} = \left[1 - \left(\frac{R_E \times \cos(E)}{R_E + h_s}\right)^2\right]^{-0.5} \tag{3.3}$$

where $S(E)$ =mapping function, Z = zenith angle of the satellite, R_E = Earth's radius, E = elevation angle in radians, and h_s = altitude of the thin layer above the surface of the Earth (taken as 350 km). To reduce the multipath effects on slant TEC (STEC), the elevation angle was fixed to $30°$. The rate of change in TEC (ROT) was calculated using the equation 3.4 proposed by Pi et al. [34], and has been utilized by several researchers to explore ionospheric irregularities [273, 274, 35, 275, 276].

$$ROT = \frac{STEC_{k+1} - STEC_k}{\Delta t_k} \tag{3.4}$$

where $STEC_{k+1}$ and $STEC_k$ are the STEC values at two successive epochs, and Δt_k is the time difference between them equivalent to 30 s for IGS given in Figure 3.2. Equation 3.4 was used to calculate the ROTI, which was defined as the standard deviation of ROT over 5 minutes.

$$ROTI = \sqrt{< ROT^2 > - < ROT >^2} \tag{3.5}$$

where the $<>$ stands for the time average value. The code for ROTI computation are accessible at https://www.mathworks.com/matlabcentral/fileexchange/129239-programs-to-compute-rot-and-roti [277].

3.5 Geomagnetic and IP Indices

The Sun emits different types of outputs such as electromagnetic radiation, solar wind, and IP IMF which interact with the near-Earth space environment. These interactions change the flow of electric currents in space, leading to variations in the Earth's magnetic field that can be measured from space down to the ground. Geomagnetic activity is monitored using various indices that represent different current systems. For example, the Dst index measures storm-time activity, the Kp index is a 3-hour measure that reflects the global intensity of irregular disturbances in the geomagnetic field caused by solar particle radiation during the corresponding time interval [278]. For a complete description of geomagnetic indices, the reader can refer to [279] and [280] for general reviews, as well as to [281] for K-derived indices and [282] for Dst derivation. Geomagnetic indices such as Dst index and the Symmetric H-component (SYM-H) index primarily reflect the strength of the ring current during geomagnetic storms [279, 283, 284]. These indices are derived from a network of ground-based magnetometers located at low latitudes across different longitudes. The SYMH index is essentially the same as Dst but offers a higher temporal resolution of one minute, making it particularly useful for examining short-term variations during geomagnetic disturbances. All these indices can be taken from Geomagnetic Data Service Kyoto (https://wdc.kugi.kyoto-u.ac.jp/wdc/Sec3.html) and high resolution SYM-H index can be taken from OMNIWeb: https://omniweb.gsfc.nasa.gov/form/omni_min.html.

The second objective of the study began by selecting all geomagnetic storms with a Dst index less than - 50 nT that occurred between January 2020 and June 2023. A total of 35 geomagnetic storms were identified using data from the website: https://www.spaceweatherlive.com/. The exact moment when the z-component of the IMF (Bz) responded to the fast-forward shock caused by a

CME impacting the magnetosphere was determined using SYM-H index data. To establish the link between solar radio emissions and geomagnetic storms, a backward search was conducted within five days following the arrival of CMEs near the magnetosphere, using radio observations recorded by the e-CALLISTO network at the following stations and their IP counterparts were checked using the WAVES/WIND and STEREO/WAVES:

- CALLISTO $\mathrm{Australia\_ASSA}$ (location: Astronomical society of south Australia, South Australia, coordinates: $30.00°S$, $136.21°E$, frequency band: 15 – 86 MHz, aerial: LWA).
- CALLISTO $\mathrm{Arecibo\_Observatory}$ (location: Arecibo, Puerto Rico, USA, coordinates: $18.12°N$, $66.59°W$, frequency band: 15 – 86 MHz, aerial: LWA).
- CALLISTO ALMATY (location: Tsao Almaty, Kazakhstan, coordinates: $43.22°N$, $76.83°E$, frequency band: 45 – 165 MHz, aerial: log-periodic dipole array antenna).
- CALLISTO Bir (location: Birr, Ireland, coordinates: $16.61°N$, $77.51°E$, frequency band: 10 – 100 Mhz, aerial: bicone antenna).
- CALLISTO GLASGOW (location: Glasgow, Scotland, coordinates: $55.86°N$, $4.26°W$, frequency band: 45 – 80.5 MHz, aerial: log-periodic dipole array antenna).

The time interval between burst registration (t_b) and CME impact (t_c) was calculated ($t = t_c - t_b$) and verified if $V_{CME} \times t = 1\ AU$ to confirm the association. Table 3.1 presents the geomagnetic storms occurred during the ascending phase of SC 25 and their backed associated radio bursts with the help of the above instruments. Their associated Soft X-ray flares were obtained using the solar monitoring website and the onset and linear speeds of CMEs were taken from LASCO-C2/SOHO and SECCHI/STEREO catalogs.

In the context of solar – terrestrial interactions, the focus lies on identifying the sources and sinks of energy. The solar wind interacts with Earth's magnetosphere, transferring energy that is eventually dissipated across the magnetosphere, ionosphere, and thermosphere system [e.g., 285, 286, 287, 288]. During intense solar events, this energy transfer can significantly impact satellites, communication systems, power networks, and other critical technologies [e.g., 289, 290, 291, 292]. Accurately measuring the amount of energy transmitted from the solar wind to the magnetosphere remains a major challenge in space weather forecasting. Over the years, researchers have introduced various coupling functions both empirical and theoretical to describe this energy exchange [e.g., 293, 294, 295, 296, 297, 298, 299]. One notable example is the energy coupling function proposed by Perreault and Akasofu [300], which estimates the power input from the solar wind into the magnetosphere. The function (also known as Akasofu's ϵ parameter) is

$$\epsilon = 10^7 V_{SW} B^2 \left(l_o\right)^2 \sin^4\left(\theta/2\right) \tag{3.6}$$

where V_{SW} is the solar wind speed, B is IMF magnitude, $\theta = \tan\left(\frac{B_y}{B_z}\right)$ is the IMF clock angle in the plane perpendicular to the Sun-Earth line, $l_0 = 7R_E$ ($R_E = 6.38 \times 10^6\ m$) is the

Table 3.1: List of geomagnetic storms and their associated SRBs observations in SC 25 (January 2020 - June 2023), $Dst_{min} < -50\ nT$.

Year	Burst date (UT)	Burst type	Flare			LASCO/STEREO CME		Geomagnetic storm		
			Onset (UT)	Class	AR	Onset (UT)	Speed (kms^{-1})	CME impact (UT)	Dst_{min} (nT)	Kp
2020	Feb 4	....	....	....	....	....	CH	Feb 18 03:30	-52	4-
	April 15	....	....	....	....	04:24	1113	April 20 07:30	-59	5-
	July 19	....	....	....	....	....	CH	July 24 12:30	-52	4-
	Sept 23	....	....	....	....	....	CH	Sep 27 19:30	-57	5+
2021	Feb 25	....	....	....	....	....	Southern Hole	Feb 28 23:30	-58	6-
	April 14	....	....	....	.....	....	Southern Hole	April 17 01:30	-54	5
	April 22 04:38	II & IV	03:54	C3.9	AR12816	05:53	620	April 24 23:13	-53	4+
	May 9 14:32	II	14:19	C2.0	AR12822	15:05	603	May 12 10:30	-61	7
	Aug 23	....	....	....	AR12859	06:48	440	Aug 27 13:00	- 82	5
	Sep 14	....	....	....	AR12868	11:54	819	Sep 17 18:30	-64	5+
	Oct 13 11:51	III	....	....	AR12882	11:00	730	Oct 17 07:26	–55	4
	Nov 1 01:30	II & IV	00:57	M1.5	AR12887	02:00	753	Nov 3 20:25	-105	8
2022	Jan 09 22:52	II	....	....	AR12924	23:12	1283	Jan 14 16:00	-91	6-
	Jan 29 22:55	II &IV	22:45	M1.1	AR12936	23:36	530	Feb 3 00:12	-66	5+
	Jan 30	....	21:33	C1.6	AR12936	21:48	386	Feb 4 12:30	-61	5+
	Feb 6 11:51	III	11:45	C3.1	AR12939	14:00	334	Feb 10 13:53	-60	5
	Mar 10	....	Erupting Filament			18:48	742	March 13 19:30	-85	6+
	April 11 05:11	II & IV	04:59	C1.6	AR12987	05:48	940	April 14 01:17	-81	6
	May 24 22:29	II & III	21:54	C1.8	AR13014	23:12	569	May 27 12:26	-63	5
	July 5 03:59	IV	02:45	C1.8	AR13011	04:36	747	July 7 22:30	-81	5+
	July 15 15:35	IV	15:33	M1.4	AR13055	16:23	557	July 19 03:33	-61	5-
	Aug 5 00:49	III	00:43	C1.1	AR13068	01:53	591	Aug 7 04:50	-59	6-
	Oct 11 08:40	IV	08:36	M3.9	AR13112	08:36	587	Oct 14 03:36	-62	4+
	Nov 3 08:54	III	Gap	Gap	Gap	09:53	453	Nov 7 08:58	-92	5
	Dec 24 03:06	III	02:13	C1.4	AR13174	02:48	984	Dec 26 10:02	-68	4+
2023	22 Dec 30 19:17	II	19:37	M3.7	AR13176	20:24	833	Jan 3 21:50	-61	5-
	Jan 11 08:32	III	08:25	M3.1	AR13186	08:36	1047	Jan 15 07:11	-58	4-
	Feb 11 11:08	IV	10:42	M1.1	AR13220	11:12	1498	Feb 15 04:00	-72	5+
	Feb 11 11:53	III	12:28	M1.5	AR13217	13:53	815	Feb 16 11:49	-53	5
	Feb 24 13:15	III	12:58	C2.9	AR13230	13:26	922	Feb 26 19:27	-138	7-
	Feb 24 20:22	II & IV	20:03	M3.7	AR13229	20:36	1336	Feb 27 04:35	-138	7-
	Mar 20	....	14:07	C4.4	AR13258	14:00	851	Mar 23 10:21	-163	8
	Apr 21 17:55	II & IV	17:44	M1.7	AR13283	18:36	624	Apr 23 17:39	-212	8
	May 2 05:17	III	04:37	C4.3	AR13288	05:12	802	May 6 01:29	-67	6
	May 16 17:32	II & IV	16:31	M9.6	AR13307	17:24	700	May 19 19:28	-57	6-
	June 13	....	....	....	AR13326	00:23	481	June 16 02:30	-54	6

scale height [300, 285, 301]. The data for V_{SW}, B_y and B_z were taken from OMNIWeb and $\theta = \arctan(B_y/B_z)$. The IP parameters taken from OMNIWeb were also accessed and processed using the Python-based Space Physics Environment Data Analysis Software (PySPEDAS) [302].

3.6 SEPs Fluxes

The Energetic and Relativistic Nuclei and Electron (ERNE) experiment [303] aboard SOHO explores the solar atmosphere and heliosphere by identifying particles produced by several types of energy release mechanisms. The ERNE telescopes can detect energies ranging from around 1 MeV to a few hundred MeV. It is capable of recognizing elements ranging from hydrogen to zinc and distinguishing the most abundant isotope. The ERNE sensor unit has two detector telescopes: the Low Energy Detector (LED) and the High Energy Detector (HED). LEDs operate in the low energy range of 1.3 to 13 MeV. HED detects protons with energies ranging from 11 to 120 MeV, as well as heavier nuclei between 11 and 540 MeV.

The third objective was initiated by selecting high-energy solar proton events (hereafter referred to as large events) that affected the Earth's atmosphere have been listed using the NOAA SWPC database (https://www.ngdc.noaa.gov/stp/space-weather/interplanetary-data/solar-proton-events/%20page%20code.html). This database provides solar proton events with energies >10 MeV and fluxes greater than or equal to 10 Particle Flux Units (pfu), measured by GOES spacecraft at geosynchronous orbit. Using this database, a list of 122 large events was compiled from 1997 to 2024. During the selection and listing of large events, some were found in the catalogs provided by Kouloumvakos et al. [304] and Ameri et al. [305]. The particle flux intensities were obtained from ERNE/SOHO from: https://cdaweb.gsfc.nasa.gov/. We calculated the inverse speed ($\beta^{-1} = \frac{c}{v(E)}$) values for all energy channels of HED and manually determined the onsets of each particle event by plotting the particle fluxes versus time and zooming in to identify where the fluxes began rising above the background in the sensor. The onsets were then plotted against the inverse speeds across the energy channels a method called velocity dispersion analysis (VDA) [306]. This technique helped estimate the release times (t_0) and apparent path lengths (L) of SEP events from the Sun. At 1 AU, the VDA equation is as follows:

$$t_{onset}(E) = t_0 + 8.33\frac{min}{AU}L\beta^{-1}(E) \tag{3.7}$$

where $t_{onset}(E)$ is the observed onset time in minutes at proton kinetic energy E, t_0 is the release time (in minutes) from the acceleration region, L is the apparent path length (AU) traveled by the particles, and $\beta^{-1}(E)$ is the inverse speed of the particles at energy E. The linear fitting of the onset timings as a function of the related inverse speed estimates the release time (t_0) as the vertical intercept, and the path length (L) was determined from the graph's slope (s) as $L = s/8.33$. The error bars, obtained by subtracting the linear fitting model from the data points and scaling them down by a constant fractional value, were added to the graph to indicate uncertainties in the calculations. Next, we evaluated the appearance of associated SRBs observed from the ground using e-CALLISTO and CESRA, along with their space-based counterparts using WAVES/STEREO. We also examined their association with GOES soft X-ray flare characteristics via Solar Monitor, as well as CMEs from the LASCO/SOHO catalog and SEEDS. For the purpose of identifying patterns in the occurrence of SEP events, three solar cycles were plotted using sunspot numbers obtained from the World Data Center SILSO, Royal Observatory of Belgium, Brussels [307].

3.7 Summary

This chapter discussed the data sources and the underlying methods used to process them, organized according to the objectives of the study.

Chapter 4

Monitoring Solar Activity Using Low-Frequency Solar Radio Emissions

---

This chapter utilizes low-frequency SRBs, recorded during the ascending phase of SC 25, to assess solar activity as inferred from radio emissions. The analysis focuses on type II to type IV bursts in alignment with the study's objectives. Observations from e-CALLISTO spectrometers were used to investigate the relationship between solar activity and SRB emissions, as well as the connections between these bursts, geomagnetic storms, and large SEP events. The results have been published in Ndacyayisenga et al. [308, 309, 310].

4.1 Introduction

Radio observations play a crucial role in advancing our understanding of solar activity, its influence on IP medium, and its impact on the solar-terrestrial environment [311]. Solar radio emissions arise from magnetic activity in the Sun's atmosphere, driving plasma acceleration and heating processes that manifest as various dynamic phenomena [5, 312]. These emissions are primarily observed as type II, III, and IV radio bursts, which carry diagnostic information about the energetic events that generate them [5, 313]. They are often associated with SFs, powerful eruptions that release high-energy electrons, ions, and atoms into space [237]. Although flares are generally required for SRB generation, not every flare produces a detectable SRB, and their occurrence does not strictly depend on the flare's intensity [314]. CMEs constitute the most prominent large-scale manifestations of solar activity, marked by the destabilization of extended coronal structures. Radio emissions in the metric domain are frequently associated with CMEs, even in the absence of concurrent SFs. Observations revealed close spatial and temporal correlations between enhanced noise storm activity and white-light transients such as CMEs or localized coronal mass accumulations near the radio emission source [315]. CMEs are typically associated with m - type II radio bursts [184, 199, 316] and type IV radio bursts [317, 49, 318]. CMEs are also driver of geomagnetic storms and can accelerate SEP events. SEPs are currently classified into two paradigms: gradual events, which are accelerated by CME or IP shocks [319, 320], and impulsive events, which result from magnetic reconnection at flare sites in the corona [321]. This classification is based on various observational characteristics at 1 AU, such as timescales, energy spectra, elemental composition and charge states, and associated radio emissions. Fundamentally, two main acceleration mechanisms are responsible for SEPs: magnetic reconnection and shock-wave acceleration [322, 323]. Magnetic reconnection in SFs or jets may result in impulsive and narrowly-distributed events [320, 324, 325]. In contrast, the formation and eruption of magnetic flux as CMEs particularly fast CMEs can drive forward-propagating shock waves that accelerate particles upstream, leading to extended and widespread gradual events. Previous investigations have established connections between SRBs and energetic particles observed in situ, based on factors such as the presence of radio signatures [326], duration of events [324], and specific spectral properties [327]. The solar radio frequency domain offers a powerful remote-sensing diagnostic capability for exploring the nature of particle drivers, acceleration processes, and propagation patterns. The significance of different types of radio bursts to space weather forecasting is elaborated in Warmuth and Mann [167]. Numerous studies have explored the relationship between type II, III, and IV radio bursts and SEP events. For instance, Lin [328] found that about 70% of SEP events from 1964 to 1967 were associated with type II and III radio bursts. Similarly, Švestka and Fritzová-Švestková [329] reported that nearly all type II bursts observed between 1966 and 1968 corresponded to SEP events. Nevertheless, Kahler [326] noted that only around half of the m - type II bursts originating from the western solar hemisphere showed a clear connection to SEPs. While both coronal and IP shock waves are widely accepted as the dominant accelerators behind large SEP events, it is important to acknowledge that not all coronal shocks are efficient in this role [330]. A statistical assessment by Cliver et al. [331] indicated that SEPs (with energies around ~ 20 MeV) detected near Earth were closely linked to coronal shock waves, particularly those evidenced by m-type II bursts accompanied by decametric-hectometric (DH) counterparts. In a further analysis dividing SEP events into gradual and impulsive categories, Cliver and Ling [332] observed that type III bursts were present in every case, although impulsive events typically lacked DH-type II radio bursts (with just one exception). High occurrence rates of m- ($\sim 90\%$) and DH-type II bursts (100%) during intense SEP events were reported by Gopalswamy [333], Cliver et al. [331] and Cliver and Ling [334]. In a study by Miteva et al. [335], approximately 75% of $\sim$25 MeV proton events were associated with both m- and DH-type II bursts, and nearly 60% with IVm bursts (see their Table 4). Papaioannou et al. [336] found strong correlations between SEP events and SRBs: 74% (with a 5% margin) with DH type II bursts, 83% with type III bursts, and 35% (plus 7% potentially associated) with type IV bursts, based on data spanning from 1997 to 2013. Building on previous research, the present study aimed to assess the strength of solar activity using SRB observations and to enhance our understanding of SEP activity as SC 25 progresses.

4.2 Solar radio type II bursts and solar activity of SC 25

The e-CALLISTO network detected a series of solar radio type II bursts ranging from 10 MHz to 400 MHz during the ascending phase of SC 25. Table 4.1 lists the spectrometers used for type II burst observations, along with their geographic locations, frequency ranges, and the number of radio bursts recorded at each station. All spectrometers operate within a narrow frequency band of a few tens of MHz. The shock characteristics of each radio event were estimated using the radio parameters described by Equations 2.15 to 2.19. Table 4.2 presents each type II radio burst along with its associated CME, GOES soft X-ray flare, and shock characteristics. The first column of the table lists the event index. The next four columns provide details of the radio events, including the date and time (dd/mm/yyyy hh:mm), starting frequency in MHz, frequency drift rate in MHz/s, and the estimated shock formation height in solar radii, $r(R_{\odot})$ based on Equation 3.2. Columns 6 to 9 contain GOES soft X-ray flare parameters: start time, flare class, NOAA active region, and

Table 4.1: e-CALLISTO Spectrometers, their geographical locations and their frequency ranges.

#	File ID	Country	Lat(deg)	Long (deg)	Obs. Freq (MHz)	# events
1	Australia_ASSA	South Australia	-30.00	136.21	15 — 87	11
2	Arecibo_Observatory	Puerto Rico, USA	18.22	-66.59	15 — 87	9
3	GREENLAND	Greenland	67.00	-50.72	10 — 110	3
4	ALASKA_HAARP	ALASKA	64.84	-147.72	5 — 87	2
5	ALMATY	Kazakhstan	43.22	76.83	45 — 165	1
6	BIR	Ireland	16.61	77.51	10 — 100	2
7	INDIAN_OOTY	India	11.41	76.69	45 — 165	1
8	KASI	South Korea	36.35	127.38	150 — 400	1
9	MEXICO_LANCE	MEXICO	19.81	-101.69	50 — 90	1
10	SWISS-Landschlacht	Switzerland	47.63	9.25	15 — 87	1

flare location. The following two columns report the CME onset time and speed. Columns 12 to 15 detail the shock properties: density jump (χ), Mach number (M_A), shock speed (V_s), and Alfvén speed (V_A) while the final column gives the estimated ambient magnetic field strength (B-field) in Gauss. The analysis of the aforementioned radio events revealed a strong correlation ($CC = 0.98$) between the drift rates and starting frequencies of type II radio bursts, which are critical parameters for estimating shock speeds from dynamic spectra. The starting frequencies and drift rates are empirically related by the expression $\frac{df}{dt} = -0.001 f^{1.19}$. Higher starting frequencies are associated with higher drift rates [337]. This correlation is consistent with previous studies, which reported slopes of $\epsilon = 1.89$ and $\epsilon = 1.33$, respectively [e.g., 228, 337]. Table 4.2 shows that 4 out of 32 radio events were not associated with any SF because they originated from the far side of the solar surface; however, the shocks that generated these bursts were driven by associated CMEs. It is also noted that 18 out of 27 events were associated with intense GOES X-ray flares (M- and X-class), consistent with their speeds and the estimated shock speeds. The shock and Alfvén speeds of these type II radio bursts were calculated to be in the ranges of 504 - 1282 kms^{-1} and 368 - 826 kms^{-1}, respectively, at a heliocentric distance of $\sim 1 - 2\ R_\odot$. These values are consistent with measurements reported in Cunha-Silva et al. [338], Minta et al. [339], which indicated speeds of about 590 - 810 kms^{-1} and 250 - 550 kms^{-1}, respectively, at $\sim 1.2 - 1.8\ R_\odot$. The current results also agree with the Alfvén speed ranges of 140 to 460 kms^{-1} over 1.2 – 1.5 $\mathrm{R}_\odot$ [340] and 259 – 982 kms^{-1} over 3 - 15 $\mathrm{R}_\odot$ [55]. The correlation between the speeds obtained from the LASCO FOV and those derived from the dynamic spectra is shown in Figure 4.1. According to the observations from Table 4.2 and Figure 4.1, there are instances where the estimated shock speeds are faster than the CME speeds from LASCO FOV, and vice versa. The difference in CME speed observed by LASCO and those derived from dynamic spectra is attributed to the central position angles of the CMEs, suggesting that the shock may have weakened and dissipated before entering the LASCO FOV [54]. A shock also slows down when its intensity decreases or when it dissipates. It should be noted that type II radio emission can originate from either the nose or the flanks of the shock front, depending on where electron acceleration is most efficient [56]. The theory behind solar radio type II bursts associated with slow CMEs proposes that these bursts result from the

Table 4.2: Type II radio bursts observed by e-CALLISTO during the ascending phase of SC 25 and their associated CMEs, GOES soft-Xray flares and estimated shock characteristics.

No	Type II burst event				Soft X-ray flare				CME		Shock characteristics				B-field
	Date (UT)	f (MHz)	Drift rate $(MHzs^{-1})$	height $R_\odot$	Start (UT)	Class	NOAA	Location	Onset (UT)	Speed (kms^{-1})	χ	M_A	V_s (kms^{-1})	V_A (kms^{-1})	G
1	22/05/2021 02:57	86	- 0.13	1.4	02:47	C6.1	12824	N18E25	......	.....	1.6	1.5	752	504	1.5
2	23/06/2021 07:05	73	-0.10	1.5	06:43	C3.4	12833	N14E89	07:24	390	1.5	1.4	668	464	1.2
3	25/07/2021 04:54	64	-0.11	1.5	.....	....	F. S.	......	05:48	237	1.3	1.2	785	637	1.6
4	28/08/2021 05:10	64	-0.11	1.5	05:01	C7.0	12860	S31E06	.....	.....	1.7	1.6	894	556	1.2
5	09/10/2021 06:34	75	- 0.11	1.5	06:19	M1.6	12882	N18E06	07:00	712	1.6	1.5	735	496	1.3
6	09/10/2021 06:49	31	- 0.04	1.9	06:19	M1.6	12882	N18E06	07:00	712	1.3	1.3	706	561	0.7
7	28/10/2021 15:28	90	-0.18	1.4	15:17	X1.0	12887	S26W07	15:48	1519	2.0	1.8	1273	697	1.6
8	20/12/2021 11:27	87	- 0.14	1.4	11:12	M1.8	12908	S20W01	12:36	386	1.7	1.6	750	479	1.5
9	12/01/2022 04:28	69	- 0.11	1.5	.....	....	F. S.	......	03:12	433	1.8	1.7	816	479	1.1
10	12/02/2022 08:33	173	- 0.36	1.2	08:25	M1.4	12939	S17W82	08:12	785	1.3	1.2	792	659	4.1
11	02/03/2022 17:42	67	- 0.11	1.5	17:31	M2.0	12958	N15E29	18:24	248	1.9	1.7	924	532	1.1
12	14/03/2022 17:20	98	- 0.13	1.4	17:13	B8.5	12964	S30W86	17:48	534	1.9	1.7	883	506	1.2
13	25/03/2022 05:15	66	- 0.12	1.5	05:02	M1.4	12974	S18E37	06:12	433	1.5	1.4	801	590	1.6
14	28/03/2022 11:23	87	- 0.15	1.4	10:58	M4.0	12975	N18W04	12:12	335	1.8	1.7	951	554	1.4
15	30/03/2022 17:33	72	- 0.11	1.5	17:21	X1.3	12975	N13W31	18:00	493	1.9	1.8	1128	654	1.1
16	31/03/2022 18:34	67	- 0.13	1.5	18:17	M9.6	12975	N12W47	19:12	489	2.0	1.8	1081	594	1.3
17	02/04/2022 13:24	71	- 0.15	1.5	12:56.	M3.9	12975	N12W68	13:36	686	1.8	1.6	1038	631	1.5
18	17/04/2022 03:28	382	- 0.83	0.9	03:17	X1.1	12994	N12E88	03:48	728	1.2	1.2	828	711	7.8
19	21/04/2022 02:00	85	-0.15	1.4	01:47	M9.6	12993	N22E23	02:36	828	1.7	1.5	1070	696	1.6
20	21/04/2022 22:47	69	-0.11	1.5	22:39	C1.6	12993	N12E25	23:12	389	1.4	1.3	791	591	1.4
21	30/04/2022 13:46	83	-0.13	1.4	13:37	X1.1	12994	N16W88	14:00	535	1.7	1.5	936	610	1.4
22	30/04/2022 19:50	80	-0.12	1.4	19:42	M1.9	12994	N16W88	20:12	793	1.7	1.6	855	543	1.3
23	04/07/2022 13:35	69	-0.13	1.5	12:23	C5.1	13050	N17E36	11:36	256	1.7	1.6	918	581	1.4
24	05/07/2022 04:16	69	-0.10	1.5	03:59	C9.8	13045	S20W18	05:00	515	1.6	1.5	761	512	1.2
25	14/08/2022 12:05	70	-0.08	1.5	11:50	C2.4	13076	N21W14	13:25	411	1.4	1.3	512	402	1.1
26	18/08/2022 12:12	62	-0.16	1.6	.....	....	F. S.	......	11:00	1131	1.7	1.6	1282	826	1.9
27	19/08/2022 04:35	81	-0.10	1.4	04:14	M1.6	13078	S27W48	04:49	695	1.3	1.2	504	420	1.4
28	23/09/2022 18:02	67	-0.12	1.5	17:48	M1.7	13110	N16E84	18:12	687	2.0	1.8	1010	548	1.1
29	29/09/2022 12:06	80	-0.10	1.4	11:50	C5.7	.....	N26E86	12:24	321	1.5	1.4	672	473	1.2
30	09/11/2022 20:03	89	-0.11	1.4	.....	....	F. S.	......	20:36	371	1.5	1.4	618	435	1.3
31	03/12/2022 17:44	84	-0.13	1.4	17:36	M1.2	13157	N14E89	.....	.....	1.8	1.8	857	518	1.3
32	14/12/2022 08:30	160	-0.22	1.2	08:24	M1.1	13162	S16W89	08:48	402	1.9	1.8	657	368	1.7

interaction between slow CMEs and the background magnetized coronal plasma, which accelerates non-thermal electrons through moving magnetic reconnection [341]. Furthermore, the observation of a type II radio burst is additional evidence of shock acceleration in the solar corona, according to a recent study [191].

The Alfvén Mach numbers in the range of approximately $\sim 1.2 - 1.8$ at $\sim 1 - 2$ $\mathrm{R}_\odot$ are consistent with measurements of about 1.1 - 1.9 at $\sim 1.3 - 2.5$ R$\odot$ reported by Vršnak et al. [228], and with values reported by Cunha-Silva et al. [338], which range from 1.4 to 1.7 at $\sim 1.2 - 1.8$ $\mathrm{R}_\odot$. The magnetic field strength is an important parameter influencing the dynamic eruption of CMEs in the solar atmosphere [e.g., 57, 243]. High-starting type II radio bursts are associated with coronal shocks occurring closer to the solar surface, where higher magnetic field strengths are expected. Figure 4.2 illustrates the variation in magnetic field strength estimated in this study (Equation 2.19), in comparison to both the quiet Sun magnetic field model, $B(r) = \frac{a}{r^2}$ with $a = 2.2$ [51], and an empirical model for active regions, $B(r) = 0.5\,(r-1)^{-1.5}$ [50]. The magnetic field was calculated in the range $0.5 < B < 8\ G$ at $\sim 1 - 2$ $\mathrm{R}_\odot$, which shows excellent agreement with previous studies and is well-modeled by $B(r) = 6.07r^{-3.96}\ G$ at $\sim 1 - 2\ R_\odot$, as shown by the black dotted curve in Figure 4.2. The Rankine – Hugoniot jump conditions have been widely used to derive shock parameters. Using this method, for example, Smerd et al. [213, 342] found

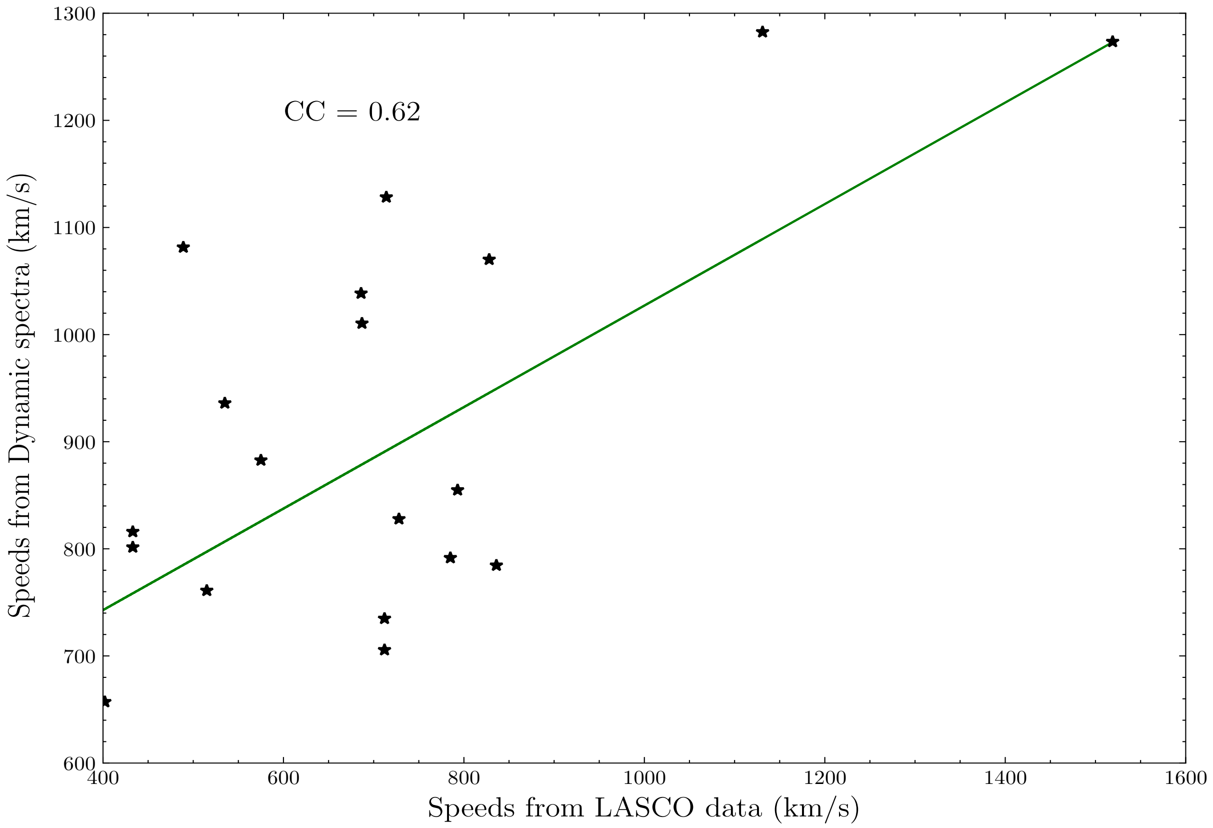

Figure 4.1: Scatter plot illustrating the correlation between LASCO FOV speeds and speeds derived from dynamic radio spectra. The higher speeds observed in the dynamic spectra are attributed to radio sources propagating faster as a result of interactions between slow CMEs and the ambient magnetized coronal plasma [341].

$1.2 \leq \mathrm{M_A} \leq 1.7$ and $0.3 \leq \mathrm{B} \leq 4$ G. Similarly, Vršnak et al. [228] reported magnetic field strengths between 1 and 8G at a $\sim\ 1.6R_\odot$. According to Ramesh et al. [53], the magnetic field ranges from 5 to 6G at $\sim 1.5 - 1.77\ R_\odot$. A comprehensive analysis of coronal magnetic fields, measured using various methods and wavelengths across the electromagnetic spectrum, has been provided by Dulk and McLean [50] and Sasikumar Raja et al. [60]. A recent study by Chernov and Fomichev [191] identified two prerequisites for type II radio emission: (i) a perpendicular shock wave and (ii) a relatively strong shock (with Mach number exceeding a critical value $\mathrm{M_{cr}}$). The Mach numbers obtained in this study ($1.2 \leq \mathrm{M_A} \leq 1.8$) are consistent with these requirements. The statistical results of this study were compared and summarized with those of previous studies involving more than two radio events in Table 4.3.

Table 4.3: Comparison of statistical results from this study with previous analyses involving multiple radio events.

Epoch	Events #	Mean shock speed (km/s)	Mean Alfvén speed (km/s)	B-field range (G)	Height range ($R_\odot$)	Authors
2021 – 2022	31	860	566	8 – 0.6	1.0 — 2.0	This work
2013 – 2014	4	739	579	1.8 – 1.3	1.7 – 1.9	Kishore et al. [58]
1996 – 2007	10	1288	555	0.105 – 0.006	3 – 15.	Kim et al. [55]

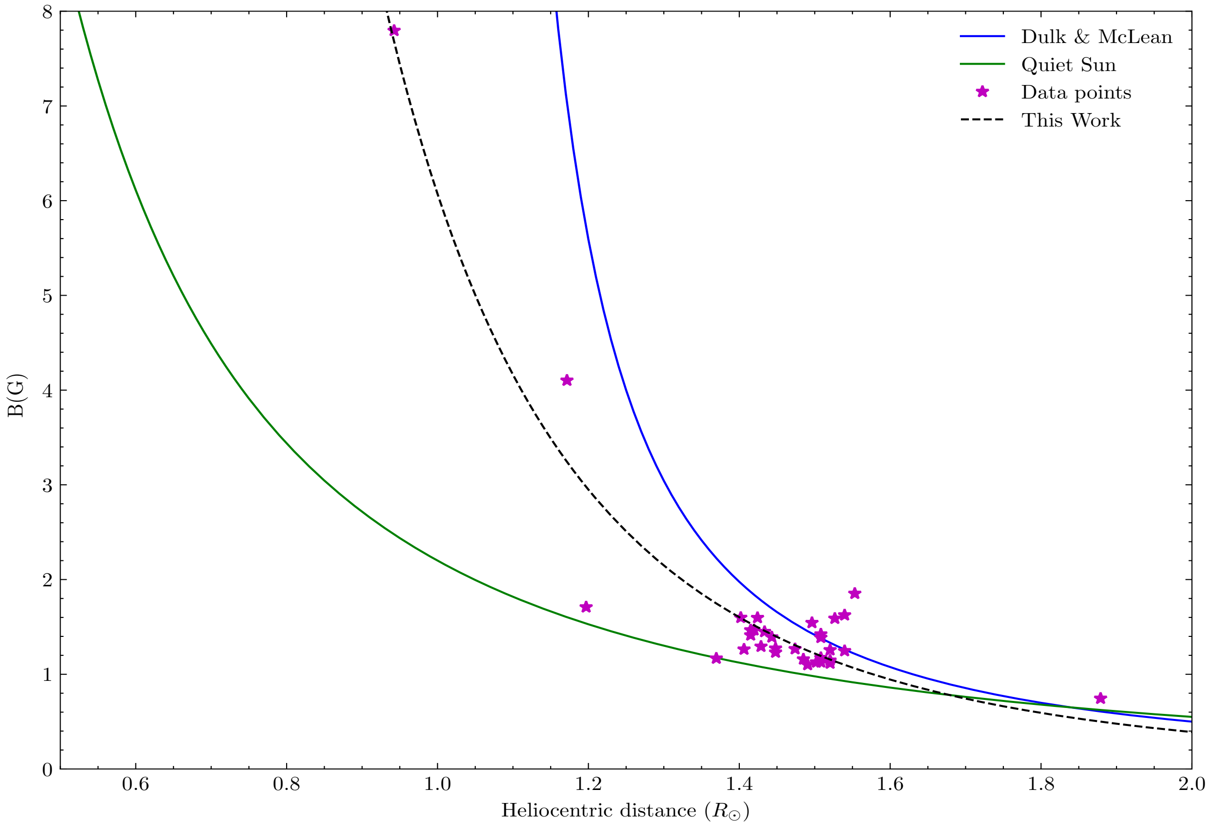

Figure 4.2: Comparison of magnetic field strength from this study with the quiet Sun magnetic field model [51] and the empirical relation by [50]. The estimated values exceed those of the quiet Sun model and closely follow the empirical trend, indicating elevated solar activity.

Thus, this analysis shows that the Sun was highly active during the ascending phase of SC 25 in terms of type II radio emission occurrences.

4.3 Geomagnetic Storms and Solar Radio Emissions of SC 25

This section presents the results of a correlative analysis between geomagnetic storms and solar radio emissions during the ascending phase of SC 25.

4.3.1 Statistical Analysis

Twenty-three out of thirty-five geomagnetic storms ($Dst_{min} < -50\,nT$) were preceded by solar radio emissions, and three of the four severe geomagnetic storms ($Dst_{min} < -100\,nT, Kp_{max} \geq 7$) were preceded by SRBs during the ascending phase of SC 25, indicating that SRBs could be used as observational proxies to track the occurrence of geomagnetic storms. The average time interval between the onset of the SRB and the effects of the CME and/or the HSS on the Earth's magnetosphere is 79 hours, within a range of 48 to 120 hours depending on the dynamics of their origins. Strong solar wind streams that arise from huge coronal holes on the solar surface drove five geomagnetic storms. With an average speed of about 755 km/s, CMEs were the source of the remaining geomagnetic storms. The Kp index, which runs from 0 to 9, represents horizontal geomagnetic field disruption and $K_p \geq 5$ reveal the occurrence of a geomagnetic storm and 28 geomagnetic storms were ascertained as shown in Table 3.1. The NOAA scale for geomagnetic storms, or G index, is correlated with the Kp index. G index values are 1 to 5, with Kp=5 corresponding to G=1 and so forth. The $K_p = 8$ & 9 denote severe and extreme geomagnetic storms, respectively. Two extreme (G5) geomagnetic storms occurred on 11 May 2024 and 10 October 2024, respectively, after the completion of the current analysis. SC 24 had only six severe geomagnetic storms, while SC 25 had nine during its rising phase at the time of writing this thesis [343]. In the following section, four severe geomagnetic storms $(Dst_{min} < -100\ nT)$ are used as examples. These are the dates: 24 April 2023, 24 March 2023, 4 November 2021, and 27 February 2023.

4.3.2 The 21 – 24 April 2023 events

On 21 April 2023, a type II radio burst was detected by the CALLISTO station at Arecibo Observatory (Puerto Rico, USA, $18.22°$N, $66.59°$S) between 17:55 UT and 18:11 UT. This burst was overlapped by a type IV burst from 17:59 UT to 18:14 UT, followed by another type II burst from 18:15 UT to 18:18 UT, as shown in Figure 4.3. No corresponding space continuation was observed during this period. These bursts were linked to a GOES soft X-ray flare of class M1.7, detected at 17:44 UT, originating from the AR13283 active region. A CME was observed in the LASCO FOV coronagraph at 18:36 UT and in STEREO-A/COR1 at 18:23 UT, near the flare's end. Figure 4.4 shows (a) the GOES soft X-ray flare timeline and intensity, (b) the 94 $\AA$ wavelength AIA image overlaid with the HMI for the active region, (c) the CME structure in the SOHO/LASCO C2 FOV, and (d) the same CME in the STEREO-A/COR 2. One can believe that type IV radio burst observed in Figure 4.3 were associated with the flux rope shown in Figure 4.4 (c) or (d), which is consistent with Gopalswamy et al. [344], who demonstrated that CME is critical for the

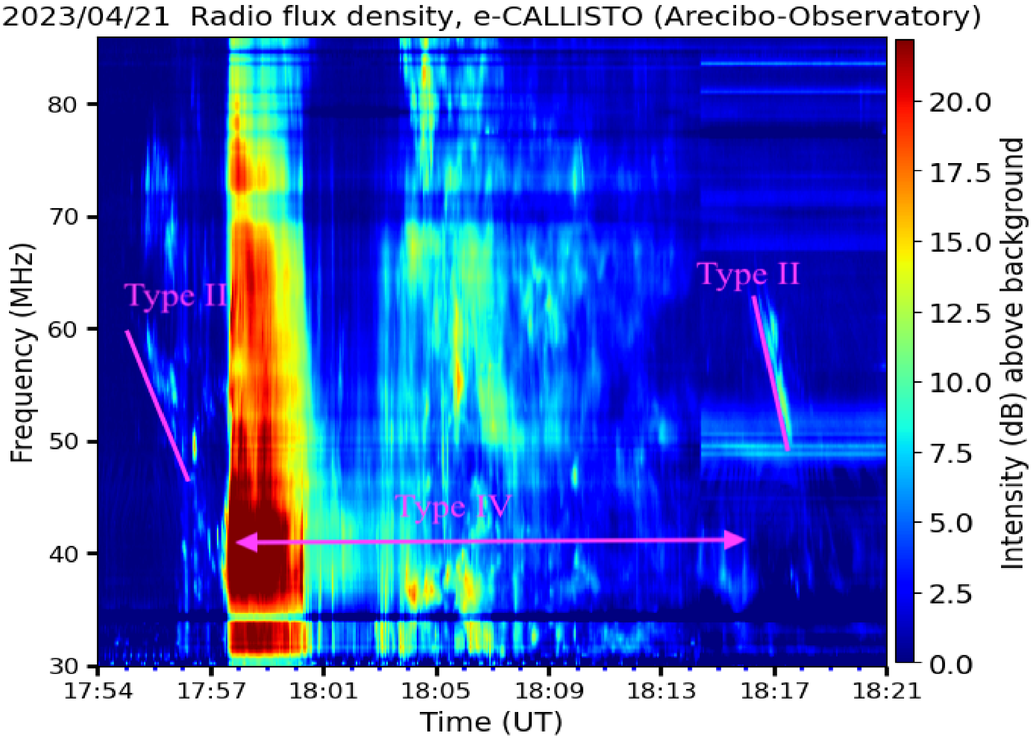

Figure 4.3: Type II bursts from 17:55 UT to 18:11 UT, overlapped by a type IV burst from 17:59 UT to 18:14 UT, followed by another type II burst from 18:15 UT to 18:18 UT on 21 April 2023.

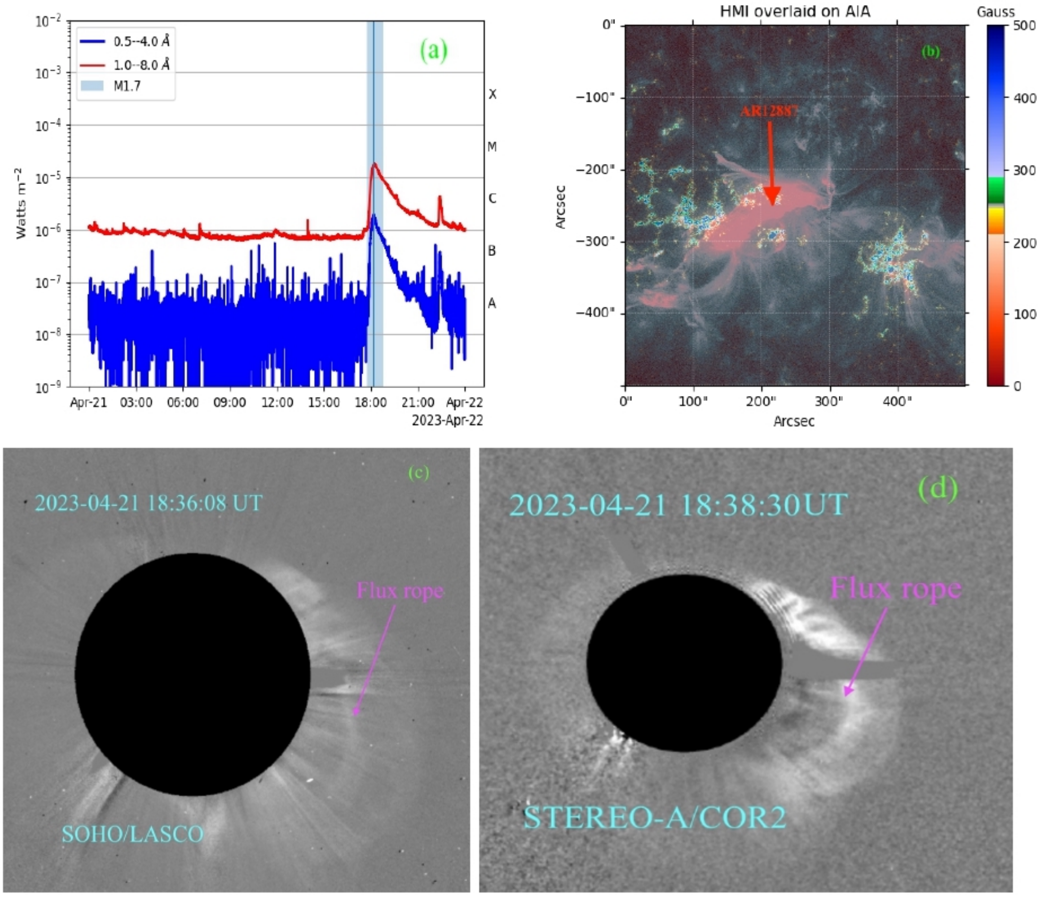

Figure 4.4: (a) The timeline of GOES X-ray flares on 21 April 2023. (b) The position of the associated active region AR12887 on the solar disc, overlaid with the HMI. (c) A 15-minute difference image of the CME captured by the SOHO/LASCO-C2 coronagraph on 21 April 2023 at 18:36 UT. (d) A 15-minute difference image of the same CME taken by STEREO-A/COR1 at 18:23 UT. The black circles represent the coronagraphs' occulting discs. The CME observed by SOHO/LASCO-C2 appears fainter than the one observed by STEREO-A/COR2, as the central position angle of the CME with respect to the plane of the sky is greater for SOHO/LASCO. In all images, the magenta arrows point to the flux ropes that are radially expanding.

occurrence of type IV bursts and that moving type IV bursts are associated with moving flux ropes of CMEs. Studies by Mel'nik et al. [345] and Vourlidas et al. [346] demonstrated that moving type IV bursts have a drift rate greater than 0.03 MHz/s and are short-lived, while stationary bursts exhibit a drift rate less than 0.03 MHz/s and can last from several minutes to several hours. Based on this classification, type IV radio burst observed from 17:59 UT to 18:14 UT had a drift rate of 0.06 MHz/s, indicating that it was a moving type IV burst (Figure 4.3). The partial halo CME shown in Figure 4.4 (c) or (d) impacted the Earth's magnetosphere on 23 April 2023 at 17:39 UT, as indicated by the red solid line in Figure 4.5, leading to the first severe geomagnetic storm (G4) of SC 25 since 2019. During this storm, the northern hemisphere witnessed by large and intense auroras. Severe geomagnetic storms often lead to disturbances in power grids, spacecraft, GPS systems, and radio communications. Figure 4.5 illustrates the variation of (a) the z-component of the magnetic field, (b) solar wind speed, (c) solar wind energy input to the magnetosphere –

ionosphere (ϵ parameter), and (d) the geomagnetic SYM-H index (a proxy for ring current intensity) from 16:00 UT on 23 April to 12:00 UT on 24 April 2023.

Figure 4.5: Solar wind parameters and geomagnetic activity from 23 – 24 April 2023. (a) z-component of the interplanetary magnetic field (IMF), (b) solar wind speed, (c) ϵ parameter, and (d) SYM-H index, which reflects geomagnetic field fluctuations, all shown with 1-minute resolution from OMNIWEB data. The arrival of the fast forward IP shock is marked by the solid red vertical lines (a – d). The storm development begins at the impact, indicated by the period between the red and green vertical lines. The lowest SYM-H index reached is -233 nT at 04:05 UT.

Figure 4.5 indicates that B_z fluctuated between 17:39 UT until 20:52 UT and then turned northwards until 01:44 UT on 24 April 2023 when it turned back and attained a minimum value of -30 nT which enhanced the phase of the storm. The epsilon parameter (ϵ) accounts for the part of energy budget consumed in the storm and substorm process [347]. At the CME impact, the $\epsilon = 1.8 \times 10^{13}$ W and during the development of the storm the consumption rate reached a maximum value of 1.5×10^{14} W. As stated in Akasofu [285], the input energy rate during magnetic storms can exceed 10^{12} W and may occasionally reach up to 10^{13} W. Consequently, the ϵ values are crucial for this storm. Additionally, it has been shown that the total solar wind pressure (both magnetic and kinetic) in SC 25 is higher than in SC 24 but lower than in SC 23 [66].

4.3.3 The 20 – 24 March 2023 events

In contrast to the previous geomagnetic event, the current storm was observed without any solar radio activity. On 20 March 2023, two halo CMEs were detected by the SOHO LASCO C2 coronagraph at 14:00 UT and 14:42 UT, with speeds of 851 km/s and 727 km/s, respectively, as they left the Sun and moved toward Earth. These CMEs were associated with a C4.4 flare and a C1.5 flare, both originating from the same NOAA active region AR13258. Figure 4.6 below presents 15-minute running difference images of the two CMEs in the SOHO LASCO C2 FOV, with both showing expanding flux ropes. On 23 March 2023, both CMEs impacted the Earth's magnetosphere at different times, triggering the second severe (G4) geomagnetic storm of SC 25. In-situ data showed that the first CME arrived at 10:21 UT and the second at 17:41 UT on the same day.

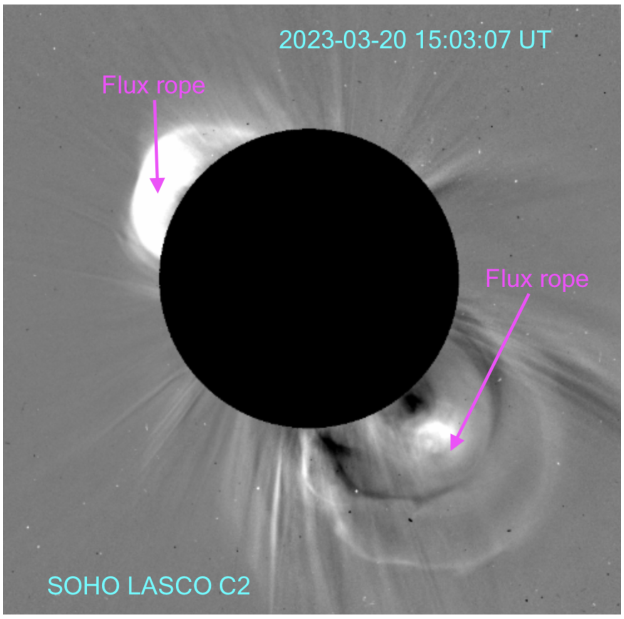

Figure 4.6: SOHO/LASCO-C2 15-minute difference images of the CMEs observed on 20 March 2023 at 14:00 UT and 14:42 UT. The black circles represent the coronagraphs' occulting discs. These CMEs were not detected by STEREO-A. In all images, the magenta arrows highlight the radial expansion of the flux ropes.

4.3.4 The 1 – 4 November 2021 events

Figure 4.7 illustrates the radio emissions recorded on 1 November 2021. Panel (a) shows the dynamic spectrum captured by the CALLISTO station at the Astronomical Society of South Australia (ASSA), while panel (b) presents the corresponding extended space-based observation from WIND/WAVES, covering the frequency ranges of 15 – 68 MHz and 0.014 – 16 MHz, respectively. These radio emissions were associated with M1.5 Class GOES soft X-ray flare from 00:57 UT to 02:10 UT (with peak emission at 01:45 UT) from active region AR12887, which was located at the heliocentric coordinates S29W45. This suggests that the initiation of the type II burst at 01:30 UT and the type IV burst at 01:38 UT, shown in Figure 4.7, occurred near the flare's peak intensity. Figure 4.8 displays: (a) the timing of the GOES soft X-ray flare; (b) the AIA 131 $\AA$ image overlaid with HMI data, highlighting the strength of the corresponding active region; (c) 15-minute running difference images showing the CME's expansion captured by SOHO/LASCO-C2; and (d) the same CME progression observed by STEREO-A/COR1. Given that the CME originated in the same active region and propagated in the radial direction, this active region must be responsible for the non-thermal electrons required for radio emissions in Figure 4.7 [245]. The flare and radio emissions shown in Figure 4.7 were associated with a CME observed by SOHO/LASCO-C2 between 02:00:06 UT and 03:48:05 UT, featuring a central

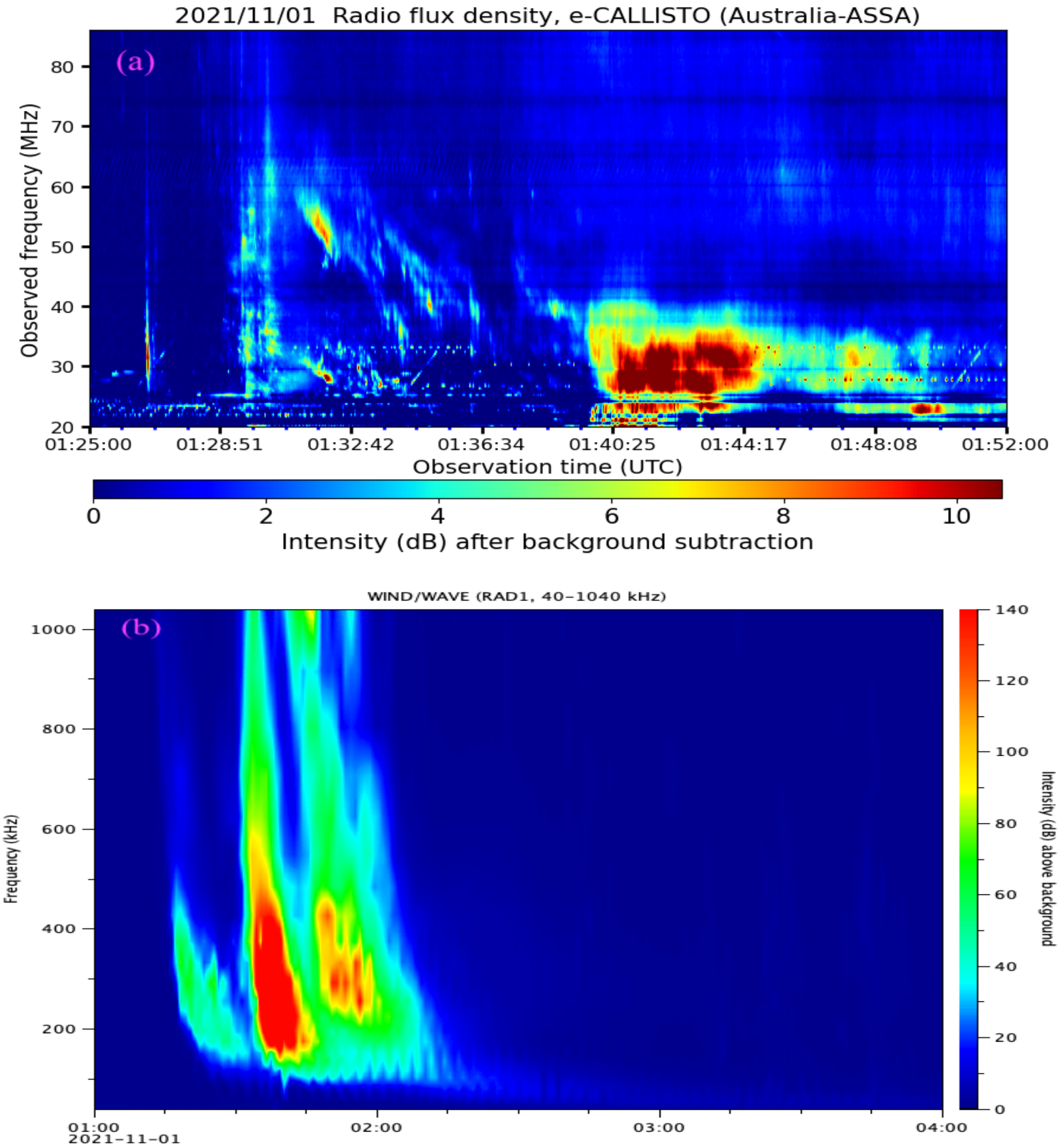

Figure 4.7: (a) Type III radio burst observed from 01:26 to 01:30 UT, followed by a Type II burst from 01:30 to 01:36 UT, and a Type IV burst spanning 01:38 to 01:52 UT on 1 November 2021. (b) Continuation of the Type II and Type IV bursts into the interplanetary medium, detected below the ionospheric cut-off frequency by the Wind/WAVES spacecraft.

position angle (measured counterclockwise from solar north) of $192°$ and an angular width of $142°$. Meanwhile, STEREO-A/COR1 recorded the same CME from 01:53:30 UT to 04:23:30 UT, with a position angle of $221°$ and a broader angular width of $212°$. In the two cases, the projected heliocentric distances of the CME were 2.7 $R_\odot$ and 3.1 $R_\odot$, respectively. The first CME's onset was predicted to occur at 01:14 UT according to the historical epoch of the STEREO-A/COR 1, which observes the Sun between 1.3 and 4 $R_\odot$, and at 01:12 UT according to the SOHO/LASCO-C2, which observes the Sun between 2.5 and 6 $R_\odot$. It is plausible to suggest that the shock wave responsible for the type II radio emission was generated by MHD waves driven by the associated CME, while the type IV radio emission originated from electrons confined within the CME's magnetic field lines [10]. Additionally, the expansion of the CME's flux rope

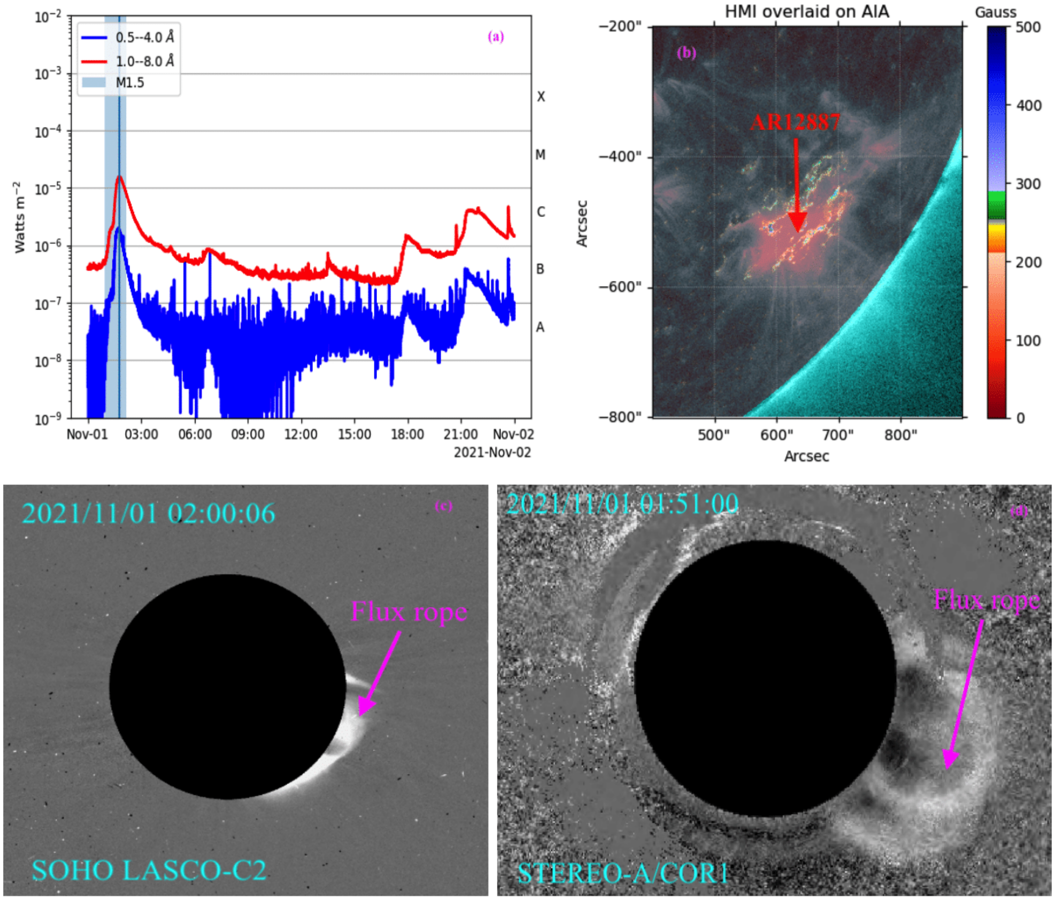

Figure 4.8: Timeline of GOES X-ray flares on 1 November 2021. (b) Location of the corresponding active region, AR12887, marked by a dotted magenta circle on the solar disk and overlaid with HMI imagery. (c) SOHO/LASCO-C2 15-minute running difference coronagraph image showing the CME at 02:00:06 UT. (d) A 15-minute difference image of the same CME captured by STEREO-A/COR1 at 01:51:00 UT. The black circles represent the coronagraphs' occulting discs. The CME appears dimmer in the STEREO-A view due to its larger central position angle relative to the plane of the sky. Magenta arrows in all images point to the radially expanding flux ropes.

may further enhance the occurrence of type IV radio emissions [346]. In this study, type IV radio burst illustrated in Figure 4.7 was classified as a moving type IV burst, characterized by a frequency drift rate of 0.04 MHz/s and a duration of 14 minutes within the 15 – 47 MHz range. Observations from two spacecraft indicated CME velocities of 753 km/s and 604 km/s, respectively. Meanwhile, type II burst associated with this CME exhibited a drift rate of 0.09 MHz/s, from which a shock speed of approximately 833 km/s was derived (Equation 2.14). The discrepancy between the CME speeds inferred from the dynamic spectrum of the type II burst and those measured by LASCO-C2 or STEREO-A/COR1 may be due to the CME's central position angle relative to the plane of the sky, suggesting that the shock could have weakened or dissipated before entering the fields of view of LASCO and STEREO [54]. On 4 November 2021, a partial halo CME aligned along the Sun–Earth line impacted Earth's magnetosphere, initiating a significant geomagnetic storm of SC 25. In-situ measurements showed that the Kp index reached a 3-hour average of 8 on that day. The fast forward IP shock arrived at Earth's orbit at 20:24 UT on 3

November 2021, as evidenced by the SYM-H index temporal variation. Upon impact, the IMF's Bz component rapidly turned southward, reaching -17 nT, which led to a moderate (G2) geomagnetic storm and auroral displayed across regions such as Sweden, Scotland, and New Zealand (https://www.washingtonpost.com/weather/2021/11/04/aurora-northern-lights-november2021-photos/). Figure 4.9 shows the variation of (a) z-component of the magnetic field, (b) y-component of the electric field (E_y), the solar wind speed, (d) the proton number density (n), (e) the proton temperature, (f) the solar wind energy input to the magnetosphere–ionosphere (ϵ parameter) and (g) the geomagnetic SYM-H index (proxy for ring current intensity) from 18:00 UT 3 November to 15:00 UT 4 November 2021. About 30 minutes later, the solar wind's kinetic energy ($V_{SW} \geq 700$ km/s) was converted into electromagnetic energy, triggering the onset of the geomagnetic storm. This solar wind speed persisted around $\sim$ 700 km/s throughout the storm. As the energy input to the magnetosphere – ionosphere system increased, the SYM-H index began to drop 34 minutes post-impact, reaching its minimum value (-118 nT) on 4 November 2021 at 12:44 UT. During the recovery phase, all IP parameters gradually returned to their pre-storm levels. Although the storm took nearly 16 hours to develop, it was classified as a G4-level event, marking the third such occurrence in SC 25. It should be noted, however, that due to data gaps, the current analysis could not accurately quantify the auroral zone magnetic disturbances caused by intensified ionospheric currents within and around the auroral regions. Consequently, the associated Joule heating and particle precipitation effects could not be used to estimate ionospheric energy dissipation.

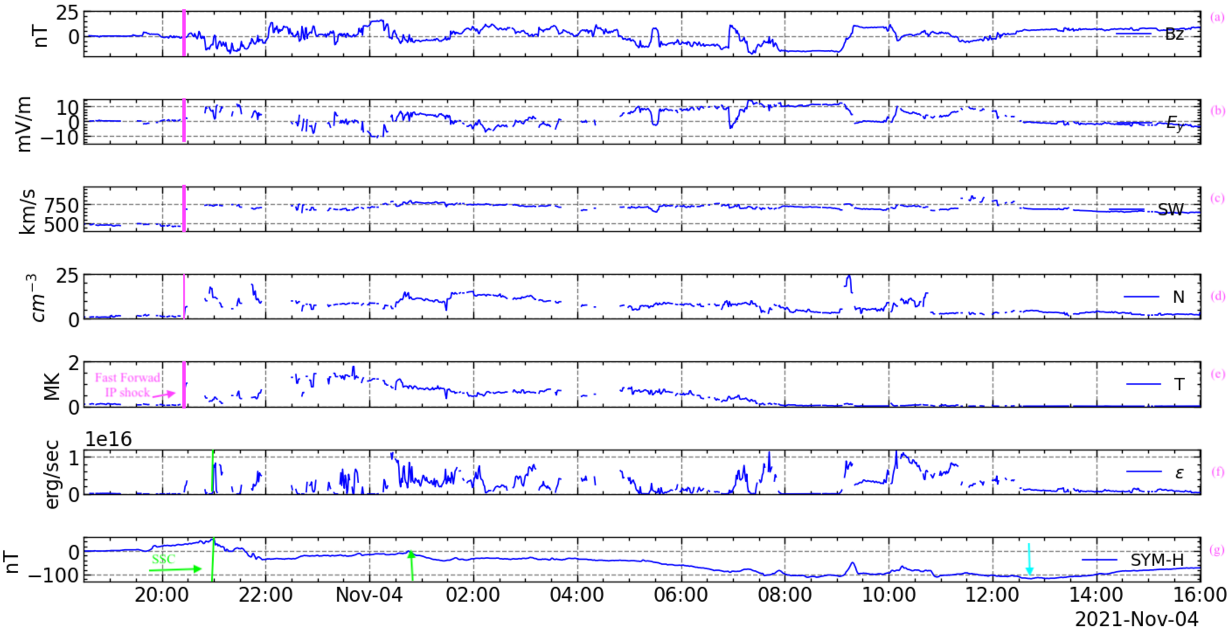

Figure 4.9: The solar wind parameters and geomagnetic activity during 3 – 4 November 2021. (a) the z-component of the interplanetary magnetic field (IMF), (b) y-component of the electric field (E_y), (c) the solar wind speed, (d) the proton number density, (e) the proton temperature, and (f) the SYM-H index: the geomagnetic field fluctuation, all from 1 minute resolution OMNIWEB. The arrival of the fast forward IP shock is indicated by the solid magenta vertical lines (a – e), while the start of the storm is indicated by the solid green vertical line (f-g). The cyan arrow indicates the time of the lowest SYM-H index (-118 nT at 12:45 UT).

Nonetheless, this geomagnetic storm was linked to substantial ionospheric perturbations in the Northern Hemisphere [348].

4.3.5 The 24 – 27 February 2023 events

February 2023 also experienced strong (G3) of $K_p = 7$ geomagnetic storm intensified by two halo CMEs. On 24 February 2023 between 13:15 – 13:19 UT, a group of type III SRBs were recorded by Glasgow CALLISTO spectrometer hosted by the University of Glasgow (https://www.astro.gla.ac.uk/) in the frequency range 50 – 80 MHz as shown in Figure 4.10. This radio emission originated from electrons accelerated during the GOES C2.9 SF eruption in the solar corona with onset at 12:58 UT, peaking and stopped at 13:09 UT and 13:22 UT, respectively. The solar eruption was linked to a halo CME observed within the SOHO LASCO C2 FOV at 13:26 UT, traveling at a speed of 922 km/s. Later that day, between 20:20 and 20:40 UT, a type II radio burst at 20:21 UT followed by a moving type IV radio burst with a frequency drift rate of approximately 0.08 MHz/s was recorded by the Cohoe Radio Observatory in Cohoe, Alaska, USA ($60.370°N$, $151.320°W$), among other CALLISTO spectrometers. These radio signals are presented in Figure 4.11. The emissions originated from active region AR13229, following the eruption of a GOES X-ray M3.7-class flare that began at 20:30 UT and ended at 20:53 UT. The flare was prominently captured by SDO particularly through its 94 $\AA$ channel. As a result of this flare eruption, ionization occurred in the Earth's upper atmosphere, leading to shortwave radio blackouts across the Pacific Ocean and other global regions. The presence of CME-driven shock waves was confirmed by the detection of type II and type IV radio bursts [349], which are typically indicative of intense CMEs and accompanying solar radiation storms. The 15-minute running difference images of the two

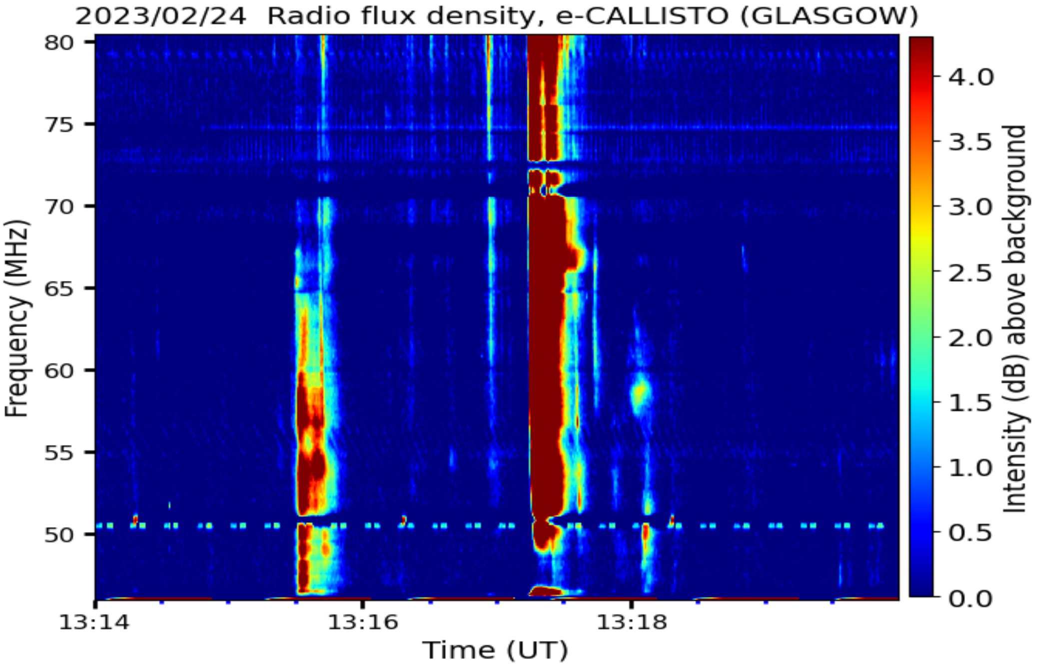

Figure 4.10: A group of type III radio bursts observed by GLASGOW CALLISTO spectrometer at University of Glasgow in the frequency range 50 – 80 MHz on 24 February 2023 between 13:15 – 13:19 UT.

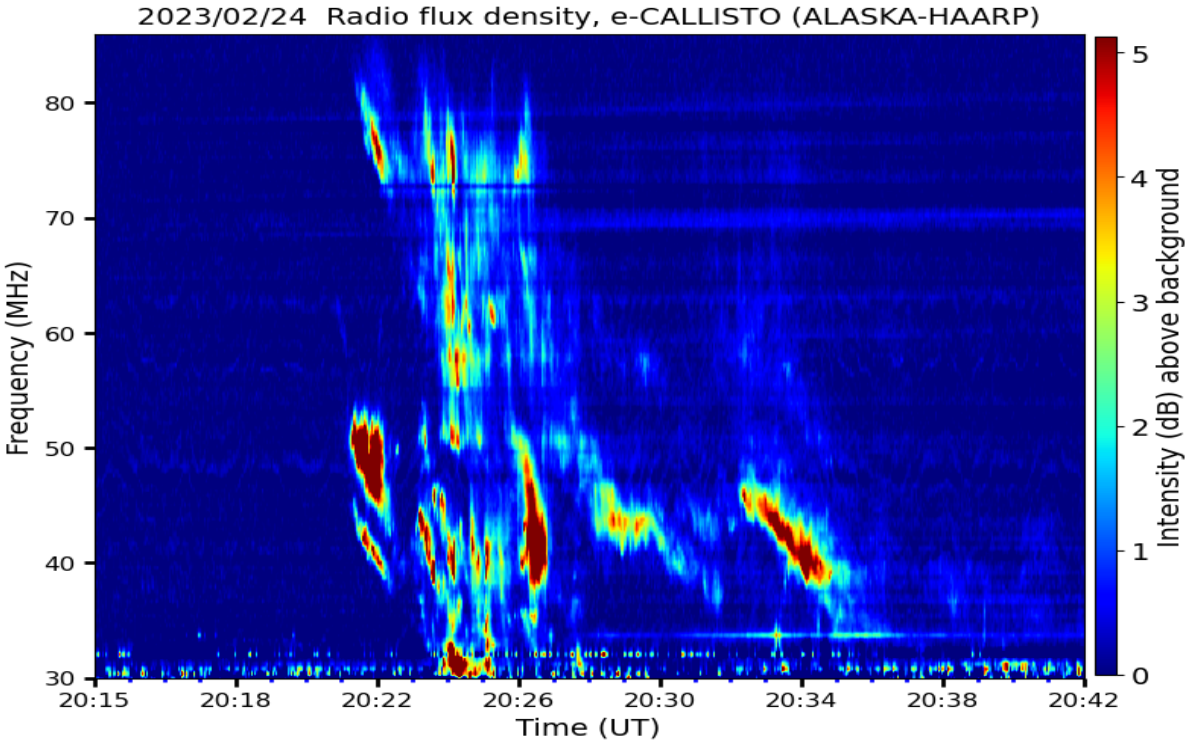

Figure 4.11: Type II radio burst from 20:22 UT to 20:30 UT followed by type IV radio burst from 20:24 UT to 20:35 UT.

CMEs launched on 24 February 2023 are shown in Figure 4.12. The fast forward IP shock of the first CME arrived near Earth's magnetosphere on 26 February 2023 at 19:27 UT while the second reached around 0:35 UT on 27 February 2023. The associated geomagnetic storm was classified as G3 or $K_p = 7$ and it was developed between 19:27 UT on 26 February 2023 and 12:15 UT on 27 February 2023 where a minimum SYM-H index of -161 nT value was attained. Hence, the ascending phase of SC 25 was characterized by high magnetic activity, and solar radio emissions

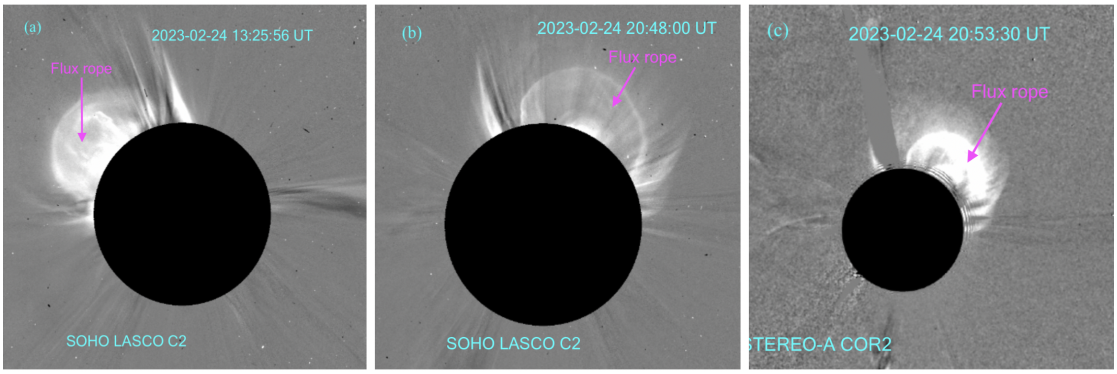

Figure 4.12: (a) SOHO/LASCO-C2 coronagraph showing a 15-minute difference image of the CME captured on 24 February 2023 at 13:25:56 UT. The black circles represent the coronagraphs' occulting discs. This CME was not observed by STEREO-A. (b) SOHO/LASCO-C2 image of the CME that erupted on 24 February 2023 at 20:36 UT, and (c) the corresponding observation of the same CME by STEREO-A/COR2 at 20:53:30 UT. In each panel, the magenta arrows highlight the outward expansion of the flux rope.

could serve as tracers.

4.4 Occurrence of large SEPs and their association with solar radio emissions

4.4.1 Results

The occurrence of large SEP events, shown as red stars, closely followed the changes in monthly sunspot numbers as the solar cycles advanced, as illustrated in Figure 4.13. The pattern in sunspot activity and the timing of large SEP events shown in Figure 4.13 suggest a strong correlation throughout the solar cycles. Out of 122 large SEP events identified in the study, about 88% were linked to both SFs and CMEs. Only six events were not associated with GOES X-ray flares (see Table 4.4). The relationship between GOES X-ray flares and large SEP events is shown in Figure 4.14 for solar cycles 23, 24, and 25. Figures 4.14(a), 4.14(c), and 4.14(e) display the locations on the Sun where these flares and SEP events originated, mostly from the western hemisphere (98 out of 116 events) [326]. Figures 4.14(b), 4.14(d), and 4.14(f) show the flare classes linked to SEP events, with M- and X-class flares being the most common. No ground-level enhancements (GLEs) were observed during the rising phase of SC 24; the first appeared on 17 May 2012. In contrast, SC 25 had its first GLE on 28 October 2021 and a second on 11 May 2024. SC 23 recorded four GLEs during its rising phase [66]. Results from VDA for 106 large SEP events are provided in Table 4.4. VDA couldn't be applied to 16 events due to missing flux data, likely caused by sensor saturation. VDA was conducted using flux measurements from the HED sensor on SOHO/ERNE across 9 energy bands (14.5–90.5 MeV) as listed in Table 4 of Vainio et al. [306]. Table 4.4 includes the following: column 1 shows event dates; columns 2–6 contain the start and

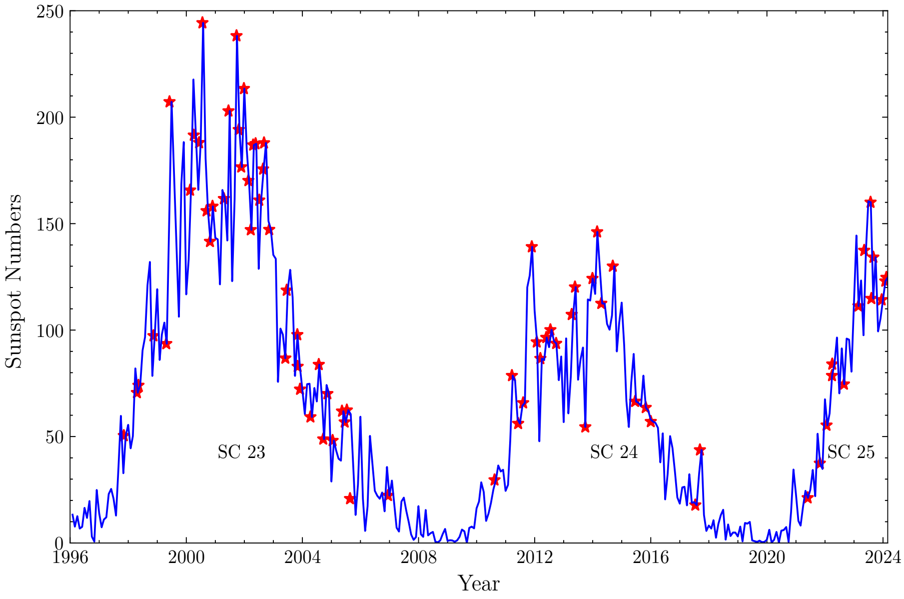

Figure 4.13: Comparison of the solar activity across three solar cycles based on monthly sunspot numbers and large SEP events, indicated by red stars. Large SEP events tend to follow the progression of the sunspot cycle, similar to halo CMEs [350, 66]. If multiple SEP events occurred in the same month, the red star marks the latest one.

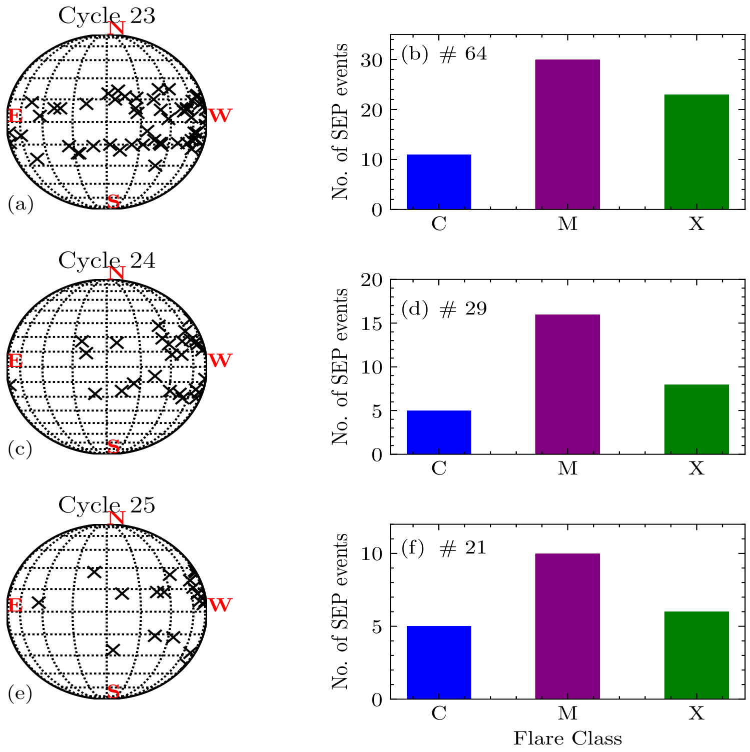

Figure 4.14: (a) Solar source locations of SFs and associated large SEP events, and (b) the distribution of flare classes related to large SEP events in cycle 23. (c) and (d) show the same for cycle 24, and (e) and (f) for cycle 25. Most large SEP events are tied to strong flares (M and X classes) and originate from the western hemisphere (±40° longitude).

peak times of the associated GOES flares, flare class, and source location. Seven SEP events are not linked to visible flares because their sources were behind the limb [351]. Radio bursts and their start times are listed in columns 7–8. Columns 9–10 report SEP onset times and peak flux values, while columns 11–12 present VDA results, including estimated release times (t_0) and path lengths (L) with uncertainties. Figure 4.15 provides an example of the VDA analysis for the 28 July 2023 event. This particular event was released 37 minutes after the peak of the associated M4-class flare and 35 minutes after the CME appeared in the LASCO C2 coronagraph. The estimated path was 1.75 AU. The event likely resulted from a CME-driven shock, as it occurred during the decay phase of the flare [352]. CME onset times and speeds are shown in columns 13 and 14 of Table 4.4. Most SEP events are linked to full or partial halo CMEs with angular widths over 160°. Events highlighted with gray shading in the table come from Kouloumvakos et al. [304], bolded rows appear in both Kouloumvakos et al. [304] and Ameri et al. [305], and cyan-shaded rows are from Ameri et al. [305].

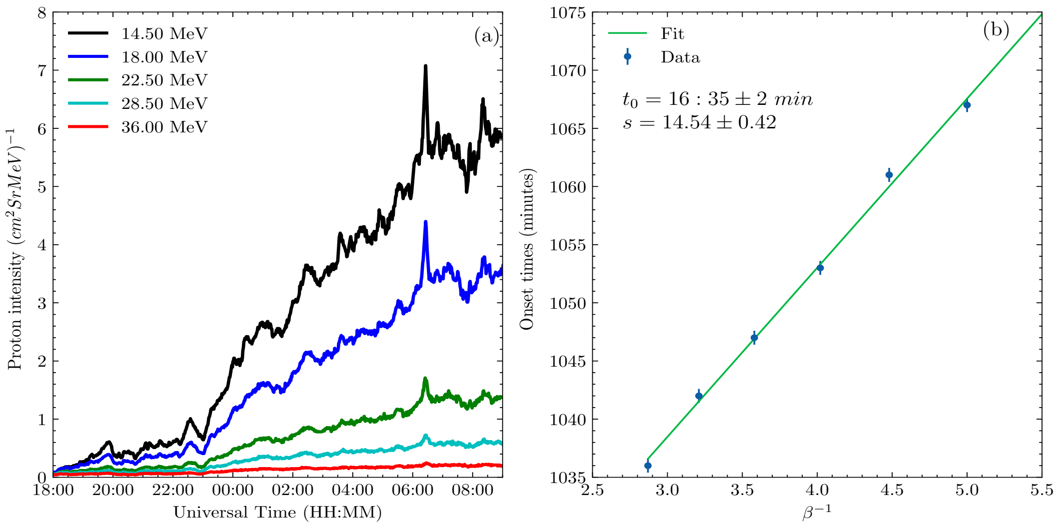

Figure 4.15: VDA method applied on the 28 July 2023 SEP event using SOHO/ERNE data. (a) Proton flux profile for the 28 July 2023 SEP event in the 14.5–36.0 MeV energy range. (b) VDA plot showing onset times as a function of inverse velocity (β^{-1}), where the slope gives the path length (L) and the y-intercept gives the release time (t_0).

Table 4.4: List of large SEP events, proton VDA results and associated solar phenomena(SFs, solar radio emissions and CMEs). Large SEP events highlighted with gray color in background are from Kouloumvakos et al. [304], those in boldface are found in Kouloumvakos et al. [304] and Ameri et al. [305], respectively; and large SEP events within cyan color background are from Ameri et al. [305].

Soft X-ray Flare						Radio Burst		SEP Event		Proton VDA		CME	
Date dd/mm/yyyy (1)	Start (UT) (2)	Peak (UT) (3)	Class (4)	NOAA (5)	Location (6)	Type (7)	Start (UT) (8)	t_{onset} (UT) (9)	I_p (PFU) (10)	t_0 (UT) (11)	L (AU) (12)	Onset (UT) (13)	Speed (kms^{-1}) (14)
04/11/1997	05:52	05:58	X2.1	08100	S14W33	III/II/IV	05:56	06:41	67	$06:16 \pm 02$	1.48 ± 0.05	06:10	785
06/11/1997	11:49	11:55	X9.4	08100	S18W63	IV/II	11:51	12:37	490	$12:18 \pm 02$	1.19 ± 0.08	12:10	1300
20/04/1998	09:38	10:21	M1.4	08210	S20W100	III/II	10:03	11:13	161	$10:15 \pm 05$	2.67 ± 0.12	10:07	1863
02/05/1998	13:31	13:42	X1.1	08210	S15W15	III/II	13:34	14:10	149	$13:45 \pm 02$	1.34 ± 0.06	14:06	938
06/05/1998	07:58	08:09	X2.7	08210	S11W65	IV/II	08:01	08:29	239	08:13	1.06	08:29	1099
09/05/1998	03:04	03:40	M7.7	08210	S17W100	II/III	03:22	04:32	12	$03:34 \pm 06$	2.55 ± 0.12	03:35	2331
14/11/1998	05:15	05:08	C1.7	08385	N28W100	III/II	05:55	06:16	314	05:58	1.16	N/A	N/A
24/04/1999	N/A	N/A	N/A	08517	N22W130	N/A	N/A	14:30	31	$13:21 \pm 06$	2.14 ± 0.12	13:31	1495
01/06/1999	16:27	16:46	C1.3	08563	S25E50	III/II	18:44	19:22	48	$18:56 \pm 06$	2.71 ± 0.15	19:37	1772
04/06/1999	06:52	07:03	M3.9	08552	N17W69	II	07:02	08:30	64	N/A	N/A	07:26	2230
18/02/2000	**09:21**	**09:27**	**C1.1**	**08867**	**S16W87**	**II/III**	**09:19**	**09:37**	**13**	$\mathbf{09:32 \pm 05}$	$\mathbf{1.47 \pm 0.14}$	**09:54**	**890**
04/04/2000	**15:12**	**15:41**	**C9.7**	**08933**	**N18W72**	**IV/II**	**15:15**	**17:00**	**55**	$\mathbf{15:28 \pm 03}$	$\mathbf{1.51 \pm 0.07}$	**16:32**	**1188**
10/06/2000	16:40	17:02	M5.2	09026	N22W42	III/II	16:55	18:05	46	$17:10 \pm 02$	1.09 ± 0.05	17:08	1108
14/07/2000	10:03	10:24	X5.7	09077	N17W11	II/IV	10:20	11:45	24,000	$10:58 \pm 03$	1.56 ± 0.08	10:54	1674
22/07/2000	**11:17**	**11:34**	**M3.7**	**09085**	**N14W62**	**II/IV**	**11:25**	**12:25**	**17**	$\mathbf{11:26 \pm 04}$	$\mathbf{1.84 \pm 0.09}$	**11:54**	**1230**
11/08/2000	N/A	N/A	N/A	09124	S13E50	N/A	N/A	14:30	17	$13:32 \pm 03$	2.46 ± 0.08	N/A	N/A
12/09/2000	1:31	12:13	M1.0	09163	S19W08	II/III	11:43	13:50	321	$12:45 \pm 03$	1.25 ± 0.06	11:54	1550
16/10/2000	06:40	09:11	M2.5	09182	N02W90	IV/III/II	06:47	08:10	15	$07:02 \pm 05$	1.63 ± 0.10	07:27	1336
25/10/2000	08:45	11:25	C4.0	09182	N02W90	N/A	N/A	15:40	15	$14:51 \pm 03$	2.23 ± 0.08	08:26	770
24/11/2000	14:51	15:13	X2.3	09236	N21W07	II	15:12	16:00	93	N/A	N/A	15:30	1245
25/11/2000	00:59	01:31	M8.2	09240	N09E32	II/IV	01:07	23:40	591	N/A	N/A	01:31	2519
26/11/2000	16:34	16:48	X4.0	09236	N22W34	III/II	16:34	18:45	942	N/A	N/A	17:06	980
18/04/2001	02:11	03:14	C2.2	09415	S20W90	III/II	02:14	03:15	32	$02:16 \pm 06$	1.97 ± 0.19	02:30	2465
15/06/2001	**N/A**	**N/A**	**N/A**	**N/A**	**N00W115**	**II**	**15:33**	**16:25**	**26**	$\mathbf{15:40 \pm 05}$	$\mathbf{1.74 \pm 0.14}$	**15:56**	**1701**
24/09/2001	09:32	10:38	X2.6	09632	S16E23	IV/III	09:59	11:40	12,900	$10:17 \pm 07$	2.63 ± 0.16	10:30	2402
01/10/2001	04:41	05:15	M9.1	09628	S18W90	III	05:22	12:45	2,360	$12:24 \pm 03$	1.16 ± 0.08	0530	1405

Continued on next page

Table 4.4 – *Continued from previous page*

Soft X-ray flare						Radio burst		event		Proton VDA		CME	
Date dd/mm/yyyy (1)	Start (UT) (2)	Peak (UT) (3)	Class (4)	NOAA (5)	Location (6)	Type (7)	Start (UT) (8)	t_{onset} (UT) (9)	I_p (PFU) (10)	t_o (UT) (11)	L (AU) (12)	Onset (UT) (13)	Speed (kms^{-1}) (14)
19/10/2001	00:47	01:05	X1.6	09661	N16W18	II/IV	01:01	02:15	11	01 : 20 ± 09	2.35 ± 0.32	01:27	558
19/10/2001	16:13	16:30	X1.6	09661	N15W29	II/IV	16:24	18:00	14	16 : 31 ± 08	2.55 ± 0.32	16:50	901
22/10/2001	14:27	15:08	M6.7	09672	S21E18	III/II	14:46	16:45	24	15 : 14 ± 05	1.88 ± 0.09	15:06	1336
04/11/2001	16:03	16:20	X1.0	09684	N06W18	II/IV	16:10	17:05	31,700	16 : 36 ± 03	2.05 ± 0.08	16:35	1329
22/11/2001	22:32	23:30	M9.9	09704	S15W34	IV/II	22:35	23:20	18,900	22 : 52 ± 03	2.94 ± 0.08	23:30	1437
26/12/2001	04:32	05:40	M7	09742	N08W54	III/II	05:13	06:05	779	05 : 27 ± 03	1.37 ± 0.07	05:30	1446
20/02/2002	05:52	06:12	M5.1	09825	N12W72	III/II/IV	05:55	06:45	13	06 : 03 ± 03	1.08 ± 0.08	06:30	952
17/03/2002	04:52	04:58	C3.1	09871	S21E17	N/A	N/A	06:45	13	04 : 51 ± 03	2.12 ± 0.08	N/A	N/A
18/03/2002	02:16	02:31	M1.0	09870	S15W22	IV	02:15	13:00	53	11 : 48 ± 03	1.06 ± 0.08	02:54	989
22/03/2002	10:12	11:13	M1.6	09866	S09W90	II/III	10:47	13:15	16	11 : 47 ± 03	1.95 ± 0.08	11:06	1750
17/04/2002	07:46	08:24	M2.6	09906	S14W34	II/III/IV	08:08	11:35	24	09 : 27 ± 06	1.84 ± 0.12	08:26	1240
21/04/2002	00:43	01:51	X1.5	09906	S14W84	III/II	01:17	02:25	2,520	01 : 15 ± 06	1.24 ± 0.11	01:27	2393
22/05/2002	03:18	03:49	C5.0	09954	S30W34	III	03:48	06:55	820	06 : 05 ± 03	2.89 ± 0.08	03:50	1557
07/07/2002	11:15	11:43	M1.0	10017	S19W100	III	11:17	12:45	22	11 : 30 ± 06	1.87 ± 0.10	11:30	1423
15/07/2002	19:59	20:08	X3.0	10030	N19W01	III/IV	20:02	16/07 17:50	234	13 : 14 ± 03	1.11 ± 0.08	20:30	1151
14/08/2002	01:47	02:12	M2.3	10061	N09W54	III/II	01:57	02:50	26	01 : 57 ± 04	1.36 ± 0.08	02:30	1309
22/08/2002	01:47	01:57	M5.4	10069	S07W62	III/II	01:51	02:40	36	01 : 46 ± 06	2.03 ± 0.16	02:06	998
24/08/2002	00:49	01:12	X3.1	10069	S02W81	III/II/IV	01:00	01:40	317	00 : 58 ± 06	2.02 ± 0.24	01:27	1913
05/09/2002	16:18	17:06	C5.2	10102	N09E28	II	16:35	06/09 06:40	20	05 : 18 ± 03	1.23 ± 0.08	16:54	1748
09/11/2002	13:08	13:23	M4.6	10180	S12W29	IV/II	13:07	15:25	404	13 : 13 ± 14	2.99 ± 0.32	13:31	1838
31/05/2003	02:13	02:24	M9.3	10365	S07W65	III/II/IV	02:20	03:00	27	02 : 17 ± 05	1.85 ± 0.13	02:30	1835
17/06/2003	22:27	22:55	M6.8	10386	S09E60	III/II/IV	22:44	18/06 09:15	19	08 : 04 ± 03	1.23 ± 0.08	23:18	1813
26/10/2003	17:21	18:15	X1.2	10484	N02W38	II	17:35	18:25	466	17 : 30 ± 03	1.33 ± 0.08	17:54	1537
28/10/2003	09:51	11:10	X17.2	10486	S16E08	IV/II	10:33	11:45	29,500	10 : 21 ± 07	2.21 ± 0.16	11:30	2459
29/10/2003	20:37	20:49	X10.0	10486	S15W02	II/IV/III	20:39	21:00	3,300	N/A	N/A	20:54	2029
02/11/2003	17:03	17:25	X8.3	10486	S14W56	II/IV	17:14	17:35	1,570	16 : 57 ± 03	2.61 ± 0.08	17:30	2598
02/12/2003	11:31	11:50	C9.7	10508	S17W95	N/A	N/A	12:35	88	12 : 18 ± 03	1.61 ± 0.08	10:50	1393
11/04/2004	03:54	04:19	C9.6	10588	S14W47	III	03:58	06:10	35	04 : 42 ± 02	1.28 ± 0.05	04:30	1645
25/07/2004	14:19	15:20	M1.1	10652	N08W33	IV/II	14:25	16:55	2,090	14 : 55 ± 09	2.60 ± 0.20	14:54	1333
12/09/2004	00:04	00:56	M4.8	10672	N04E42	IV	00:13	10:35	273	09 : 31 ± 03	1.18 ± 0.08	00:36	1328
19/09/2004	16:46	17:12	M1.9	10672	N03W58	III/II/IV	16:50	18:10	57	N/A	N/A	N/A	N/A
01/11/2004	N/A	N/A	N/A	N/A	S00W120	III	05:42	06:10	63	05 : 34 ± 04	2.00 ± 0.10	06:06	800
07/11/2004	15:42	16:06	X2.0	10696	N09W17	II/IV	15:59	18:25	495	17 : 27 ± 03	2.84 ± 0.08	16:54	1759
09/11/2004	16:59	17:19	M8.9	10696	N07W51	IV/III/II	17:06	20:20	82	18 : 22 ± 03	2.77 ± 0.08	17:26	1853
10/11/2004	01:59	02:13	X2.5	10696	N09W49	III/II/IV	02:08	03:15	424	02 : 38 ± 03	2.57 ± 0.08	02:26	3387
15/01/2005	22:25	23:02	X2.6	10720	N15W05	IV/II	22:30	16/01 01:05	5,040	00 : 35 ± 03	2.49 ± 0.08	23:06	2861
13/05/2005	16:13	16:57	M8.0	10759	N12E12	III/II/IV	16:41	19:15	3,140	18 : 35 ± 03	2.05 ± 0.08	17:12	1689
16/06/2005	20:01	20:22	M4.0	0775	N08W90	III	20:12	20:45	44	20 : 21 ± 03	1.28 ± 0.07	N/A	N/A
13/07/2005	14:01	14:49	M5.0	10786	N11W90	III	14:06	17:55	134	14 : 15 ± 08	2.77 ± 0.18	14:30	1423
22/08/2005	16:46	17:27	M5.6	10798	S12W60	IV	16:54	19:20	330	N/A	N/A	17:30	2378
05/12/2006	10:18	10:35	X9.0	10930	S07E79	III/II/IV	10:27	N/A	1,980	N/A	N/A	N/A	N/A
13/12/2006	02:14	02:40	X3.4	10930	S06W24	III/II/IV	02:24	03:10	698	02 : 21 ± 11	2.13 ± 0.41	02:54	1774
14/08/2010	09:38	10:05	C4.4	1099	N17W52	II	09:52	11:05	14	10 : 19 ± 03	1.12 ± 0.08	10:12	1205
07/03/2011	19:43	20:12	M3.7	11164	N24W59	III/II	19:52	21:45	50	20 : 33 ± 07	1.81 ± 0.18	20:00	2125
21/03/2011	N/A	N/A	N/A	11169	Farside	III	02:21	03:55	14	02 : 47 ± 05	1.90 ± 0.16	02.24	1341
07/06/2011	06:16	06:41	M2.5	11226	S21W54	II/IV	06:25	08:20	73	07 : 22 ± 02	2.81 ± 0.05	06:49	1255
04/08/2011	03:41	03:57	M9.3	11261	N19W36	III/II/IV	03:50	04:30	96	04 : 12 ± 04	1.91 ± 0.12	04:12	1315
09/08/2011	07:48	08:05	X6.9	11263	N17W69	II/IV/III	08:01	08:20	26	08 : 07 ± 07	0.96 ± 0.11	08:12	1610
26/11/2011	06:09	07:10	C1.2	11353	N08W49	III	07:03	08:55	80	08 : 39 ± 03	2.35 ± 0.08	07:12	933
23/01/2012	03:38	03:59	M8.7	11402	N28W36	IV	03:39	04:45	6,310	N/A	N/A	04:00	2175
27/01/2012	17:37	18:37	X1.7	11402	N33W85	N/A	N/A	18:55	796	18 : 10 ± 02	2.34 ± 0.04	18:27	2508
07/03/2012	00:02	00:24	X5.4	11429	N17E15	II/IV	00:17	07:10	6,530	06 : 02 ± 02	1.29 ± 0.06	00:24	2684
13/03/2012	17:12	17:41	M7.9	11429	N18W62	II/III/IV	17:15	18:05	469	17 : 28 ± 05	1.49 ± 0.16	17:36	1884
17/05/2012	01:25	01:47	M5.1	11476	N11W76	III/II/IV	01:33	02:50	255	02 : 14 ± 02	2.92 ± 0.05	01:48	1582
26/05/2012	N/A	N/A	N/A	11428	Farside	II	20:17	23:35	14	22 : 37 ± 03	1.95 ± 0.08	20:57	1966

Continued on next page

Table 4.4 – *Continued from previous page*

Soft X-ray flare						Radio burst		event		Proton VDA		CME	
Date dd/mm/yyyy (1)	Start (UT) (2)	Peak (UT) (3)	Class (4)	NOAA (5)	Location (6)	Type (7)	Start (UT) (8)	t_{onset} (UT) (9)	I_p (PFU) (10)	t_o (UT) (11)	L (AU) (12)	Onset (UT) (13)	Speed (kms^{-1}) (14)
06/07/2012	23:01	23:08	X1.1	11515	S18W50	III/II	23:04	07/07 00:05	25	N/A	N/A	23:24	1828
08/07/2012	16:23	16:32	M6.9	11515	S17W74	III/II	16:23	18:10	19	N/A	N/A	16:24	2711
12/07/2012	15:37	16:49	X1.4	11520	S16W09	IV/II	16:15	17:25	96	16 : 59 ± 02	1.22 ± 0.06	16:48	885
17/07/2012	12:03	17:15	M1.7	11520	S17W75	N/A	N/A	16:15	136	15 : 25 ± 02	1.85 ± 0.05	13:48	958
27/09/2012	23:36	23:57	C3.7	11577	N08W41	II	23:44	28/09 01:20	28	N/A	N/A	00:12	947
11/04/2013	06:55	07:16	M6.5	11719	N09E12	III/II	07:03	08:55	114	08 : 39 ± 02	2.75 ± 0.05	07:24	861
22/05/2013	13:08	13:32	M5.0	11745	N15W70	II/IV	12:59	14:20	1,660	12 : 52 ± 01	2.74 ± 0.04	13:25	1466
29/09/2013	21:43	23:37	C1.2	N/A	N15W40	II	21:53	30/09 00:25	182	N/A	N/A	22:12	1179
28/12/2013	17:53	18:02	C9.3	11936	S18E07	N/A	N/A	19:00	29	18 : 43 ± 02	2.84 ± 0.06	17:36	1118
20/02/2014	07:26	07:56	M3.0	11976	S15W67	II	07:45	08:15	22	07 : 51 ± 03	1.17 ± 0.08	08:00	948
25/02/2014	00:39	00:49	X4.9	11990	S12E82	III/II/IV	00:45	07:55	103	07 : 08 ± 03	2.10 ± 0.08	01:25	2147
18/04/2014	12:31	13:03	M7.3	12036	S16W41	IV/II	12:42	13:40	58	13 : 24 ± 02	2.32 ± 0.06	13:25	1203
10/09/2014	17:21	17:45	X1.6	12158	N16W06	IV	21:00	23:35	126	22 : 09 ± 02	2.53 ± 0.06	18:00	1267
18/06/2015	00:33	01:27	M1.2	12365	SW limb	III	00:55	04:52	17	04 : 27 ± 03	2.46 ± 0.08	01:25	1714
29/10/2015	N/A	N/A	N/A	12434	Farside	II	02:19	03:05	23	02 : 30 ± 02	2.30 ± 0.06	02:36	530
01/01/2016	23:10	00:11	M2.4	12473	S21W73	II/III	23:21	02/01 00:05	21	23 : 26 ± 02	1.60 ± 0.06	23:24	1730
14/07/2017	01:07	02:09	M2.4	12665	S06W29	II/IV	01:23	03:12	22	02 : 41 ± 03	1.70 ± 0.08	01:25	1200
04/09/2017	20:28	20:33	M5.5	12673	S11W16	II	20:36	22:15	844	21 : 45 ± 03	1.56 ± 0.08	20:36	1418
10/09/2017	15:35	16:06	X8.2	12673	S08W83	II/III/IV	15:53	16:25	1494	N/A	N/A	16:00	3163
28/05/2021	22:19	23:13	C9.4	12824	N21W63	II	23:03	23:44	15	23 : 12 ± 02	1.35 ± 0.05	23:12	971
28/10/2021	15:17	15:35	X1.0	12887	S26W04	III/II/IV	15:28	16:48	29	16 : 13 ± 01	1.50 ± 0.04	15:48	1519
20/01/2022	05:41	06:01	M5.5	12929	N07W83	II	06:01	06:47	12	06 : 19 ± 01	1.36 ± 0.04	06:12	1431
28/03/2022	10:58	11:29	M4.0	12975	N12W09	II/IV	11:23	12:15	19	11 : 50 ± 01	1.07 ± 0.04	12:00	702
30/03/2022	17:21	17:37	X1.3	12975	N13W31.	II	17:30	22:02	11	21 : 28 ± 02	1.29 ± 0.06	18:00	641
02/04/2022	12:56	13:55	M3.9	12975	N12W68	II /IV	13:24	13:54	32	13 : 26 ± 01	1.30 ± 0.04	13:36	1433
27/08/2022	09:11	09:16	C4.4	13088	S28W71	N/A	N/A	09:54	27	09 : 26 ± 02	1.03 ± 0.06	09:48	509
25/02/2023	18:40	19:44	M6.4	13229	N25W44	II /IV	19:23	20:27	58	19 : 49 ± 01	1.91 ± 0.04	19:24	1170
09/05/2023	20:32	20:52	M5.0	13296	N13W36	N/A	N/A	21:53	83	20 : 59 ± 02	1.74 ± 0.05	19:00	1209
16/07/2023	N/A	N/A	N/A	N/A	Farside	II	04:34	05:28	18	04 : 39 ± 02	1.55 ± 0.06	04:42	1970
17/07/2023	22:41	22:54	M2.7	13363	N25W81	III	23:19	18/07 00:52	620	00 : 06 ± 02	1.91 ± 0.42	23:36	1385
28/07/2023	15:39	15:58	M4.1	13376	N27W87	III/ II	15:42	17:23	154	16 : 35 ± 02	1.75 ± 0.05	16:00	1896
05/08/2023	06:16	07:18	M1.6	13386	N07W69	IV	07:06	08:57	18	08 : 10 ± 02	2.03 ± 0.05	07:00	1000
07/08/2023	20:30	20:46	X1.5	13386	N12W88	II	20:38	21:13	47	20 : 46 ± 02	1.65 ± 0.06	20:48	1851
01/09/2023	03:06	03:51	M1.2	13413	N16W64	III	03:08	04:30	25	03 : 49 ± 02	1.49 ± 0.05	03:24	1339
15/12/2023	23:31	23:43	C5.4	13514	N05W76	N/A	N/A	23:45	13	N/A	N/A	N/A	N/A
03/01/2024	19:38	20:16	C2.7	13536	N06E43	N/A	N/A	20:05	20	N/A	N/A	N/A	N/A
29/01/2024	03:54	04:38	M6.8	13559	N28W86	III/II	04:19	05:15	137	04 : 34 ± 01	1.46 ± 0.04	04:24	812
09/02/2024	12:53	13:14	X3.3	13575	S37W85	III/IV	13:03	15:10	187	14 : 53 ± 02	1.25 ± 0.06	13:23	1890
12/02/2024	05:43	05:54	C6.9	13576	S16W30	III	06:27	08:05	118	07 : 45 ± 02	1.32 ± 0.05	06:36	1009
23/03/2024	00:58	01:33	X1.1	13614	N27E08	II	01:09	06:15	14	05 : 54 ± 03	1.70 ± 0.08	01:48	873
11/05/2024	01:10	01:23	X5.8	13664	S17W44	III/IV	01:13	02:10	116	N/A	N/A	01:36	752

Figure 4.16 presents the distribution of large SEP event occurrences as a function of the time lag between their estimated release times and the peak of the associated SFs across each solar cycle. Negative values correspond to immediate release with no delay, whereas a time difference of zero indicates that the release coincided exactly with the peak of the respective SF. Positive values represent delays in particle release. Such delays are often attributed to the time required for shock waves to effectively accelerate protons to relativistic energies [353, 354]. Among the 55 recorded large SEP events, 31 occurred concurrently with flare eruptions (i.e., no delay), as seen in Figure 4.16(a). During solar cycle 23, ten events exhibited delays of less than one hour. In cycle 24 (Figure 4.16(b)), nine events were released without delay, while six were delayed by less

than an hour. Likewise, Figure 4.16(c) indicates that seven large SEP events were released during the SF eruptions, while six others experienced delays of under one hour. Figure 4.17 highlights

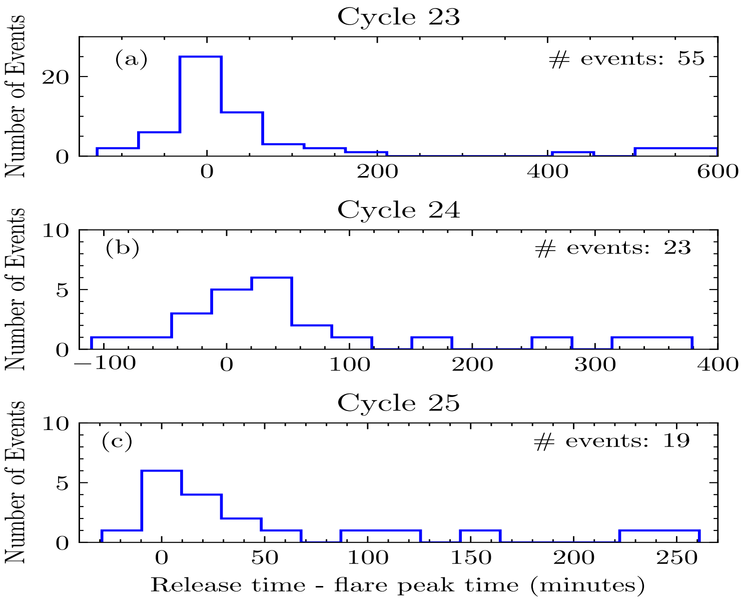

Figure 4.16: Temporal offsets between the onset of large SEP events and the peak emission of their associated SFs. Negative values indicate an almost immediate particle release following flare onset, whereas zero denotes precise synchronization with the SF peak time.

the comparison of time differences between large SEP event releases and the onset of associated solar radio emissions during the ascending phases of the three solar cycles. It is observed that approximately 55% (30 out of 54), 83% (19 out of 23), and 82% (14 out of 17) of large SEP events in cycles 23, 24, and 25, respectively, align with particle populations or emerging radio emission signatures. SEP events released more than 100 minutes after the onset of these emissions are generally believed to result from IP acceleration mechanisms or CIRs. Type III bursts are widely regarded as indicators of electron and charged particle emissions into the heliosphere. The classification of events often depends on their temporal relationship with type III burst onsets. In many large events, particle production particularly of electrons and protons continues well beyond the durations of type III bursts, often with substantial delay [355].

4.4.2 Comparative Analysis and VDA Technique

SC 25 has thus far exhibited greater solar activity compared to its predecessor, in agreement with earlier predictions [356, 61, 62]. This elevated activity suggests a higher frequency of geomagnetic storms approaching its expected maximum in 2025 [65]. The pattern of large SEP event occurrences during the ascending phase of SC 25 mirrors that observed in SC 23, as illustrated in Figure 4.13. Specifically, 22 large SEP events occurred before March 2001 (SC 23), 11 prior to May 2012 (SC 24), and 22 were registered before June 2024 (SC 25), as detailed in Table 4.4. Regarding GLEs (https://gle.oulu.fi/), four events were recorded during SC 23's rise, none during SC 24, and two so far in SC 25 (on 28 October 2021 and 11 May 2024), indicating comparatively higher SEP activity in SC 25 relative to SC 24. A substantial proportion (76%) of the large SEP events were linked to M- and X-class SFs, with most originating from

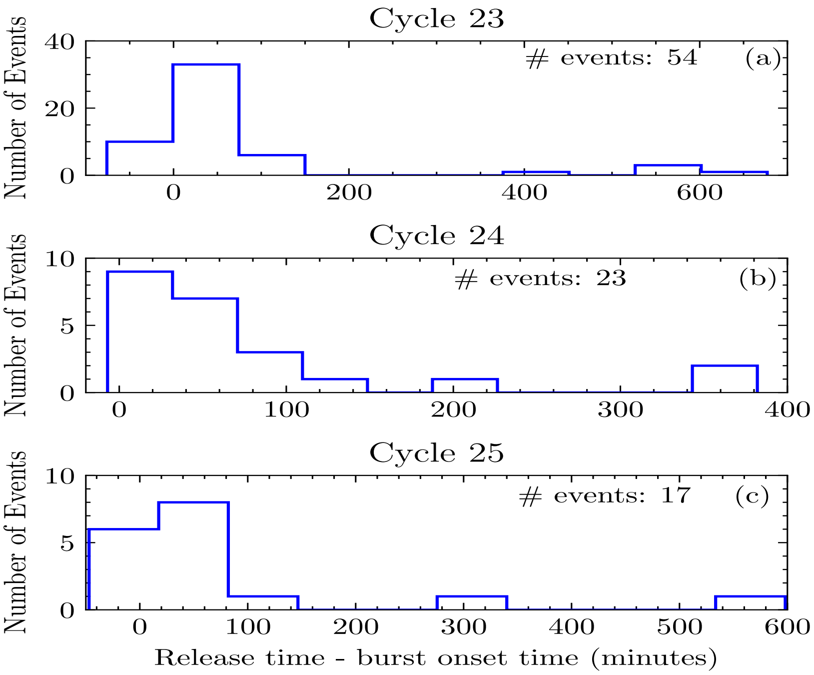

Figure 4.17: Temporal differences between the release times of large SEP events and the onset of their associated solar radio emissions. Negative values indicate that SEP release occurred before the initiation of the radio bursts.

the western solar hemisphere (Figure 4.14). Since flares and SEP events from the western side of the solar disk have a higher geoeffective potential, this regional distribution is particularly significant. Supporting this, Kouloumvakos et al. [304] found that IP magnetic flux structures typically follow the same spatial distribution as flare sources. Moreover, 91% of large SEP events were accompanied by fast halo CMEs with speeds exceeding 500 km/s (see Table 4.4). Such CMEs promote favorable conditions for efficient particle acceleration due to the formation of shock fronts [357, 352]. Nonetheless, they may also contribute to delayed acceleration processes within the corona, which could account for the late detection of energetic particles near 1 AU [355].

Solar radio emissions were observed in association with 90% of large SEP events, with 36 out of 96 recorded radio bursts occurring before the associated flare's peak. This supports the widely accepted view that both SFs and CMEs are responsible for large SEP events. However, Zhang et al. [358] noted that during solar minimum when flares and CMEs are rare,CIRs may act as the primary drivers of SEP events. This explains the 11 August 2000 SEP event, which lacked any clear association with a flare or CME, as shown in Table 4.4. To further investigate particle propagation, VDA method was employed to estimate the apparent path length (L) of particles traveling along IP magnetic field lines. The calculated path lengths ranged from 1.0 to 3.0 AU, with 70% of events showing $L > 1.5$ AU. These estimates are consistent with previous findings in the literature [e.g., 359, 360, 306, 304, 361, 305]. Despite this consistency, the VDA often yields path lengths significantly exceeding 1 AU for certain SEP events. According to Lintunen and Vainio [359], values of $L > 1.5$ AU may result from particle scattering in the IP medium, as well as non-zero pitch angles at the point of release [362]. Ultimately, accurate estimation of path length provides crucial insight into the timing and transport of SEPs from their solar source.

4.4.3 SEPs Inferred from Solar Radio Emissions

As illustrated in Table 4.4, solar radio type II bursts alone were linked with 15 major SEP events. When type II bursts were accompanied by type IV bursts, this number increased to 20 events. The presence of type II radio emissions confirms that a total of 35 large SEP events were driven by coronal and IP shocks [200]. The simultaneous detection of type II and persistent type IV radio emissions is characteristic of the early stages of CME evolution, following the occurrence of a gamma-ray burst, and serves as a valuable forecasting indicator [e.g., 363]. Furthermore, type III radio emissions preceded 59 large SEP events. Among these, 22 were also associated with type II bursts, and 21 showed a combination of type II and type IV bursts. Due to their frequent occurrence and role in identifying open magnetic field lines, type III bursts are often used as a baseline in SEP-related studies [324, 351, 306, 364, 304, 336, 111, 305]. Figure 4.18 provides an example of complex solar radio emissions tied to a large SEP event on 28 July 2023. Panel (a) displays a group of type III emissions followed by band-splitting type II bursts recorded by the CALLISTO station at the Deutsches Zentrum für Luft- und Raumfahrt (DLR), Germany. These fast and slow drift emissions signify magnetic reconnection between the expanding closed loops of a flux rope and adjacent open field lines [365]. The continuation of these emissions in IP space is captured in Figure 4.18(b) by WAVES/STEREO in the 16–0.25 MHz frequency range. These emissions originated from active region AR 13376, associated with an M4.1-class soft X-ray flare, as shown using HMI data overlaid on AIA 131 $\AA$ imagery in Figure 4.18(c). The 15-minute running difference image in panel (d) illustrates the outward-expanding CME-driven shock, further confirmed by SOHO/LASCO C2 observations. Type III bursts are frequently observed during solar activity, resulting from electron beams generating Langmuir waves, which subsequently convert into escaping radio emissions. Their absence also provides diagnostic information. For instance, confined flares, energetic events without associated CMEs often lack type III bursts, as seen in about 10% of X-class flares during SC 23 [366]. This study recorded two GLE events during SC 25 using neutron monitor data. The first, on 28 October 2021, has been the focus of various investigations [e.g., 365, 367, 368]. The second occurred on 11 May 2024, and its associated solar radio emissions and origin are depicted in Figure 4.19. Figure 4.19(a) presents a group of type III bursts from 01:13 UT to 01:26 UT 11 May 2024, followed by a type IV burst recorded by the ASSA. The IP extension of the type III bursts is shown in panel (b). The eruption's source region is identified in panel (c), where HMI data, overlaid on AIA 131 $\AA$ imagery, marks the active region responsible. Panel (d) shows the outward-expanding flux rope and shock structure via a 15-minute running difference image. The associated energetic halo CME (752 km/s) was Sun–Earth disconnected, resulting in no geomagnetic storm. Notably, SOHO/ERNE did not detect this GLE, suggesting the particle energies exceeded the FOV of the HED sensor. Consequently, observations from multiple spacecraft are necessary to fully characterize the 11 May 2024 GLE. At lower energies, SEPs predominantly reach Earth's polar regions, causing PCAs and affecting the ionosphere. These effects are mostly confined to high-latitude, high-altitude areas, disrupting

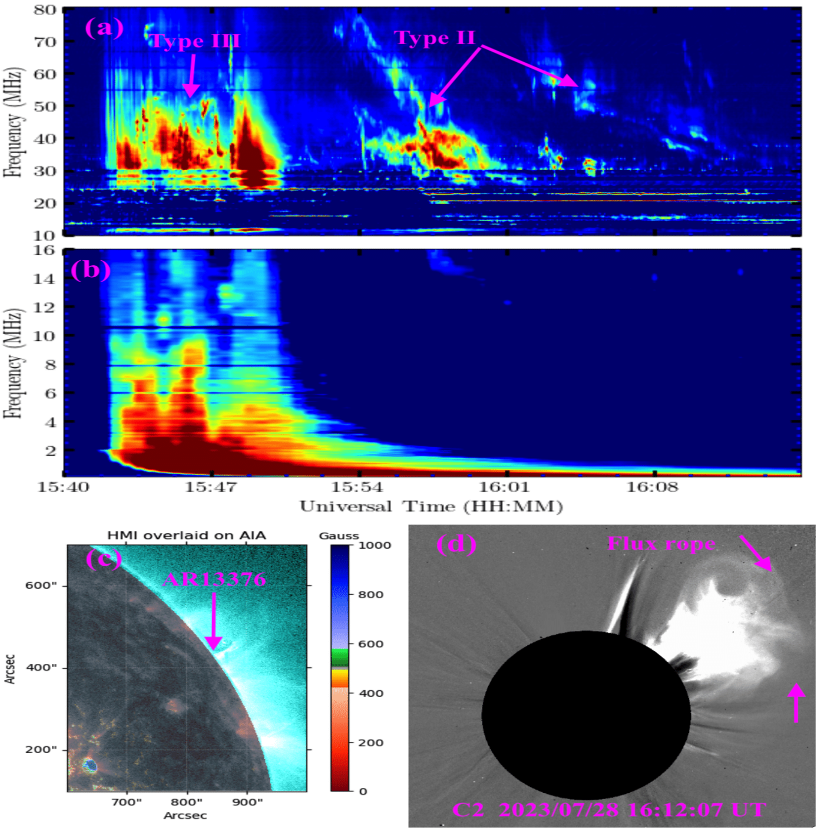

Figure 4.18: Dynamic spectrum showing (a) group of type III radio emission from 15:42 UT to 15:50 UT followed by band-splitting type II radio bursts from 15:52 UT to 16:14 UT 28 July 2023 observed by the Deutsches Zentrum f"ur Luft- und Raumfahrt in Germany (DLR) (b) IP continuation of type III radio bursts observed by WAVES/STEREO within 16 – 0.25 MHz (c) solar source location indicated by active region number using HMI overlaid on AIA of 131 $\AA$ wavelength and (d) 15 minutes running difference image illustrating the CME-driven shock.

HF communication and navigation systems. PCAs, caused by particles in the 10–100 MeV range, typically begin within an hour of solar acceleration [369]. Of the 122 large SEP events considered in this study, 93 (76%) were linked to solar radio bursts with IP counterparts. The most frequent IP radio signatures of flares and CMEs are type II bursts (tracing magnetohydrodynamic shock waves) and type III bursts (signaling electron streams along open or semi-open field lines) [370]. In 114 cases, 15-minute running difference images revealed flux ropes expanding radially, pointing to underlying magnetic instability. M-type III emissions are indicators of impulsive flare-associated events [321], whereas type IV bursts are more reliable predictors of SEP events reaching Earth. The type IV continuum represents prolonged electron acceleration within the corona, linked to CME-driven shocks [371]. As noted by Pick and Vilmer [372], large SEP events typically correlate with type II and type IV emissions in the metric-to-decametric range. Gopalswamy et al. [222] emphasized that although CMEs originating near the solar disk center (within ±15° longitude) may not always impact Earth directly, the shocks they generate can still propagate Earthward. This may explain instances where fast CMEs were observed without corresponding Earth-directed impacts. Additionally, two SEP events lacking visible radio bursts or CMEs began synchronously with peak flare times, suggesting that although they were energetic, they went undetected by HED/ERNE

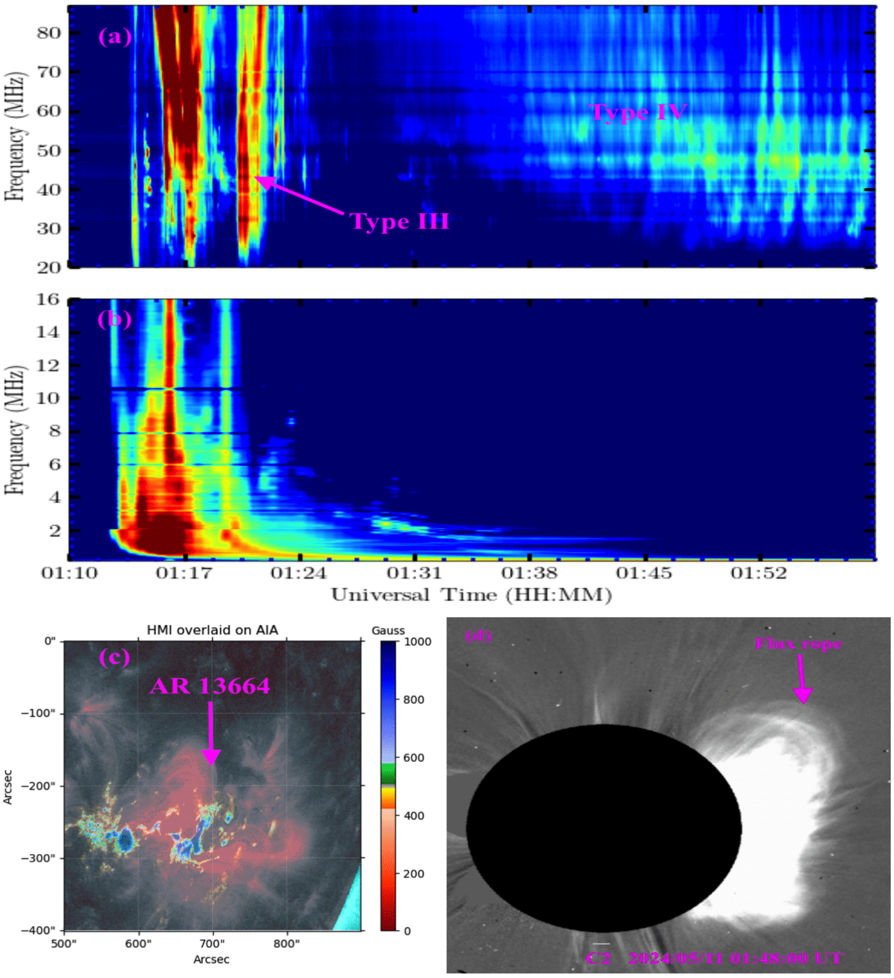

Figure 4.19: Dynamic spectrum showing (a) group of type III radio emission from 01:13 UT to 01:26 UT 11 May 2024 followed by type IV radio burst from 01:28 UT to 02:00 UT observed at Astronomical society of South Australia (b) IP continuation of type III radio bursts observed by WAVES/STEREO within 16 – 0.25 MHz (c) solar source location indicated by active region number with HMI overlaid on AIA of 131 $\mathring{A}$ wavelength and (d) 15 minutes running difference image illustrating the CME-driven shock.

due to sensor saturation.

4.5 Summary

This chapter presents the findings of a correlation analysis conducted to assess solar activity during the ascending phase of SC 25 using low-frequency solar radio observations. The study began with the analysis of 32 solar radio type II bursts with clear morphology, recorded by the e-CALLISTO network. Radio parameters obtained from the dynamic spectra were used to determine shock characteristics and estimate the ambient magnetic field strength. A strong correlation was found between the drift rates and starting frequencies: key parameters in determining shock properties. The derived shock speeds ranged from 504 to 1282 kms^{-1} and the Alfvén speeds ranged from 368 to 826 kms^{-1} at $\sim 1-2\ R_{\odot}$. The Mach numbers were found to be between 1.1 and 1.8, while the magnetic field strength ranged from 8 to 0.5 G and followed the model $B(r) = 6.07r^{-3.96}\ G$ at $\sim 1-2\ R_{\odot}$. The chapter also explores the correlation between solar radio emissions and geomagnetic storms. It was found that type II, III, and IV solar radio bursts preceded 23 out of 35 geomagnetic storms during the study period, with an average delay of 79 hours (ranging from 48 to 120 hours) between the onset of radio bursts and the arrival of CMEs and/or HSS at Earth's magnetosphere. Five of the 35 geomagnetic storms were recurrent and associated with HSS, while the rest were triggered by CMEs with average speeds $\sim 700\ kms^{-1}$. Four major geomagnetic storms: on 4 November 2021, 27 February 2023, 24 March 2023, and 24 April 2024 were analyzed in detail. The CMEs linked to these intense events featured radially expanding flux ropes, and the dynamics of their cores were consistent with the signatures of type II and moving type IV radio bursts. The last part of the analysis showed that the occurrence of large SEP events aligned with the sunspot cycle progression. A comparative analysis across the three most recent solar cycles revealed that SC 25 exhibited more intense solar activity than SC 24. Among the 122 large SEP events recorded, 35 occurred concurrently with the peak of associated SFs and the onset of SRBs, while the remaining events showed a temporal delay. Estimated path lengths of large SEP events ranged from 1.0 to 3.0 AU, with longer paths ($L > 1.5\ AU$) attributed to pitch-angle scattering and the geometry of the acceleration region. The main solar drivers of these large SEP events were identified as shock waves generated by SFs, CMEs, and rapid plasma flows in magnetic reconnection regions, accounting for 115 out of the 122 events analyzed. Furthermore, solar radio emissions were observed to precede 90% of SEP events, and data from WAVES/STEREO indicated that about 76% of these SRBs extended into IP medium, reflecting the propagation of shocks and electron beams through open or quasi-open magnetic field lines. The characteristics of SEP populations linked to SFs and CMEs were effectively diagnosed using SRBs, primarily classified as type II, III, and IV bursts. Overall, the rising phase of SC 25 exhibited elevated solar activity, with increased occurrences of geomagnetic storms and large SEP events, and SRBs proving to be reliable observational proxies.

Chapter 5

Space Weather Implications

Comprehensive insight into solar eruptions from Sun to Earth requires integrating multi-wavelength data from both ground- and space-based instruments. This chapter explores the space weather implications owned by solar radio emissions. Radio emissions are especially valuable as they serve as early indicators of eruptive solar events, particularly intense flares and CMEs, which often represent the most significant hazards [373].

5.1 Introduction

The primary cause of the most intense space weather events in the magnetosphere is the interaction between CMEs, their associated shocks, and the Earth's magnetosphere. These shocks can be observed across extreme ultraviolet, visible, and radio wavelengths [374, 375]. CMEs trigger space weather hazards by compressing the Earth's magnetosphere upon their arrival at the Earth which results in channeling the particles into the Earth's atmosphere to produce auroras. CMEs are also responsible for geomagnetic storms, power grid disruptions, accelerating SEP events etc.

SEP events are regarded as one of the most critical components of space weather [e.g., 320, 330, 376, 377, 378, 379]. These events typically follow the broader pattern of SC activity marked by eruptive phenomena [111]. From an Earth-based perspective, SEPs present several risks, including disruptions to HF radio communication in polar regions, inaccuracies in navigation systems, elevated radiation exposure for astronauts and for airline passengers and crew at high altitudes and latitudes, as well as deterioration of satellite systems [380]. The energy released by explosive flares produces disruptions in the Earth's atmosphere within 8 minutes of the initial emission time [160, 11]. In this study, the perturbation of the ionospheric TEC due to the interaction between SF radiation and the ionosphere was assessed using ROTI variation. Furthermore, the study examined the space weather behavior during the ascending phase of SC 25 through the correlation between solar radio emissions and the occurrence of geomagnetic storms.

5.2 Ionospheric Irregularities

The ascending phase of SC 25 was characterized by more intense solar activity than previously expected [e.g., 381, 65, 382]. Studies by Tan [356]and Sarp et al. [61] predicted SC 25 to be more active than the preceding cycle and prediction is now aligned more closely with observed data. Furthermore, Du [62] estimated that the peak of SC 25 would be 30% stronger than that of SC 24. These findings inferred higher solar activity and presented an opportunity to monitor the intensity of early space weather events in SC 25. To identify disturbed days influenced by ionospheric irregularities linked to GOES X-ray flares, solar radio type II bursts were used as a selection criterion due to their connection with solar events like radio blackouts. The Rate of TEC Index (ROTI) was analyzed for 25 type II radio bursts associated with both solar flares and CMEs, considering GNSS data from stations located in equatorial, mid-latitude, and high-latitude regions. ROTI is used to classify ionospheric TEC irregularities into the following categories: no irregularity (ROTI $<$ 0.25 TECU/min), weak (0.25 $\leq$ROTI $<$ 0.5 TECU/min), moderate (0.5 $\leq$ROTI $<$ 1.0 TECU/min), and strong (ROTI $\geq$ 1.0 TECU/min) [274]. It is worth noting that four large SEP events ($>$ 10 MeV) occurred on days when type II radio bursts were observed. These dates are used as illustrative examples in next sections.

5.2.1 The 28 October 2021 Event

A type II radio burst observed on 28 October 2021 was recorded by the CALLISTO spectrometer at Birr Castle, Ireland. The event occurred between 15:28 UT and 15:38 UT and overlapped with a type IV burst from 15:32 UT to 15:43 UT, as shown in Figure 5.1. This radio activity was linked to an X1.0-class GOES soft X-ray flare that began at 15:17 UT, peaked at 15:35 UT, and ended at 15:38 UT, originating from NOAA Active Region 12887. It was also associated with an energetic halo CME detected by the LASCO C2 coronagraph, first appeared at 15:48 UT with a speed of 1519 km/s. However, this CME did not reach near-Earth space, and no geomagnetic storm was recorded over the following five days. A few minutes after the onset of the type II burst, an increase in proton flux caused a major (R3) radio blackout that impacted South America and the Atlantic Ocean (https://spaceweather.com/images2021/28oct21/blackoutx1.jpg). Figure 5.2 illustrates the resulting ionospheric disturbances using ROTI values across various global regions on the day of the event. While the flare did not directly impact the magnetosphere, its radiations (X-rays, UV, EUV) cause ionospheric perturbations by enhancing ionization levels, leading to GNSS signal delays [e.g., 383]. As shown in Figure 5.2, no significant ionospheric disruption was observed in the equatorial region over Seychelles (Figure 5.2 a), whereas a noticeable suppression in ROTI

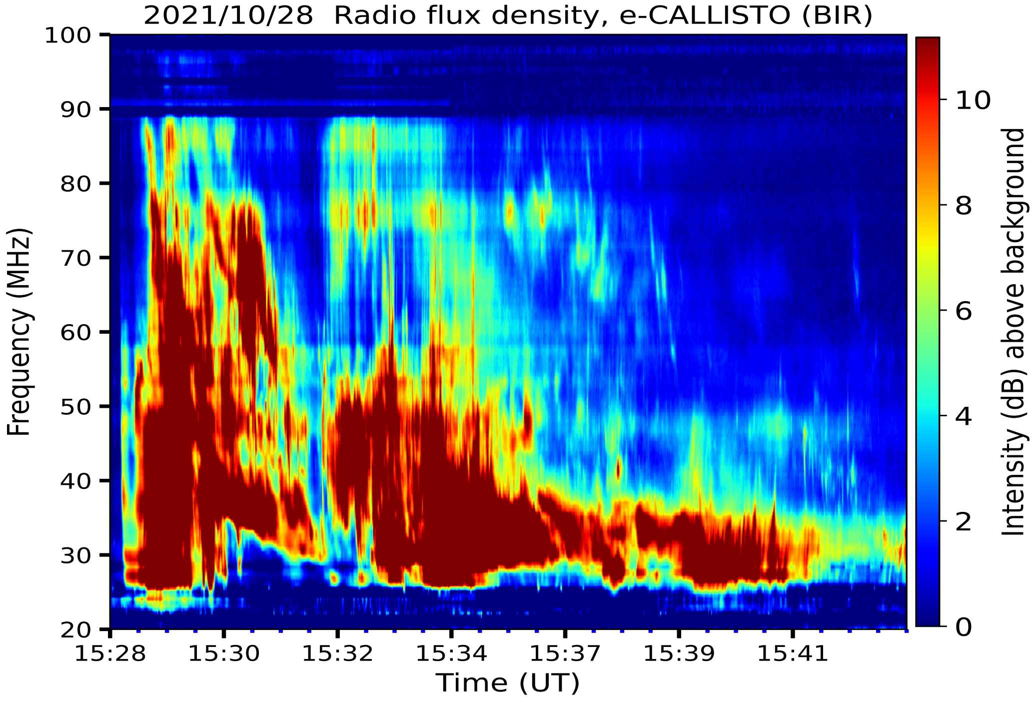

Figure 5.1: Type II radio emissions observed on 28 October 2021 overlapped by a type IV radio emission from 15:32 UT to 15:43 UT.

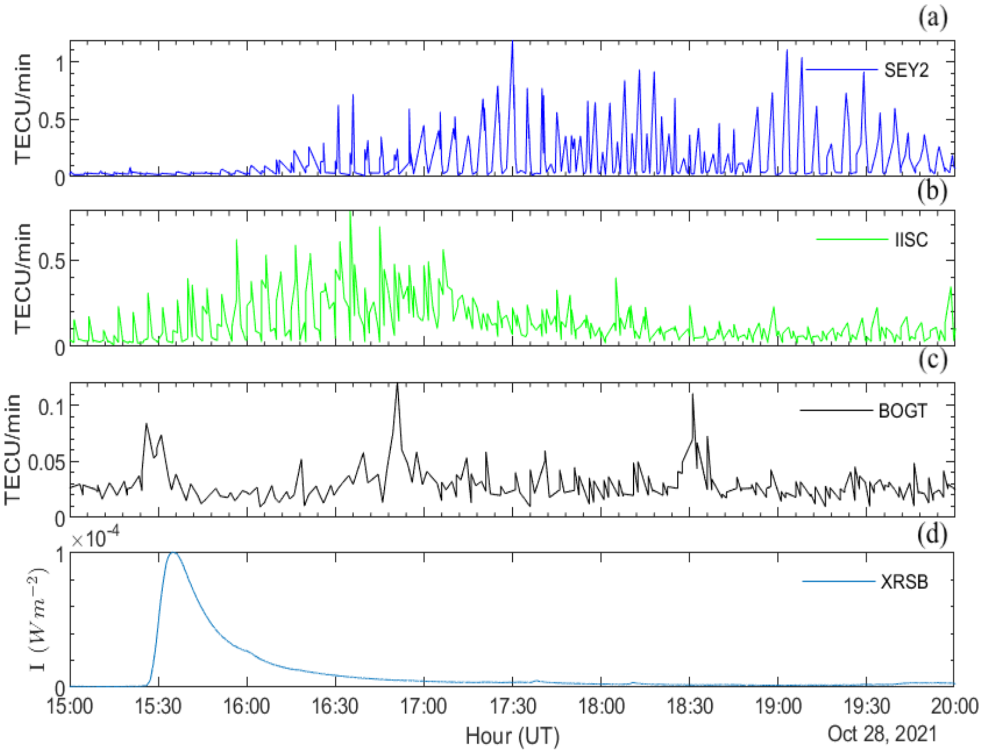

Figure 5.2: ROTI variations observed in (a) the equatorial region (SEY2), (b) the mid-latitude region (IISC), (c) the high-latitude region (BOGT), along with (d) the intensity profile of the associated GOES X1.0-class soft X-ray flare.

was recorded in the mid-latitude region over India (Figure 5.2 b). The ROTI profile in high latitude region over Colombia (Figure 5.2 C) is consistent with the X1.0 flare flux profile (Figure 5.2 d). According to Habarulema et al. [384], the F2 layer was unaffected by the X1.0 flare on 28 October 2021. However, ROTI is strongly suppressed in equatorial region (SEY2) when large SEP arrived at 17:00 UT. On this day, a large SEP (> 10 MeV) was observed with an onset time of roughly 17:00 UT on HED on board ERNE/SOHO, as shown in Figure 5.3. Furthermore, neutron monitor (https://gle.oulu.fi/) recorded the large SEP on 28 October 2021 as the first GLE of SC 25 that started at 15:46 UT [365, 367, 368].

5.2.2 The 28 March 2022 Event

Solar activity was notably elevated during March 2022, marked by the occurrence of several solar events, including seven recorded type II radio bursts. One such event is illustrated in Figure 5.4 , showing a type II radio burst detected by the e-CALLISTO network at Arecibo Observatory, Puerto Rico, USA, between 11:23:12 and 11:28:37 UT on 28 March 2022, spanning a frequency range of 87–32 MHz. This burst was overlapped with a type IV burst that lasted from 11:26 to 11:36 UT. Both were associated with a GOES M4.0-class soft X-ray flare from NOAA AR 12975, which started at 10:58 UT, peaked at 11:29 UT, and ended at 11:45 UT. The eruption also generated a solar atmospheric tsunami (see: https://sdo.gsfc.nasa.gov/data/dailymov/movie.php?q=20220328_1024_0193). A partial halo CME, propagating at 335 km/s, was linked to the event; however, as it was not directed toward Earth, no geomagnetic storm followed. Nevertheless, the flare and the tsunami accelerated protons, leading to a minor radiation storm upon interaction with Earth's

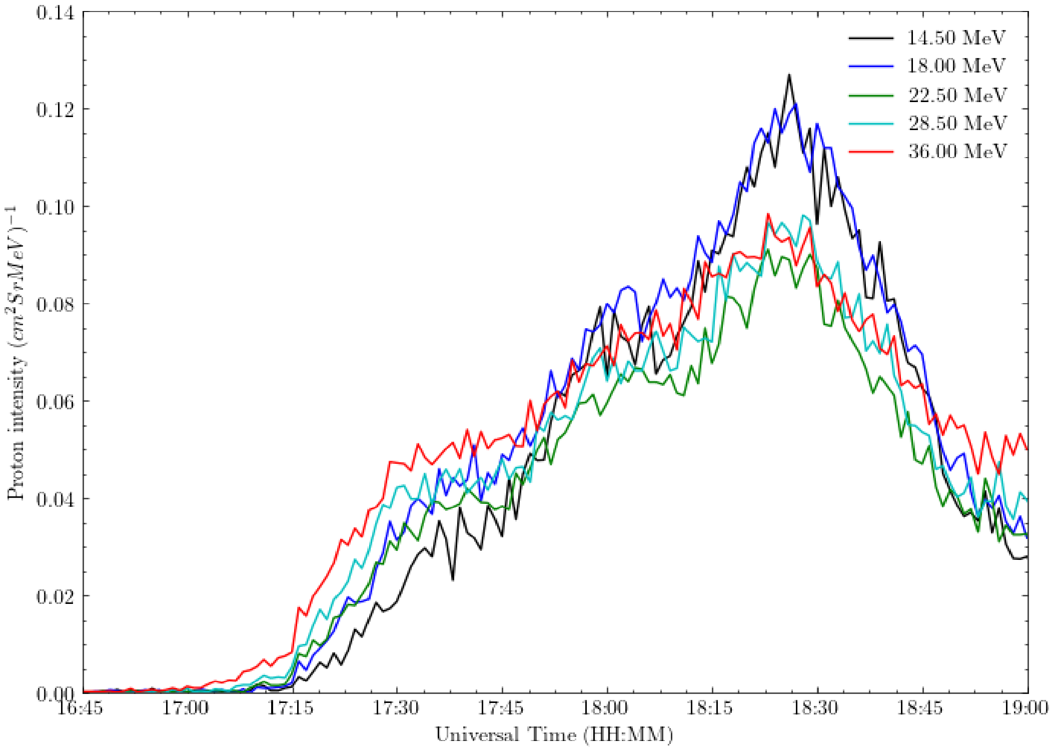

Figure 5.3: Profile of the particle intensity of the SEP on 28 October 2021 in five energy levels onset at 17:00 UT and peak at 18:26 UT.

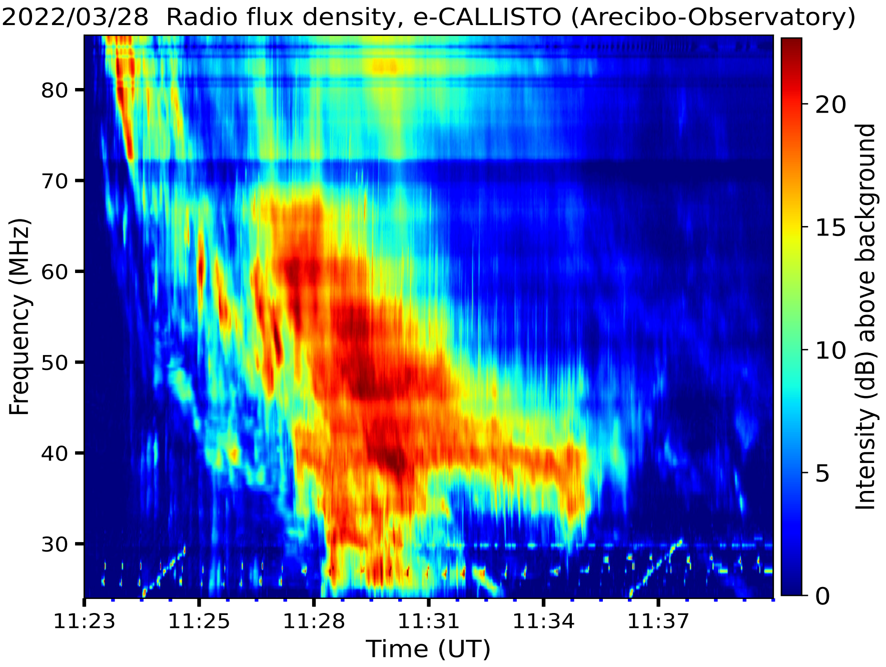

Figure 5.4: The type II radio emissions that are observed on 28 March 2022 from 11:23:12 UT to 11:28:37 UT followed by a type IV radio bursts from 11:26 UT to 11:36 UT.

magnetosphere. The enhancement of proton events is revealed by the radio blackout that covered the whole African continent (https://spaceweather.com/images2022/28mar22/blackout.jpg) and the polar cap absorption event (PCAE) that occurred after about 2:40 UT from the burst onset (https://spaceweather.com/images2022/28mar22/pca.jpg). This event indicated an enhancement in solar proton activity, where HF and Very High Frequency (VHF) signals were absorbed, while lower and very low frequencies were reflected at lower altitudes. Earlier studies have shown that SFs responsible for SEPs are often accompanied by radio bursts and noise storms that disrupt the ionospheric TEC [385], typically occurring within 20 minutes to 20 hours after the flare [386, 387, 388]. These studies also found that SEPs and PCAEs tend to occur more frequently near the solar maximum [389]. However, SC 25 was still in its ascending phase, with its peak expected in 2025. Therefore, the current observations point to elevated solar activity even before reaching the cycle's peak. Notably, the association of type II radio bursts with key space weather phenomena such as SFs, SEPs, and CMEs highlights their importance in space weather research [390, 233]. Figure 5.5 illustrates ionospheric disturbances based on ROTI in response to the solar flare on 28 March 2022. As shown in Figure 5.5 (a), significant TEC disturbances (ROTI > 0.5 TECU/min) were observed at the peak intensity of the M4.0 flare. However, no TEC anomalies were detected in the mid-latitude and equatorial regions (Figure 5.5 b – c). Additionally, the observed suppression of ROTI in the mid-latitudes is attributed to a large SEP event that started around 13:00 UT, with two notable peaks in particle intensity occurred at 15:50 UT and 17:11 UT, respectively. But the mid-latitude region above India has ionospheric irregularity as a result of

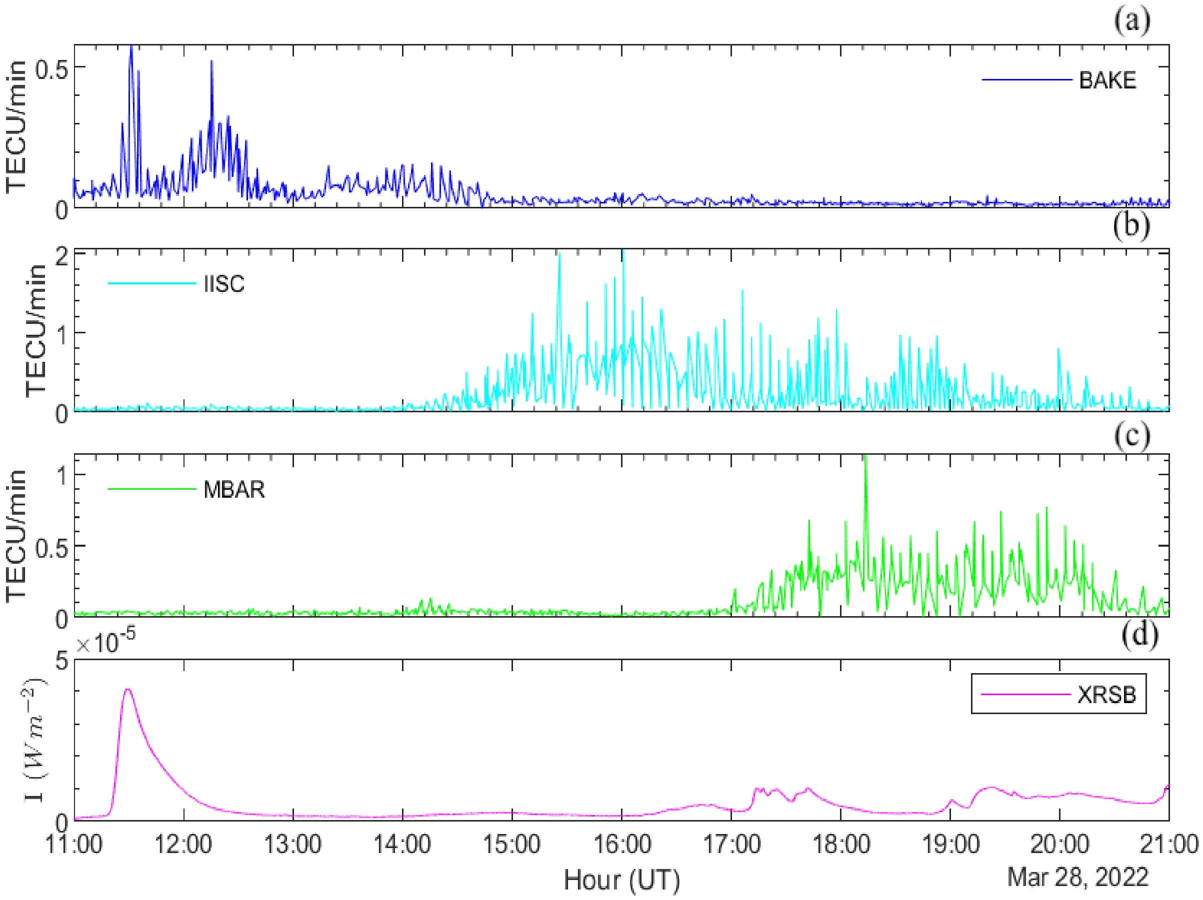

Figure 5.5: ROTI variability in (a) high-latitude region, (b) mid-latitude region, (c) equatorial region, and (d) the associated GOES soft X-ray M4.0 flare on 28 March 2022.

SEP. As ROTI ≥ 0.5 TECU/min indicates, the equatorial region (Mbarara station, Uganda) was impacted by the intensification of the SEP during the ascent towards the second peak.

5.2.3 The 31 March 2022 Event

A type II radio burst was detected by the e-CALLISTO network at the Arecibo Observatory in Puerto Rico, USA, between 18:33 and 18:37 UT on 31 March 2022, within the 76 – 34 MHz frequency range. It was overlapped with a type IV burst that occurred from 18:36 to 18:41 UT. These radio emissions were associated with a GOES soft X-ray flare of M9.6 class that started at 18:17 UT, reached its peak at 18:35 UT, and ended at 18:45 UT, originating from NOAA Active Region 12975. The event was also linked to a halo CME that appeared at 19:12 UT with a speed of 489 km/s, which later triggered a minor geomagnetic storm on 2 April 2022. Further, a large SEP event was observed on the same day, starting at 03:35 UT and peaking at 04:36 UT. Although this SEP event occurred outside the radio burst period and was not associated with any other radio emission, it was believed to have been triggered by CIRs [391, 392, 36, 393], with no corresponding GOES soft X-ray flare. Figure 5.6 displays daily variations in ionospheric TEC, expressed as ROTI, over (a) high-latitude station (INVK), (b) mid-latitude station (IISC), (c) equatorial station (MBAR), and (d) the flux profile of the associated GOES soft X-ray flare.

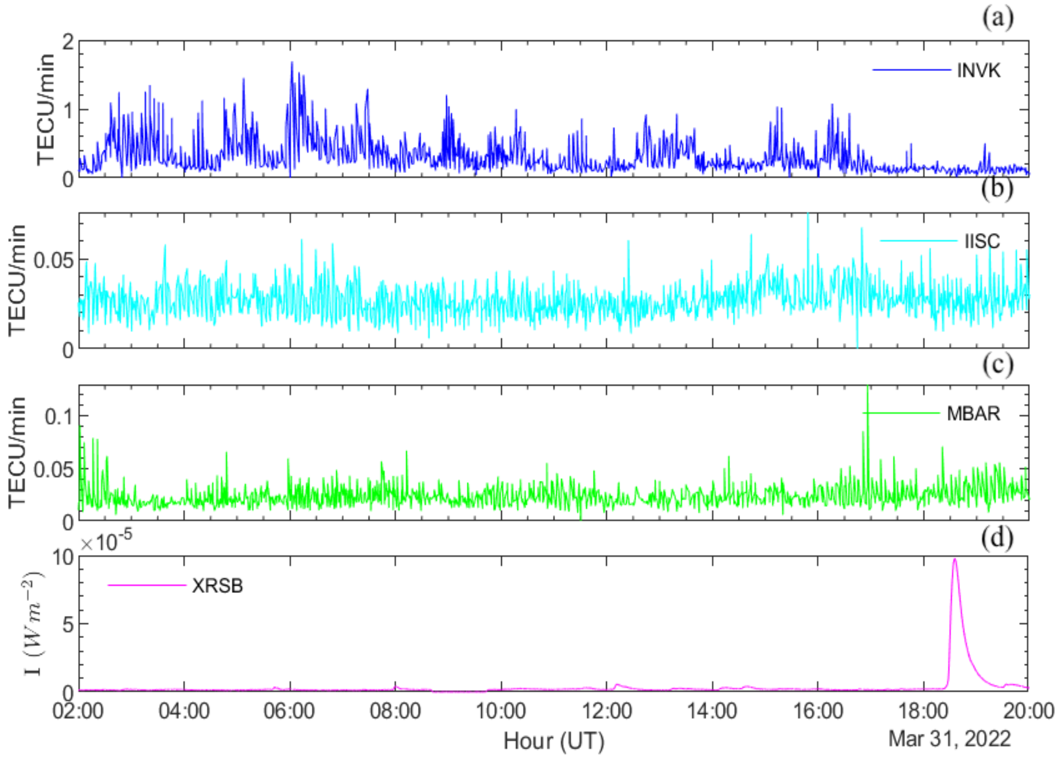

Figure 5.6: Daily variation of the ionospheric TEC in terms of ROTI (a) in high latitude zone (b) in mid latitude region (c) in equatorial region (d) associated GOES soft X-ray flare on 31 March 2022.

Significant TEC disturbances observed at high latitudes (Figure 5.6 a) were attributed to SEP intensification, while no marked irregularities were noted in the mid- and low-latitude regions. Furthermore, there were no anomalies in any of the locations caused by the M9.6 SF. This was believed to be due to electrodynamic coupling of the ionosphere – magnetosphere [394, 395].

5.2.4 The 2 April 2022 Event

April 2022 was marked by significant solar activity. On 2 April 2022, between 13:24 and 13:31 UT, a type II radio burst was observed within the 86 – 30 MHz frequency range, followed by a type IV burst from 13:28 UT to 13:35 UT. These emissions were linked to a GOES soft X-ray flare of M3.9 class, which began at 12:56 UT, peaked at 13:55 UT, and ended at 14:44 UT, originating from NOAA Active Region 12975. During this period, a SEP event occurred, starting at 14:21 UT and peaking at 15:41 UT. Figure 5.7 shows the ionospheric TEC variability in response to both the GOES soft X-ray flare and the SEP across different global regions (a – c).

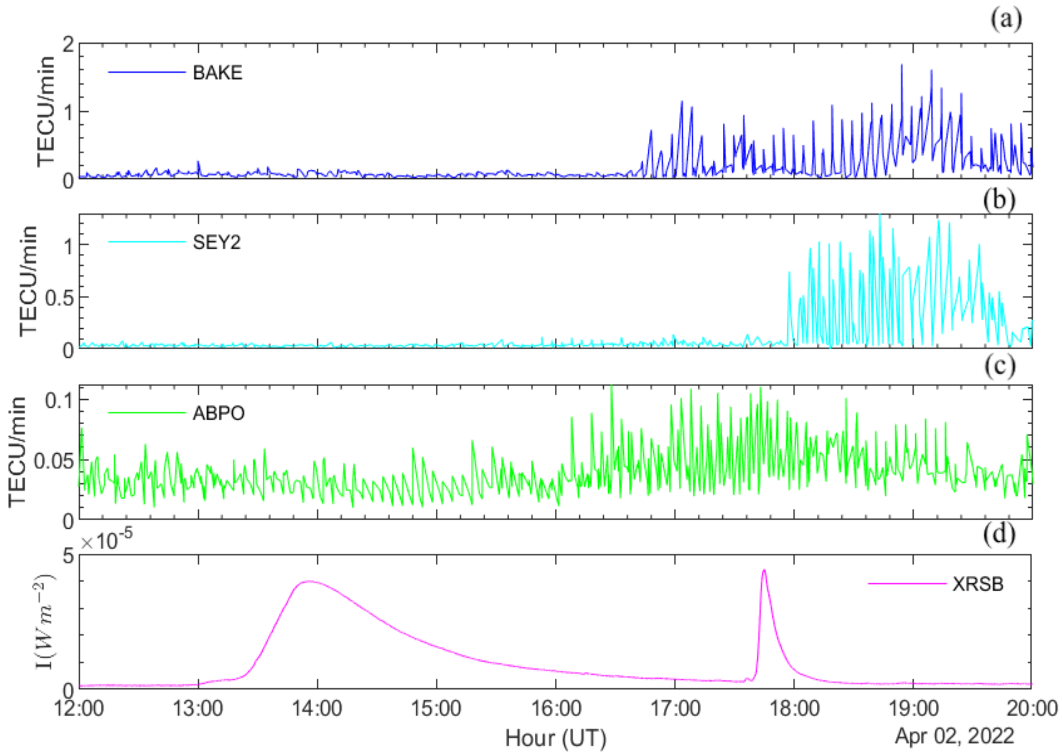

Figure 5.7: Daily variation of the ionospheric TEC in terms of ROTI (a) in the high latitude zone, (b) in the midlatitude region, (c) in the equatorial region, and (d) accompanying GOES soft X-ray flare on 2 April 2022.

As seen in Figure 5.7, no significant TEC variation occurred in any region due to the M3.9 flare or the SEP during this timeframe (Figure 5.7 a–c). It is important to note that particles not deflected by the magnetosphere can become trapped in the Earth's magnetic field [396]. Another M4.3 solar flare erupted from the same active region (AR12975) at 17:34 UT, peaked at 17:44 UT, and ended at 17:51 UT. However, no radio events were detected by the e-CALLISTO network, nor were reported by the Space Weather Prediction Center (SWPC). According to Figure 5.7, substantial fluctuation of ROTI in the high latitude region (BAKE) began before the second SF and was thought to be manifested by the SEP interaction with the magnetosphere. However, the ROTI irregularity began around the peak of the second flare in the mid-latitude region (Figure 5.7 b), suggesting that it was a response to this flare. The equatorial region remained unaffected by all three events (Figure 5.7 c). Based on the scenarios mentioned, it is worth noting that a solar flare lasts between 15 minutes and 2 hours, causing continuous ionization during the event [393].

Additionally, the SEPs follow shortly after the flare, depending on the particles' kinetic energy, pitch angle, and magnetic connectivity [362, 393].

5.3 Geomagnetic Impacts

The manifestations of geomagnetic storms have been better studied than those of other kinds of storms [e.g., 14, 397, 398, 399, 400, 401, 402, 403]. While the ionospheric impacts of geomagnetic storms have been extensively studied over the years and their primary physical drivers are well understood, each storm exhibits distinct characteristics and effects that current empirical models are unable to fully capture [258, 259]. Continued observations of new storm events and further model comparisons are necessary to enhance the accuracy and reliability of these models.

5.3.1 Impacts of Geomagnetic Storm on 10 May 2024

On 10 May 2024 at 17:07 UTC, the simultaneous arrival of several solar CMEs triggered the extreme (G5) geomagnetic storm of the past twenty years, with a minimum Dst of - 412 nT. This event, commonly referred to as the Mother's Day event, is illustrated in Figure 5.8 showing the Dst variation during the storm. Tulasi Ram et al. [404] reported that one of the most intense geomagnetic storms in recent history took place on 10 – 11 May 2024. This event, characterized by a Sym-H index dropping below - 500 nT, ranks as the second strongest geomagnetic storm of the space era. Their analysis showed that the dayside magnetopause was compressed to within geostationary orbit ($6.6\ R_E$) for approximately six continuous hours, driven by strong Solar Wind Dynamic Pressure (SWDP). The storm triggered severe electrodynamic disturbances,

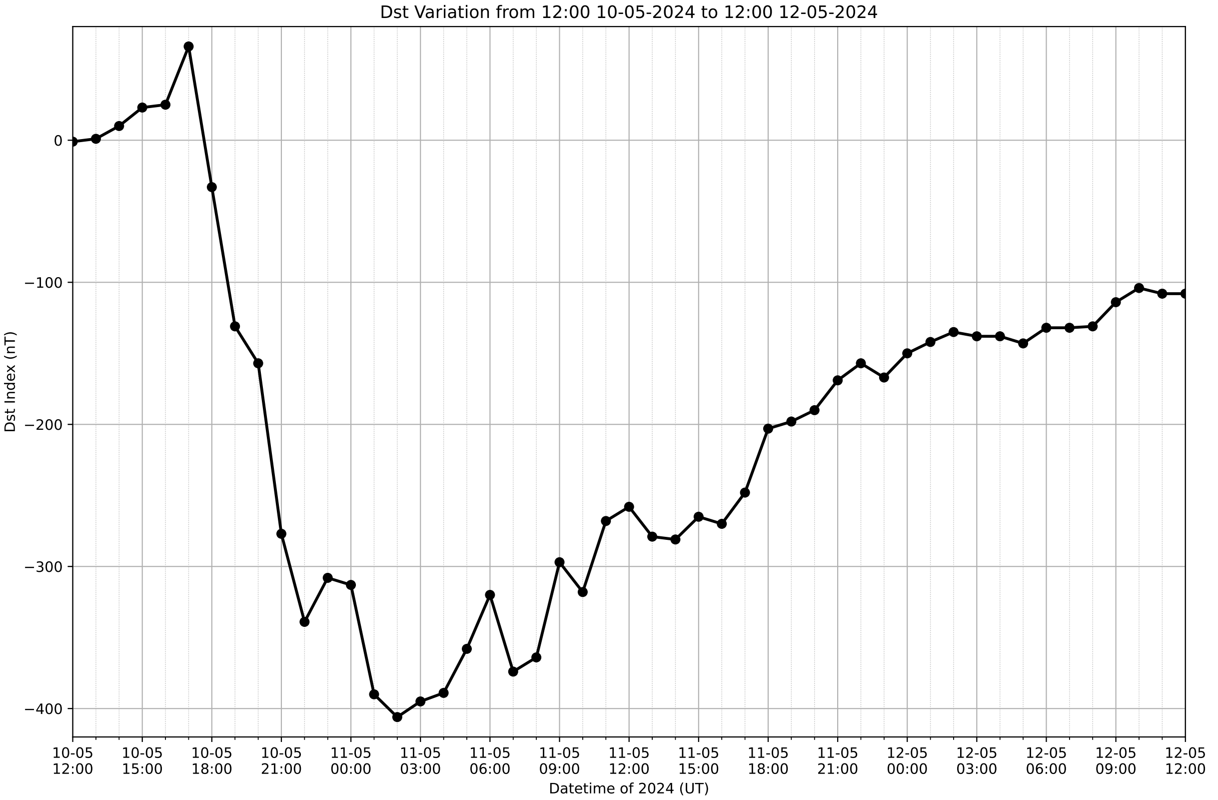

Figure 5.8: Extreme (G5) geomagnetic storm on 10 May 2024, reaching a minimum Dst of - 412 nT.

producing a vigorous positive ionospheric storm marked by a more than 100% rise in dayside TEC, significantly impacting GPS-based positioning and navigation systems. Furthermore, a HF radio blackout occurred in the 2 – 12 MHz band attributed to enhanced D- and E- regions ionization caused by SF that produced the storm. While ionization increases during the main phase of the storms, the electron density decreased for at least one day after the storm and the F2 layer refilled very suddenly after the Mother's Day event, which was highly unusual [405]. The solar source and the radio emission of the Mother's Day Event is represented in Figure 4.19. For a more detailed description of the characteristics and impacts of the Mother's Day event across different altitudes and sectors, the reader is referred to [404, 406, 407, 408, 405]. A second G5 geomagnetic storm of Solar Cycle 25 occurred on 10 October 2024; its impacts on near-Earth environments, as well as its characteristics, are well explored in Oliveira et al. [409].

5.3.2 Impacts of Geomagnetic Storm on 23 April 2023

The radio emission associated with the 23 April 2023 geomagnetic storm is displayed in Figure 4.3, while the corresponding solar source location is presented in Figure 4.4. The IP characteristic parameters of the storm are displayed in Figure 4.5. During the storm, the European Geostationary Navigation Overlay Service (EGNOS) exhibited degraded performance, with significant positioning errors observed at southernmost stations in Africa, Spain, Portugal, and their territories, likely due to the presence of super plasma bubbles [410]. Hajra et al. [411] reported that during the magnetic storm, the equatorial ionospheric anomaly underwent significant structural disruption. Plasma density at around 470 km altitude increased by approximately 60%, while the integrated ionospheric total electron content near the anomaly crests rose by about 80%. Moreover, the latitudinal extent of these enhancements expanded by nearly 33% and 67%, respectively, relative to quiet-time conditions.

5.3.3 Impacts of Geomagnetic Storm on 23 March 2023

On 23 March 2023, a notable reduction in ionospheric density occurred, attributed to prolonged thermospheric wind perturbations. The storm's substantial energy input disrupted thermospheric dynamics, thereby modulating plasma density in the ionosphere [412]. Nykiel et al. [413] reported that ionospheric heating led to an approximately 250% increase in electron temperature above 200 km and in ion temperature above 100 km altitude. Their findings highlight that Joule heating serves as the dominant energy source for nighttime Large-Scale Traveling Ionospheric Disturbances (LSTIDs) originating in the auroral region, while daytime LSTIDs may also be driven by particle precipitation in the polar cusp. They further observed a marked reduction in background plasma density across the European sector the following day, during which clear LSTID signatures were largely absent. Furthermore, the 23 March 2023 geomagnetic storm was not preceded by any radio emission. However, the storm was unusual, disrupted spacecraft operations and caused power grid fluctuations, as reported by the South African National Space Agency (SANSA) (https://africanews.space/sansa-announcement-navigation-and-communications-systems-to-be-impacted-by-severe-geomagnetic-storm/).

5.3.4 Impacts of Geomagnetic Storm on 3 November 2021

Gan et al. [414] observed that during the G3-class geomagnetic storm on 3 November 2021, NASA's Global-scale Observations of the Limb and Disk (GOLD) mission recorded significant changes ranging from 60% to 70% in the thermospheric column density ratio of atomic oxygen to molecular nitrogen, as well as in temperature. Sharon et al. [415] reported a positive ionospheric storm in Asian, East African, West Africa, South America and Pacific West sectors in low-latitude and space-based swarm satellite. Furthermore, TEC fluctuations during the geomagnetic storm, marked by significant disruptions and varying depletion rates, were observed across low-, mid-, and high-latitude regions [416]. The TEC fluctuation due to the flare that cause the storm was described in Section 5.2.1 and the radio emission that preceded the storm is presented in Figure 5.1. However, Figure 4.9 illustrates the characteristics of the IP parameters associated with the storm.

5.3.5 Impacts of Geomagnetic Storm on 27 February 2023

In their investigation of the ionospheric responses to the G3 geomagnetic storm on 27 February 2023, Reznychenko et al. [417] reported a nighttime negative ionospheric storm characterized by an approximately 70% decrease in peak electron density (N_mF_2) during the storm's initial phase, followed by a very strong daytime negative ionospheric storm, with the N_mF_2 reduced by a factor of ~ 4. During the reconstruction of ionospheric electron density (IED) to analyze the spatial distribution and temporal evolution of the ionosphere, Li et al. [418] argued that the storm altered the ionosphere's daily cycle, leading to localized regional peaks in foF_2 and N_mF_2 occurred approximately 1.5 hours earlier. This G3 storm was discussed in Section 4.3.5 and the associated radio emission is displayed in Figure 4.11. In fact, a solar particle event (SPE), characterized by a blast of high-energy protons, began circulating around Earth late on 25 February 2023, intensifying into a near S2-level (Moderate) radiation storm by 26 February 2023 (https://spaceweather.com/images2023/25feb23/protonstorm.jpg).

5.4 Summary

The results of this study showed that 19 out of 32 type II radio events could serve as precursors to space weather phenomena. These events were associated with immediate effects such as radio blackouts, PCAs, exhibited band-splitting features, or were followed by type III and IV bursts. The study also emphasized that ionospheric disturbances are common and depend on the intensity of solar flare classes and/or SEPs, as evidenced by ROTI irregularities; highlighting the value of type II solar radio observations as indicators. We demonstrated that the space weather impacts of geomagnetic storms vary from one event to another, yet ionospheric storms consistently occur regardless of storm intensity. In the five perturbation cases discussed in Section 5.3, all were preceded by solar radio emissions except one, suggesting that solar radio emissions could play a major role in improving geomagnetic forecasts.

Chapter 6

Conclusions, Future Work and Recommendation

6.1 Conclusions

The main objective of the study was to assess the intensity of solar activity during the progression of SC 25, using SRB observations and evaluating their implications for space weather. The results presented have been published in three journal articles.

The study analyzed 32 solar radio type II bursts observed by the e-CALLISTO network between May 2021 and December 2022, during SC 25. The analysis revealed a strong correlation between drift rates and starting frequencies, which are key parameters for determining shock properties. The shock parameters derived from type II radio bursts include bandwidth, drift rate, shock speed, Alfvén speed, Mach number, and magnetic field intensity. The estimated shock and Alfvén speeds range from 504 to 1282kms^{-1} and 368 to 826kms^{-1}, respectively, at heliocentric distances of approximately 1 – 2 $R_{\odot}$. Using the Rankine–Hugoniot approximation, the Mach number was found to range from 1.1 to 1.8, and the magnetic field strength was estimated to vary between 7.8 and 0.7 G. This magnetic field was modeled as $B(r) = 6.07r^{-3.96}$G at $\sim$1.2–1.8$R_{\odot}$, consistent with previous studies. Nineteen out of the 32 type II bursts were associated with direct space weather phenomena, such as radio blackouts and PCAEs. These events exhibited band-splitting properties and were often associated with type III and IV bursts, indicating their potential as space weather precursors. The study also demonstrated that ionospheric disturbances are widespread and depend on the intensity of flare classes and/or SEPs, based on sequences of ROTI irregularities detected by globally distributed GNSS receivers. Thus, observations of solar radio type II bursts were shown to be valuable indicators in this context. The analysis concluded that type II bursts are closely linked to space weather hazards, and understanding their physical characteristics is essential for accurate prediction and forecasting of space weather.

This study was further extended to analyze the correlation between solar radio emissions and geomagnetic storms. The analysis focused on 35 geomagnetic storms with $Dst < -50$ nT, occurred between January 2020 and June 2023. It was found that 23 of these 35 storms were preceded by solar radio type II, III, and IV bursts. The average time lag between the radio burst emissions and the onset of geomagnetic storms was approximately 79 hours, with a range of 48 to 120 hours. Four major geomagnetic storms were examined in detail, those on 4 November 2021, 27 February 2023, 24 March 2023, and 24 April 2023. All were preceded by solar radio emissions except for the 24 March 2023 event. Additionally, two extreme (G5) geomagnetic storms occurred on 11 May 2024 and on 10 October 2024, after the completion of the initial analysis. Each of these intense and severe storms was associated with CMEs containing radially expanding flux ropes. The internal dynamics of the CME cores were thus identified as the source of the associated type II and moving type IV radio bursts. Our findings indicate that while the space weather effects of geomagnetic storms differ from one event to another, ionospheric storms consistently occur, irrespective of the storm's strength. This analysis inferred that the rising phase of SC 25 exhibited higher geomagnetic activity, with solar radio bursts serving as effective observational proxies.

Finally, this study examined the occurrence of large SEP events and their relationship with solar radio emissions during the progression of SC 25. VDA was used to estimate the release times of SEP events from the Sun and their apparent path lengths along IP magnetic field lines. The findings showed that the occurrence of large SEP events aligned with the progression of the sunspot cycle, with SC 25 displaying activity levels more comparable to SC 23 than SC 24, indicating a peak in solar activity higher than that of SC 24. During the study period, approximately 88% of the 122 large SEP events were associated with both SFs and CMEs, while only six events showed no correlation with GOES X-ray flares. The solar source regions of both the flares and their associated SEP events were predominantly located in the western hemisphere of the Sun. Large SEP events were also linked with SRBs, and 36 out of 96 SRBs occurred before the peak of the corresponding solar flares. WAVES/STEREO observations confirmed space counterparts for about 76% of these SRBs, highlighting the dynamics of associated shocks and electron beams propagating along open and quasi-open magnetic field lines. VDA performed on 106 large SEP events yielded apparent path lengths (L) ranging from 1.07 to 3.0 AU. SRBs classified as types II, III, and IV provided diagnostic information about the particle populations accelerated by SFs and CMEs, making them valuable tools for space weather studies. Therefore, the continuous monitoring of solar radio bursts is critical not only for forecasting space weather events but also for improving our understanding of solar coronal and IP processes that drive large SEP events.

The analysis of low-frequency SRBs and their implications for space weather was a central objective of this study. The findings effectively assessed the level of solar activity during SC 25 using SRB observations and examined their associated space weather impacts. The study concludes that SRBs would play a vital role in space weather forecasting and remain a valuable tool for investigating space weather phenomena and understanding the physical processes occurring in the solar corona and IP medium.

6.2 Future work

Spectroscopic investigation of low-frequency solar radio type IV bursts remains a focus in the near future as researchers investigate their feasible emission mechanisms in comparison to proposed microwave burst emission mechanisms. Machine learning is also required to model space weather events from the Sun to Earth, taking into account solar radio parameters and solar wind data in the presence of disturbed geomagnetic conditions.

6.3 Recommendation

It has been noted that many African nations, including Rwanda, have significant gaps in their ground-based space weather observation infrastructures. These gaps make it difficult to collect the data required for space weather research, which in turn restricts the potential development of space weather services and products that could aid in addressing socioeconomic issues [419]. By working with Rwandan researchers in the field, the University of Rwanda can intervene and grant permission to international organizations desiring to contribute and install their equipments such as magnetometers, GPS receivers etc.

References

[1] A. A. Koval, A. A. Stanislavsky, A. A. Konovalenko *et al.*, “Tracking Type III Radio Burst Sources in the Solar Corona by Heliographic Means,” *Odessa Astronomical Publications*, vol. 27, p. 74, 2014.

[2] M. Moldwin, *An Introduction to Space Weather*. Published in the United States of America by Cambridge University Press, New York; ISBN-13 978-0-521-86149-6, Feb. 2008.

[3] J. Adassuriya, S. Gunasekera, K. P. S. Jayaratne *et al.*, “Observation of solar radio bursts using e-callistosystem,” in *Proceedings of the Technical Sessions*, vol. 30. Institute of Physics - Sri Lanka, 03 2014, pp. 43–51.

[4] M. S. White, “Solar radio bursts and space weather,” *Asian J. Phys.*, vol. 16, 01 2007.

[5] D. J. McLean and N. R. Labrum, *Solar radiophysics: Studies of emission from the sun at metre wavelengths*. Cambridge University Press; New York, 1985.

[6] H. V. Cane and W. C. Erickson, “Studies of Space Weather Using Solar Radio Bursts,” in *From Clark Lake to the Long Wavelength Array: Bill Erickson’s Radio Science*, ser. Astronomical Society of the Pacific Conference Series, N. Kassim, M. Perez, W. Junor *et al.*, Eds., vol. 345, Dec. 2005, p. 133.

[7] C. E. Alissandrakis, A. Nindos, S. Patsourakos *et al.*, “A tiny event producing an interplanetary type III burst,” *A&A*, vol. 582, p. A52, Oct. 2015.

[8] V. L. Ginzburg and V. V. Zhelezniakov, “On the Possible Mechanisms of Sporadic Solar Radio Emission (Radiation in an Isotropic Plasma),” *Soviet Astronomy*, vol. 2, p. 653, Oct. 1958.

[9] M. Pick, “Observations of Radio Continua and Terminology,” *Sol. Phys.*, vol. 104, no. 1, pp. 19–32, Mar. 1986.

[10] A. Kumari, D. E. Morosan, and E. K. J. Kilpua, “On the Occurrence of Type IV Solar Radio Bursts in Solar Cycle 24 and Their Association with Coronal Mass Ejections,” *ApJ*, vol. 906, no. 2, p. 79, Jan. 2021.

[11] A. Vourlidas, E. P. Carley, and N. Vilmer, “Radio Observations of Coronal Mass Ejections: Space Weather Aspects,” *Frontiers in Astronomy and Space Sciences*, vol. 7, p. 43, Aug. 2020.

[12] C. T. Russell, X. W. Zhou, P. J. Chi *et al.*, “Sudden compression of the outer magnetosphere associated with an ionospheric mass ejection,” *Geophysical Research Letters*, vol. 26, no. 15, pp. 2343–2346, 1999.

[13] N. Balan, H. Alleyne, S. Walker *et al.*, “Magnetosphere–ionosphere coupling during the cme events of 07–12 november 2004,” *Journal of Atmospheric and Solar-Terrestrial Physics*, vol. 70, no. 17, pp. 2101–2111, 2008, coupling of Solar Wind, Magnetosphere, Ionosphere and Upper Atmosphere.

[14] W. D. Gonzalez, J. A. Joselyn, Y. Kamide *et al.*, “What is a geomagnetic storm?” *Journal of Geophysical Research: Space Physics*, vol. 99, no. A4, pp. 5771–5792, 1994.

[15] Y. Kamide, N. Yokoyama, W. Gonzalez *et al.*, “Two-step development of geomagnetic storms,” *Journal of Geophysical Research: Space Physics*, vol. 103, no. A4, pp. 6917–6921, 1998.

[16] Y. Kamide, W. Baumjohann, I. A. Daglis *et al.*, “Current understanding of magnetic storms: Storm-substorm relationships,” *Journal of Geophysical Research: Space Physics*, vol. 103, no. A8, pp. 17 705–17 728, 1998.

[17] R. G. Rastogi, “Geomagnetic storms and electric fields in the equatorial ionosphere,” *Nature*, vol. 268, no. 5619, pp. 422–424, Aug. 1977.

[18] T. Kikuchi, T. Araki, H. Maeda *et al.*, “Transmission of polar electric fields to the equator,” *Nature*, vol. 273, p. 650, Jun. 1978.

[19] M. C. Kelley, J. J. Makela, J. L. Chau *et al.*, “Penetration of the solar wind electric field into the magnetosphere/ionosphere system,” *Geophysical Research Letters*, vol. 30, no. 4, 2003.

[20] C. M. Huang, M. Q. Chen, and J. Y. Liu, “Ionospheric positive storm phases at the magnetic equator close to sunset,” *Journal of Geophysical Research: Space Physics*, vol. 115, no. A7, 2010.

[21] H. G. Mayr and H. Volland, “Magnetic storm characteristics of the thermosphere,” *Journal of Geophysical Research (1896-1977)*, vol. 78, no. 13, pp. 2251–2264, 1973.

[22] T. J. Fuller-Rowell, M. V. Codrescu, R. J. Moffett *et al.*, “Response of the thermosphere and ionosphere to geomagnetic storms,” *Journal of Geophysical Research: Space Physics*, vol. 99, no. A3, pp. 3893–3914, 1994.

[23] S. Tulasi Ram, C. H. Liu, and S.-Y. Su, “Periodic solar wind forcing due to recurrent coronal holes during 1996–2009 and its impact on earth’s geomagnetic and ionospheric properties during the extreme solar minimum,” *Journal of Geophysical Research: Space Physics*, vol. 115, no. A12, 2010.

[24] N. Matuura, “Theoretical Models of Ionospheric Storms,” *Space Sci. Rev.*, vol. 13, no. 1, pp. 124–189, May 1972.

[25] C. H. Lin, A. D. Richmond, R. A. Heelis *et al.*, “Theoretical study of the low- and midlatitude ionospheric electron density enhancement during the october 2003 superstorm: Relative importance of the neutral wind and the electric field,” *Journal of Geophysical Research: Space Physics*, vol. 110, no. A12, 2005.

[26] R. A. Heelis, J. J. Sojka, M. David *et al.*, “Storm time density enhancements in the middle-latitude dayside ionosphere,” *Journal of Geophysical Research: Space Physics*, vol. 114, no. A3, 2009.

[27] N. Balan, K. Shiokawa, Y. Otsuka *et al.*, “A physical mechanism of positive ionospheric storms at low latitudes and midlatitudes,” *Journal of Geophysical Research: Space Physics*, vol. 115, no. A2, 2010.

[28] G. Lu, L. Goncharenko, M. J. Nicolls *et al.*, “Ionospheric and thermospheric variations associated with prompt penetration electric fields,” *Journal of Geophysical Research: Space Physics*, vol. 117, no. A8, 2012.

[29] J. J. Sojka, M. David, R. W. Schunk *et al.*, “A modeling study of the longitudinal dependence of storm time midlatitude dayside total electron content enhancements,” *Journal of Geophysical Research: Space Physics*, vol. 117, no. A2, 2012.

[30] R. S. Al-Awadi, O. T. Al-Taai, and S. A. Abdullah, “Assessment of x-ray effects on hf radio communications,” *IOP Conference Series: Earth and Environmental Science*, vol. 1223, no. 1, p. 012003, aug 2023.

[31] A. Oljira, “A study of solar flares and geomagnetic storms impact on total electron content over high-latitude region during july- november 2021: The case of tromso station,” *Advances in Space Research*, vol. 72, no. 9, pp. 3868–3881, 2023.

[32] W. Wan, H. Yuan, L. Liu *et al.*, “The sudden increase in ionospheric total electron content caused by the very intense solar flare on july 14, 2000,” *Science in China A: Mathematics*, vol. 45, no. S1, pp. 142–147, Oct. 2002.

[33] S. Kumar and A. Singh, “Effect of solar flares on ionospheric tec at varanasi, near eia crest, during solar minimum period,” *Indian J Radio & Space Physics*, vol. 41, pp. 141 – 147, April 2012.

[34] X. Pi, A. J. Mannucci, U. J. Lindqwister *et al.*, “Monitoring of global ionospheric irregularities using the Worldwide GPS Network,” *Geophys. Res. Lett.*, vol. 24, no. 18, pp. 2283–2286, Sep. 1997.

[35] Y. Liu, Z. Li, L. Fu *et al.*, “Analyzing ionosphere tec and roti responses on 2010 august high speed solar winds,” *IEEE Access*, vol. 7, pp. 29 788–29 804, 2019.

[36] I. G. Richardson, L. M. Barbier, D. V. Reames *et al.*, "Corotating mev/amu ion enhancements at $\leq$1 au from 1978 to 1986," *Journal of Geophysical Research: Space Physics*, vol. 98, no. A1, pp. 13–32, 1993.

[37] J. T. Gosling and V. J. Pizzo, "Formation and Evolution of Corotating Interaction Regions and Their Three Dimensional Structure," in *Corotating Interaction Regions. Series: Space Sciences Series of ISSI*, A. Balogh, J. T. Gosling, J. R. Jokipii *et al.*, Eds., 1999, vol. 7, pp. 21–52.

[38] J. Zhang, I. G. Richardson, D. F. Webb *et al.*, "Solar and interplanetary sources of major geomagnetic storms (Dst ¡= -100 nT) during 1996-2005," *Journal of Geophysical Research (Space Physics)*, vol. 112, no. A10, p. A10102, Oct. 2007.

[39] W. D. Gonzalez, E. Echer, B. T. Tsurutani *et al.*, "Interplanetary Origin of Intense, Superintense and Extreme Geomagnetic Storms," *Space Sci. Rev.*, vol. 158, no. 1, pp. 69–89, Jan. 2011.

[40] A. K. Singh, A. Bhargawa, D. Siingh *et al.*, "Physics of space weather phenomena: A review," *Geosciences*, vol. 11, no. 7, 2021.

[41] D. Nandy, "Progress in Solar Cycle Predictions: Sunspot Cycles 24-25 in Perspective," *Sol. Phys.*, vol. 296, no. 3, p. 54, Mar. 2021.

[42] S. W. McIntosh, S. Chapman, R. J. Leamon *et al.*, "Overlapping Magnetic Activity Cycles and the Sunspot Number: Forecasting Sunspot Cycle 25 Amplitude," *Sol. Phys.*, vol. 295, no. 12, p. 163, Dec. 2020.

[43] N. Chrysaphi, "Fine structures of solar radio bursts: origins and radio-wave propagation effects," Ph.D. dissertation, University of Glasgow, School of Physics and Astronomy, Feb. 2021.

[44] A. O. Benz, C. Monstein, and H. Meyer, "Callisto A New Concept for Solar Radio Spectrometers," *Sol. Phys.*, vol. 226, no. 1, pp. 143–151, Jan. 2005.

[45] A. O. Benz, C. Monstein, H. Meyer *et al.*, "A World-Wide Net of Solar Radio Spectrometers: e-CALLISTO," *Earth Moon and Planets*, vol. 104, no. 1-4, pp. 277–285, apr 2009.

[46] A. C. Christian Monstein and A. O. Benz, "Callisto solar spectrogram fits files [data set]," *International Space Weather Initiative (ISWI)*, 2023.

[47] P. Zucca, D. E. Morosan, A. P. Rouillard *et al.*, "Shock location and CME 3D reconstruction of a solar type II radio burst with LOFAR," *A & A*, vol. 615, p. A89, Jul. 2018.

[48] S. Mondal, D. Oberoi, and A. Vourlidas, "Estimation of the Physical Parameters of a CME at High Coronal Heights Using Low-frequency Radio Observations," *ApJ*, vol. 893, no. 1, p. 28, Apr. 2020.

[49] D. E. Morosan, E. K. J. Kilpua, E. P. Carley *et al.*, "Variable emission mechanism of a Type IV radio burst," *A&A*, vol. 623, p. A63, Mar. 2019.

[50] G. A. Dulk and D. J. McLean, "Coronal magnetic fields." *Sol. Phys.*, vol. 57, no. 2, pp. 279–295, Apr. 1978.

[51] N. Gopalswamy, A. Lara, M. L. Kaiser *et al.*, "Near-Sun and near-Earth manifestations of solar eruptions," *J. Geophys. Res.*, vol. 106, no. A11, pp. 25 261–25 278, Nov. 2001.

[52] K. S. Cho, J. Lee, D. E. Gary *et al.*, "Magnetic Field Strength in the Solar Corona from Type II Band Splitting," *ApJ*, vol. 665, no. 1, pp. 799–804, Aug. 2007.

[53] R. Ramesh, C. Kathiravan, and C. V. Sastry, "Estimation of Magnetic Field in the Solar Coronal Streamers Through Low Frequency Radio Observations," *ApJ*, vol. 711, no. 2, pp. 1029–1032, Mar. 2010.

[54] N. Gopalswamy, N. Nitta, S. Akiyama *et al.*, "Coronal Magnetic Field Measurement from EUV Images Made by the Solar Dynamics Observatory," *ApJ*, vol. 744, no. 1, p. 72, Jan. 2012.

[55] R. S. Kim, N. Gopalswamy, Y. J. Moon *et al.*, "Magnetic Field Strength in the Upper Solar Corona Using White-light Shock Structures Surrounding Coronal Mass Ejections," *ApJ*, vol. 746, no. 2, p. 118, Feb. 2012.

[56] N. Gopalswamy, H. Xie, P. Mäkelä *et al.*, "Height of shock formation in the solar corona inferred from observations of type ii radio bursts and coronal mass ejections," *Advances in Space Research*, vol. 51, no. 11, pp. 1981–1989, 2013.

[57] K. Sasikumar Raja, R. Ramesh, K. Hariharan *et al.*, "An Estimate of the Magnetic Field Strength Associated with a Solar Coronal Mass Ejection from Low Frequency Radio Observations," *ApJ*, vol. 796, no. 1, p. 56, Nov. 2014.

[58] P. Kishore, R. Ramesh, K. Hariharan *et al.*, "Constraining the Solar Coronal Magnetic Field Strength using Split-band Type II Radio Burst Observations," *ApJ*, vol. 832, no. 1, p. 59, Nov. 2016.

[59] A. Kumari, R. Ramesh, C. Kathiravan *et al.*, "Addendum to: Strength of the Solar Coronal Magnetic Field - A Comparison of Independent Estimates Using Contemporaneous Radio and White-Light Observations," *Sol. Phys.*, vol. 292, no. 12, p. 177, Dec. 2017.

[60] K. Sasikumar Raja, S. Venkata, J. Singh *et al.*, "Solar coronal magnetic fields and sensitivity requirements for spectropolarimetry channel of VELC onboard Aditya-L1," *Advances in Space Research*, vol. 69, no. 1, pp. 814–822, Jan. 2022.

[61] V. Sarp, A. Kilcik, V. Yurchyshyn *et al.*, "Prediction of solar cycle 25: a non-linear approach," *MNRAS*, vol. 481, no. 3, pp. 2981–2985, Dec. 2018.

[62] Z. L. Du, “The solar cycle: predicting the peak of solar cycle 25,” *Astrophysics and Space Science*, vol. 365, no. 6, p. 104, Jun. 2020.

[63] G. D. Fleishman, D. E. Gary, B. Chen *et al.*, “Decay of the coronal magnetic field can release sufficient energy to power a solar flare,” *Science*, vol. 367, no. 6475, pp. 278–280, Jan. 2020.

[64] A. Nindos, “Incoherent Solar Radio Emission,” *Frontiers in Astronomy and Space Sciences*, vol. 7, p. 57, Nov. 2020.

[65] M. Hapgood, H. Liu, and N. Lugaz, “Spacex—sailing close to the space weather?” *Space Weather*, vol. 20, no. 3, p. e2022SW003074, 2022.

[66] N. Gopalswamy, G. Michalek, S. Yashiro *et al.*, “What Do Halo CMEs Tell Us about Solar Cycle 25?” *ApJ Lett.*, vol. 952, no. 1, p. L13, Jul. 2023.

[67] T. I. Gombosi, *Physics of the Space Environment*. UK: Cambridge University Press, ISBN 052160768X, August 2004. chap.11, Aug. 2004.

[68] F. Breitling, G. Mann, and C. Vocks, “Propagation of Energetic Electrons from the Corona into Interplanetary Space and Type III Radio Emission,” *Planetary, Solar and Heliospheric Radio Emissions (PRE VII)*, pp. 373–380, 2015.

[69] J. O. Bennett, M. Donahue, N. Schneider *et al.*, *The Essential Cosmic Perspective Media Update*, 2006.

[70] C. J. Schrijver and C. Zwaan, *Solar and Stellar Magnetic Activity*, 2000.

[71] M. V. Zombeck, *Handbook of space astronomy and astrophysics*, 1990.

[72] M. G. Kivelson and C. T. Russell, *Introduction to Space Physics*, 1995.

[73] K. R. Lang, *The Cambridge Encyclopedia of the Sun*, 2001.

[74] E. E. Mamajek, A. Prsa, G. Torres *et al.*, “IAU 2015 Resolution B3 on Recommended Nominal Conversion Constants for Selected Solar and Planetary Properties,” *arXiv e-prints*, p. arXiv:1510.07674, Oct. 2015.

[75] H. W. Babcock, “The Topology of the Sun’s Magnetic Field and the 22-Year Cycle.” *ApJ*, vol. 133, p. 572, Mar. 1961.

[76] K. J. Li, W. Feng, X. J. Shi *et al.*, “Long-Term Variations of Solar Differential Rotation and Sunspot Activity: Revisited,” *Sol. Phys.*, vol. 289, no. 3, pp. 759–768, Mar. 2014.

[77] P. Chowdhury, D. P. Choudhary, and S. Gosain, “A Study of the Hemispheric Asymmetry of Sunspot Area during Solar Cycles 23 and 24,” *ApJ*, vol. 768, no. 2, p. 188, May 2013.

[78] J. Sharma, A. K. Malik, B. Kumar *et al.*, “Evidence of a strong relationship between hemispheric asymmetry in solar coronal rotation and solar activity during solar cycle 24,” *MNRAS*, vol. 499, no. 4, pp. 5442–5446, Dec. 2020.

[79] W. Livingston, “Sunspots Observed to Physically Weaken in 2000-2001,” *Sol. Phys.*, vol. 207, no. 1, pp. 41–45, May 2002.

[80] R. J. Thompson and K. Cantner, “Here comes the solar maximum: What we know - and don’t know - about solar storms and their hazards,” 2012.

[81] P. Zucca, “Radio spectroscopy and imaging of coronal shocks,” Ph.D. dissertation, University of Dublin Trinity College, Ireland, Jan. 2015.

[82] F. Breitling, “Propagation of energetic electrons in the solar corona observed with lofar,” doctoralthesis, Universität Potsdam, 2016.

[83] Y. Kamide and A. C.-L. Chian, *Handbook of the Solar-Terrestrial Environment.* Springer, Berlin, Heidelberg, ISBN 978-3-540-46314-6, 2007.

[84] L. van Driel-Gesztelyi and L. M. Green, “Evolution of Active Regions,” *Living Reviews in Solar Physics*, vol. 12, no. 1, p. 1, Sep. 2015.

[85] M. J. Aschwanden, *Physics of the Solar Corona. An Introduction*, 2004.

[86] D. H. Hathaway, “The Solar Cycle,” *Living Reviews in Solar Physics*, vol. 12, no. 1, p. 4, Dec. 2015.

[87] L. van Driel-Gesztelyi and M. J. Owens, “Solar cycle,” 07 2020.

[88] F. Carta, F. Chlistovsky, A. Manara *et al.*, “A comparative spectral analysis of the earth’s rotation and the solar activity,” *A & A*, vol. 114, no. 2, pp. 388–393, Oct. 1982.

[89] D. Djurović and P. Pâquet, “The Common Oscillations of Solar Activity, the Geomagnetic Field, and the Earth’s Rotation,” *Sol. Phys.*, vol. 167, no. 1-2, pp. 427–439, Aug. 1996.

[90] K. Mursula, I. Usoskin, and B. Zieger, “On the Claimed 5.5-year Periodicity in Solar Activity,” *Sol. Phys.*, vol. 176, no. 1, pp. 201–210, Nov. 1997.

[91] A. K. Singh, D. Siingh, and R. P. Singh, “Space weather: Physics, effects and predictability,” *Surveys in Geophysics*, vol. 31, no. 6, pp. 581–638, Dec 2010.

[92] G. Kopp, G. Lawrence, and G. Rottman, “The Total Irradiance Monitor (TIM): Science Results,” *Sol. Phys.*, vol. 230, no. 1-2, pp. 129–139, Aug. 2005.

[93] R. C. Canfield, M. J. Penn, J.-P. Wulser *et al.*, “H alpha Spectra of Dynamic Chromospheric Processes in Five Well-observed X-Ray Flares,” *ApJ*, vol. 363, p. 318, Nov. 1990.

[94] A. Falchi, R. Falciani, and L. A. Smaldone, "Analysis of the optical spectra of the solar flares. VI. Velocity field in the 13 June 1980 flare area." *A&A*, vol. 256, no. 1, pp. 255–263, Mar. 1992.

[95] P. Heinzel, M. Karlicky, P. Kotrc *et al.*, "On the Occurrence of Blue Asymmetry in Chromospheric Flare Spectra," *Sol. Phys.*, vol. 152, no. 2, pp. 393–408, Jul. 1994.

[96] D. F. Neidig, P. H. Wiborg, and L. B. Gilliam, "Physical properties of white-light flares derived from their center-to-limb distribution," *Sol. Phys.*, vol. 144, no. 1, pp. 169–194, Mar. 1993.

[97] M. Kretzschmar, "The Sun as a star: observations of white-light flares," *A&A*, vol. 530, p. A84, Jun. 2011.

[98] Q. Hao, K. Yang, X. Cheng *et al.*, "A circular white-light flare with impulsive and gradual white-light kernels," *Nature Communications*, vol. 8, p. 2202, Dec. 2017.

[99] J. Uwamahoro, L. A. McKinnell, and J. B. Habarulema, "Estimating the geoeffectiveness of halo CMEs from associated solar and IP parameters using neural networks," *Annales Geophysicae*, vol. 30, no. 6, pp. 963–972, Jun. 2012.

[100] K. Bocchialini, B. Grison, M. Menvielle *et al.*, "Statistical Analysis of Solar Events Associated with Storm Sudden Commencements over One Year of Solar Maximum During Cycle 23: Propagation from the Sun to the Earth and Effects," *Sol. Phys.*, vol. 293, no. 5, p. 75, May 2018.

[101] V. Bothmer and I. A. Daglis, *Space weather: physics and effects*. Springer Science & Business Media, 2007.

[102] G. E. Brueckner, R. A. Howard, M. J. Koomen *et al.*, "The Large Angle Spectroscopic Coronagraph (LASCO)," *Sol. Phys.*, vol. 162, no. 1-2, pp. 357–402, Dec. 1995.

[103] V. Domingo, B. Fleck, and A. I. Poland, "SOHO: The Solar and Heliospheric Observatory," *Space Sci. Rev.*, vol. 72, no. 1-2, pp. 81–84, Apr. 1995.

[104] N. Gopalswamy, "Coronal Mass Ejections and Solar Radio Emissions," in *Planetary, Solar and Heliospheric Radio Emissions (PRE VII)*, H. O. Rucker, W. S. Kurth, P. Louarn *et al.*, Eds., Jan. 2011, pp. 325–342.

[105] D. F. Webb, E. W. Cliver, N. U. Crooker *et al.*, "Relationship of halo coronal mass ejections, magnetic clouds, and magnetic storms," *J. Geophys. Res.*, vol. 105, no. A4, pp. 7491–7508, Apr. 2000.

[106] N. Gopalswamy, "Coronal mass ejections and space weather," in *Climate and Weather of the Sun-Earth System (CAWSES): Selected Papers from the 2007 Kyoto Symposium*, T. Tsuda, R. Fujii, K. Shibata *et al.*, Eds., May 2009, pp. 77–120.

[107] X. P. Zhao and D. F. Webb, “Source regions and storm effectiveness of frontside full halo coronal mass ejections,” *Journal of Geophysical Research (Space Physics)*, vol. 108, no. A6, p. 1234, Jun. 2003.

[108] N. Gopalswamy, S. Yashiro, and S. Akiyama, “Geoeffectiveness of halo coronal mass ejections,” *Journal of Geophysical Research (Space Physics)*, vol. 112, no. A6, p. A06112, Jun. 2007.

[109] R. Miteva, K.-L. Klein, O. Malandraki *et al.*, “Solar Energetic Particle Events in the 23rd Solar Cycle: Interplanetary Magnetic Field Configuration and Statistical Relationship with Flares and CMEs,” *Sol. Phys.*, vol. 282, pp. 579–613, feb 2013.

[110] R. Miteva, K.-L. Klein, S. W. Samwel *et al.*, “Radio Signatures of Solar Energetic Particles During the 23ˆrd Solar Cycle,” *Central European Astrophysical Bulletin*, vol. 37, pp. 541–553, 2013.

[111] R. Miteva, S. W. Samwel, and V. Krupar, “Solar energetic particles and radio burst emission,” *Journal of Space Weather and Space Climate*, vol. 7, no. 27, p. A37, dec 2017.

[112] M. Paassilta, O. Raukunen, R. Vainio *et al.*, “Catalogue of 55-80 MeV solar proton events extending through solar cycles 23 and 24,” *Journal of Space Weather and Space Climate*, vol. 7, no. 27, p. A14, Jun. 2017.

[113] S. R. Cranmer, “Solar-Wind Origin,” in *Oxford Research Encyclopedia of Physics*, 2019, p. 18.

[114] C. Arridge, “Solar wind: Interaction with planets,” 07 2020.

[115] D. J. McComas, R. W. Ebert, H. A. Elliott *et al.*, “Weaker solar wind from the polar coronal holes and the whole Sun,” *Geophys. Res. Lett.*, vol. 35, no. 18, p. L18103, Sep. 2008.

[116] R. Schwenn, *Large-Scale Structure of the Interplanetary Medium*, 1990, p. 99.

[117] Y. M. Wang and J. Sheeley, N. R., “Coronal Mass Ejections and the Solar Cycle Variation of the Sun’s Open Flux,” *ApJ Lett.*, vol. 809, no. 2, p. L24, Aug. 2015.

[118] J. Newkirk, Gordon, “Structure of the Solar Corona,” *Annu. Rev. Astron. Astrophys.*, vol. 5, p. 213, Jan. 1967.

[119] J. A. Klimchuk and C. DeForest, “Cross Sections of Coronal Loop Flux Tubes,” in *AGU Fall Meeting Abstracts*, vol. 2020, Dec. 2020, pp. SH037–0001.

[120] M. J. Owens, “Solar-wind structure,” 02 2020.

[121] E. J. Smith, “The heliospheric current sheet and modulation of galactic cosmic rays,” *J Geophys. Res.*, vol. 95, no. A11, pp. 18 731–18 743, Nov. 1990.

[122] Y. M. Wang, R. Grappin, E. Robbrecht *et al.*, “On the Nature of the Solar Wind from Coronal Pseudostreamers,” *ApJ*, vol. 749, no. 2, p. 182, Apr. 2012.

[123] G. W. Prölss and M. K. Bird, *Physics of the Earth’s Space Environment: an introduction*, 2004.

[124] N. Meyer-Vernet, *Basics of the Solar Wind*, 2007.

[125] J. E. Borovsky and M. H. Denton, “Compressional perturbations of the dayside magnetosphere during high-speed-stream-driven geomagnetic storms,” *Journal of Geophysical Research: Space Physics*, vol. 121, no. 5, pp. 4569–4589, 2016.

[126] C. Cattell, A. Breneman, C. Colpitts *et al.*, “Dayside response of the magnetosphere to a small shock compression: Van allen probes, magnetospheric multiscale, and goes-13,” *Geophysical Research Letters*, vol. 44, no. 17, pp. 8712–8720, 2017.

[127] N. Ganushkina, A. Jaynes, and M. Liemohn, “Space Weather Effects Produced by the Ring Current Particles,” *Space Science Reviews*, vol. 212, no. 3-4, pp. 1315–1344, Nov. 2017.

[128] M. Stepanova, E. Antonova, P. Moya *et al.*, “Multisatellite analysis of plasma pressure in the inner magnetosphere during the 1 june 2013 geomagnetic storm,” *Journal of Geophysical Research: Space Physics*, vol. 124, no. 2, pp. 1187–1202, 2019.

[129] P. S. Moya, V. A. Pinto, D. G. Sibeck *et al.*, “On the effect of geomagnetic storms on relativistic electrons in the outer radiation belt: Van allen probes observations,” *Journal of Geophysical Research: Space Physics*, vol. 122, no. 11, pp. 11,100–11,108, 2017.

[130] D. L. Turner, T. P. O’Brien, J. F. Fennell *et al.*, “The effects of geomagnetic storms on electrons in earth’s radiation belts,” *Geophysical Research Letters*, vol. 42, no. 21, pp. 9176–9184, 2015.

[131] D. L. Turner, E. K. J. Kilpua, H. Hietala *et al.*, “The response of earth’s electron radiation belts to geomagnetic storms: Statistics from the van allen probes era including effects from different storm drivers,” *Journal of Geophysical Research: Space Physics*, vol. 124, no. 2, pp. 1013–1034, 2019.

[132] M. J. Engebretson, M. R. Lessard, J. Bortnik *et al.*, “Pc1–pc2 waves and energetic particle precipitation during and after magnetic storms: Superposed epoch analysis and case studies,” *Journal of Geophysical Research: Space Physics*, vol. 113, no. A1, 2008.

[133] N. Longden, M. H. Denton, and F. Honary, “Particle precipitation during icme-driven and cir-driven geomagnetic storms,” *Journal of Geophysical Research: Space Physics*, vol. 113, no. A6, 2008.

[134] A. Pulkkinen, S. Lindahl, A. Viljanen *et al.*, “Geomagnetic storm of 29–31 october 2003: Geomagnetically induced currents and their relation to problems in the swedish high-voltage power transmission system,” *Space Weather*, vol. 3, no. 8, 2005.

[135] Y. Shi, E. Zesta, and L. R. Lyons, “Modeling magnetospheric current response to solar wind dynamic pressure enhancements during magnetic storms: 1. methodology and results of the 25 september 1998 peak main phase case,” *Journal of Geophysical Research: Space Physics*, vol. 113, no. A10, 2008.

[136] S. C. Chapman, R. B. Horne, and N. W. Watkins, “Using the index over the last 14 solar cycles to characterize extreme geomagnetic activity,” *Geophysical Research Letters*, vol. 47, no. 3, p. e2019GL086524, 2020.

[137] M. Menvielle and A. Marchaudon, “Geomagnetic Indices in Solar-Terrestrial Physics and Space Weather,” in *Space Weather : Research Towards Applications in Europe 2nd European Space Weather Week (ESWW2)*, ser. Astrophysics and Space Science Library, J. Lilensten, Ed., vol. 344, Jan. 2007, p. 277.

[138] M. Menvielle, T. Iyemori, A. Marchaudon *et al.*, *Geomagnetic Indices*. Dordrecht: Springer Netherlands, 2011, pp. 183–228.

[139] R. A. Howard, J. D. Moses, A. Vourlidas *et al.*, “Sun Earth Connection Coronal and Heliospheric Investigation (SECCHI),” *Space Sci. Rev.*, vol. 136, no. 1-4, pp. 67–115, Apr. 2008.

[140] M. Kaiser, “The stereo mission: an overview,” *Advances in Space Research*, vol. 36, no. 8, pp. 1483–1488, 2005, solar Encounter, Solar-B and STEREO.

[141] H. O. Rucker, W. Macher, G. Fischer *et al.*, “Analysis of spacecraft antenna systems: Implications for STEREO/WAVES,” *Advances in Space Research*, vol. 36, no. 8, pp. 1530–1533, Jan. 2005.

[142] E. C. Stone, A. M. Frandsen, R. A. Mewaldt *et al.*, “The Advanced Composition Explorer,” *Space Sci. Rev.*, vol. 86, pp. 1–22, Jul. 1998.

[143] J. L. Burch, T. E. Moore, R. B. Torbert *et al.*, “Magnetospheric Multiscale Overview and Science Objectives,” *Space Sci. Rev.*, vol. 199, no. 1-4, pp. 5–21, Mar. 2016.

[144] N. Buzulukova and B. Tsurutani, “Space weather: From solar origins to risks and hazards evolving in time,” *Frontiers in Astronomy and Space Sciences*, vol. 9, 2022.

[145] S. R. Cranmer, “Coronal Holes,” *Living Reviews in Solar Physics*, vol. 6, no. 1, p. 3, Sep. 2009.

[146] K. Shibata and T. Magara, “Solar Flares: Magnetohydrodynamic Processes,” *Living Reviews in Solar Physics*, vol. 8, no. 1, p. 6, Dec. 2011.

[147] S. Toriumi and H. Wang, “Flare-productive active regions,” *Living Reviews in Solar Physics*, vol. 16, no. 1, p. 3, May 2019.

[148] E. J. Smith and J. H. Wolfe, “Observations of interaction regions and corotating shocks between one and five au: Pioneers 10 and 11,” *Geophysical Research Letters*, vol. 3, no. 3, pp. 137–140, 1976.

[149] D. A. Guidice, E. W. Cliver, W. R. Barron *et al.*, “The Air Force RSTN System,” in *Bulletin of the American Astronomical Society*, vol. 13, Mar. 1981, p. 553.

[150] T. Kondo, T. Isobe, S. Igi *et al.*, “The New Solar Radio Observation System At Hiraiso,” *Communications Research Laboratory Review*, vol. 40, p. 85, Mar. 1994.

[151] C. Caroubalos, D. Maroulis, N. Patavalis *et al.*, “The New Multichannel Radiospectrograph ARTEMIS-IV/HECATE, of the University of Athens,” *Experimental Astronomy*, vol. 11, no. 1, pp. 23–32, Feb. 2001.

[152] R. V. Gorgutsa, A. A. Gnezdilov, A. K. Markeev *et al.*, “An upgrade of the izmiran’s solar digital radio spectrograph: First results,” *Astronomical and Astrophysical Transactions*, vol. 20, no. 3, pp. 547–549, Oct. 2001.

[153] P. Kishore, C. Kathiravan, R. Ramesh *et al.*, “Gauribidanur Low-Frequency Solar Spectrograph,” *Sol. Phys.*, vol. 289, no. 10, pp. 3995–4005, Oct. 2014.

[154] A. Boischot, C. Rosolen, M. G. Aubier *et al.*, “A new high-grain, broadband, steerable array to study Jovian decametric emission,” *Icarus*, vol. 43, no. 3, pp. 399–407, Sep. 1980.

[155] S. I. Braude, A. V. Men, and L. G. Sodin, “The UTR-2 decametric-wave radio telescope,” *Antenny*, vol. 26, pp. 3–15, Jan. 1978.

[156] S. Y. Braude, “Decametric radioastronomy.” in *Astrophysics on the Threshold of the 21st Century*, N. S. Kardashev, Ed., 1992, pp. 81–102.

[157] S. Y. Braude, A. V. Megn, S. L. Rashkovsky *et al.*, “The Ukrainian radio interferometer system URAN for studies in decametric wavelengths band (Abstract),” in *Planetary Radio Emissions III*, H. O. Rucker, S. J. Bauer, and M. L. Kaiser, Eds., Jan. 1992, p. 183.

[158] A. V. Megn, S. Y. Braude, S. L. Rashkovskiy *et al.*, “URAN System of the Decametric Interferometers (I),” *Radio Physics and Radio Astronomy*, vol. 2, p. 385, Dec. 1997.

[159] J. L. Bougeret, M. L. Kaiser, P. J. Kellogg *et al.*, “Waves: The Radio and Plasma Wave Investigation on the Wind Spacecraft,” *Space Sci. Rev.*, vol. 71, no. 1-4, pp. 231–263, Feb. 1995.

[160] H. Salmane, R. Weber, K. Abed-Meraim *et al.*, “A method for the automated detection of solar radio bursts in dynamic spectra,” *Journal of Space Weather and Space Climate*, vol. 8, p. A43, Oct. 2018.

[161] D. B. Melrose and G. A. Dulk, “Electron-cyclotron masers as the source of certain solar and stellar radio bursts.” *ApJ*, vol. 259, pp. 844–858, Aug. 1982.

[162] D. B. Melrose, *Plasma astrohysics. Nonthermal processes in diffuse magnetized plasmas - Vol.1: The emission, absorption and transfer of waves in plasmas; Vol.2: Astrophysical applications*. New York: Gordon and Breach, 1980.

[163] V. N. Tsytovich and D. ter Haar, *Lectures on Non-linear Plasma Kinetics*, 1995.

[164] P. A. Robinson, I. H. Cairns, and A. J. Willes, “Dynamics and Efficiency of Type III Solar Radio Emission,” *ApJ*, vol. 422, p. 870, Feb. 1994.

[165] D. B. Melrose, “Coherent emission,” in *Universal Heliophysical Processes*, N. Gopalswamy and D. F. Webb, Eds., vol. 257, Mar. 2009, pp. 305–315.

[166] D. Tsiklauri, “An alternative to the plasma emission model: Particle-in-cell, self-consistent electromagnetic wave emission simulations of solar type III radio bursts,” *Physics of Plasmas*, vol. 18, no. 5, pp. 052 903–052 903, May 2011.

[167] A. Warmuth and G. Mann, “The Application of Radio Diagnostics to the Study of the Solar Drivers of Space Weather,” in *Lecture Notes in Physics, Berlin Springer Verlag*, K. Scherer, H. Fichter, and B. Herber, Eds., 2004, vol. 656, p. 49.

[168] G. Mann, “2.2 solar radio telescopes: Datasheet from landolt-börnstein - group vi astronomy and astrophysics · volume 4a: “instruments and methods” in springermaterials,” 2010, copyright 2010 Springer-Verlag Berlin Heidelberg.

[169] A. Krueger, *Introduction to solar radio astronomy and radio physics*, 1979.

[170] V. V. Zheleznyakov, *Radio emission of the sun and planets*. Oxford: Pergamon Press, 1970.

[171] G. Befki, *Radiation processes in plasmas*. Wiley Series in Plasma Physics, New York: Wiley, 1966.

[172] A. O. Benz, *Plasma astrophysics: Kinetic processes in solar and stellar coronae*. Kluwer Academic Publishers, Dordrecht, 1993, vol. 184.

[173] S. A. Kaplan and V. N. Tsytovich, *Plasma astrophysics*. International Series of Monographs in Natural Philosophy, Oxford: Pergamon Press, 1973.

[174] D. B. Melrose, *Instabilities in Space and Laboratory Plasmas*. Cambridge, UK: Cambridge University Press, 1986.

[175] G. B. Rybicki and A. P. Lightman, *Radiative processes in astrophysics*, 1979.

[176] V. V. Zheleznyakov, *Radiation in Astrophysical Plasmas*. Astrophysics & Space Science Library, 1996, vol. 204.

[177] J. P. Wild and L. L. McCready, "Observations of the Spectrum of High-Intensity Solar Radiation at Metre Wavelengths. I. The Apparatus and Spectral Types of Solar Burst Observed," *Australian Journal of Scientific Research A Physical Sciences*, vol. 3, p. 387, Sep. 1950.

[178] A. Boischot, "Caractères d'un type d'émission hertzienne associé à certaines éruptions chromosphériques," *Academie des Sciences Paris Comptes Rendus*, vol. 244, pp. 1326–1329, Jan. 1957.

[179] J. P. Wild, K. V. Sheridan, and G. H. Trent, "The transverse motions of the sources of solar radio bursts," in *URSI Symp. 1: Paris Symposium on Radio Astronomy*, R. N. Bracewell, Ed., vol. 9, Jan. 1959, p. 176.

[180] J. P. Wild, S. F. Smerd, and A. A. Weiss, "Solar Bursts," *Ann. Rev. Astron and Astrophys.*, vol. 1, p. 291, Jan. 1963.

[181] D. B. Melrose, "A Plasma Emission Mechanism for Type-I Solar Radio Emission," *Sol. Phys.*, vol. 67, no. 2, pp. 357–375, Aug. 1980.

[182] M. R. Kundu and T. E. Gergely, "Radio physics of the sun: proceedings from IAU symposium no. 86, held in College Park, Md. U.S.A., August 7-10, 1979." in *Radio Physics of the Sun*, vol. 86, Jan. 1980.

[183] E. Ø. Elgarøy, *Solar noise storms.*, 1977.

[184] R. Payne-Scott, D. E. Yabsley, and J. G. Bolton, "Relative Times of Arrival of Bursts of Solar Noise on Different Radio Frequencies," *Nature*, vol. 160, no. 4060, pp. 256–257, Aug. 1947.

[185] D. Maia, M. Pick, A. Vourlidas *et al.*, "Development of coronal mass ejections: Radio shock signatures," *The Astrophysical Journal*, vol. 528, no. 1, pp. L49–L51, jan 2000.

[186] M. Pick, T. G. Forbes, G. Mann *et al.*, "Multi-Wavelength Observations of CMEs and Associated Phenomena. Report of Working Group F," *Space Sci. Rev.*, vol. 123, no. 1-3, pp. 341–382, Mar. 2006.

[187] M. Temmer, A. M. Veronig, E. P. Kontar *et al.*, "Combined stereo/rhessi study of coronal mass ejections acceleration and particle acceleration in solar flares," *The Astrophysical Journal*, vol. 712, no. 2, pp. 1410–1420, mar 2010.

[188] V. V. Grechnev, A. N. Afanasyev, A. M. Uralov *et al.*, "Coronal Shock Waves, EUV Waves, and Their Relation to CMEs. III. Shock-Associated CME/EUV Wave in an Event with a Two-Component EUV Transient," *Sol. Phys.*, vol. 273, no. 2, pp. 461–477, Nov. 2011.

[189] V. Vasanth, S. Umapathy, B. Vršnak *et al.*, "Characteristics of Type-II Radio Bursts Associated with Flares and CMEs," *Sol. Phys.*, vol. 273, no. 1, pp. 143–162, Oct. 2011.

[190] N. Gopalswamy, S. Yashiro, P. Mäkelä *et al.*, "Extreme kinematics of the 2017 september 10 solar eruption and the spectral characteristics of the associated energetic particles," *The Astrophysical Journal*, vol. 863, no. 2, p. L39, aug 2018.

[191] G. Chernov and V. Fomichev, "On the Issue of the Origin of Type II Solar Radio Bursts," *ApJ*, vol. 922, no. 1, p. 82, Nov. 2021.

[192] Y. Uchida, "On the Exciters of Type II and Type III Solar Radio Bursts," *Pub. Astron Society Japan*, vol. 12, p. 376, Jan. 1960.

[193] G. J. Nelson and D. B. Melrose, "Type II bursts." in *Solar Radiophysics: Studies of Emission from the Sun at Metre Wavelengths*, D. J. McLean and N. R. Labrum, Eds., 1985, pp. 333–359.

[194] N. Gopalswamy, E. Aguilar-Rodriguez, S. Yashiro *et al.*, "Type II radio bursts and energetic solar eruptions," *Journal of Geophysical Research (Space Physics)*, vol. 110, no. A12, p. A12S07, Dec. 2005.

[195] H. V. Cane, J. Sheeley, N. R., and R. A. Howard, "Energetic interpanetary shocks, radio emission, and coronal mass ejections," *J Geophys. Res.*, vol. 92, no. A9, pp. 9869–9874, Sep. 1987.

[196] M. J. Reiner, M. L. Kaiser, J. Fainberg *et al.*, "On the origin of radio emissions associated with the January 6-11, 1997, CME," *Geophys. Res. Lett.*, vol. 25, no. 14, pp. 2493–2496, Jul. 1998.

[197] M. L. Kaiser, M. J. Reiner, N. Gopalswamy *et al.*, "Type II radio emissions in the frequency range from 1-14 MHz associated with the April 7, 1997 solar event," *Geophys. Res. Lett.*, vol. 25, no. 14, pp. 2501–2504, Jul. 1998.

[198] N. Gopalswamy, S. Yashiro, S. Krucker *et al.*, "Intensity variation of large solar energetic particle events associated with coronal mass ejections," *Journal of Geophysical Research (Space Physics)*, vol. 109, no. A12, p. A12105, Dec. 2004.

[199] N. Gopalswamy, M. L. Kaiser, R. P. Lepping *et al.*, "Origin of coronal and interplanetary shocks: A new look with WIND spacecraft data," *J Geophys. Res.*, vol. 103, no. A1, pp. 307–316, Jan. 1998.

[200] E. W. Cliver, D. F. Webb, and R. A. Howard, "On the origin of solar metric type II bursts," *Sol. Phys.*, vol. 187, no. 1, pp. 89–114, Jun. 1999.

[201] B. Vršnak and E. W. Cliver, "Origin of Coronal Shock Waves. Invited Review," *Sol. Phys.*, vol. 253, no. 1-2, p. 215, Dec. 2008.

[202] J. Sheeley, N. R., R. A. Howard, D. J. Michels *et al.*, "Associations between coronal mass ejections and metric type II bursts," *ApJ*, vol. 279, pp. 839–847, Apr. 1984.

[203] B. Vršnak, "Solar flares and coronal shock waves," *J Geophys. Res.*, vol. 106, no. A11, pp. 25 291–25 300, Nov. 2001.

[204] A. Umuhire, J. Uwamahoro, K. Sasikumar Raja *et al.*, "Trends and characteristics of high-frequency type ii bursts detected by callisto spectrometers," *Advances in Space Research*, vol. 68, no. 8, pp. 3464–3477, 2021.

[205] J. Sheeley, N. R., R. A. Howard, D. J. Michels *et al.*, "Coronal mass ejections and interplanetary shocks," *J Geophys. Res.*, vol. 90, no. A1, pp. 163–176, Jan. 1985.

[206] S. D. Bale, M. J. Reiner, J. L. Bougeret *et al.*, "The source region of an interplanetary type II radio burst," *Geophys. Res. Lett.*, vol. 26, no. 11, pp. 1573–1576, Jun. 1999.

[207] N. Gopalswamy, M. L. Kaiser, B. J. Thompson *et al.*, "Radio-rich solar eruptive events," *Geophys. Res. Lett.*, vol. 27, no. 10, pp. 1427–1430, May 2000.

[208] A. Lara, N. Gopalswamy, S. Nunes *et al.*, "A statistical study of CMEs associated with metric type II bursts," *Geophys. Res. Lett.*, vol. 30, no. 12, p. 8016, Jun. 2003.

[209] A. Shanmugaraju, Y. J. Moon, M. Dryer *et al.*, "Statistical Characteristics of CMEs and Flares Associated with Solar Type II Radio Bursts," *Sol. Phys.*, vol. 217, no. 2, pp. 301–317, Nov. 2003.

[210] M. J. Reiner, M. L. Kaiser, N. Gopalswamy *et al.*, "Statistical analysis of coronal shock dynamics implied by radio and white-light observations," *J Geophys. Res.*, vol. 106, no. A11, pp. 25 279–25 290, Nov. 2001.

[211] S. Pohjolainen, H. Allawi, and E. Valtonen, "Origin of wide-band IP type II bursts," *A&A*, vol. 558, p. A7, Oct. 2013.

[212] R. D. Robinson and K. V. Sheridan, "A study of multiple type II solar radio events," *Publ. Astron. Soc. Pac.*, vol. 4, no. 4, pp. 392–396, Jan. 1982.

[213] S. F. Smerd, K. V. Sheridan, and R. T. Stewart, "On Split-Band Structure in Type II Radio Bursts from the Sun (presented by S.F. Smerd)," in *Coronal Disturbances*, G. A. Newkirk, Ed., vol. 57, Jan. 1974, p. 389.

[214] G. J. Nelson and R. D. Robinson, "Multi-Frequency Heliograph Observations of Type II Bursts," *Proc. Astron. Soc. Australia.*, vol. 2, p. 370, Oct. 1975.

[215] I. Zimovets, N. Vilmer, A. C. L. Chian *et al.*, "Spatially resolved observations of a split-band coronal type II radio burst," *A&A*, vol. 547, p. A6, Nov. 2012.

[216] P. Zucca, M. Pick, P. Démoulin *et al.*, "Understanding Coronal Mass Ejections and Associated Shocks in the Solar Corona by Merging Multiwavelength Observations," *ApJ*, vol. 795, no. 1, p. 68, Nov. 2014.

[217] E. Aguilar-Rodriguez, N. Gopalswamy, R. MacDowall *et al.*, "A Study of the Drift Rate of Type II Radio Bursts at Different Wavelengths," in *Solar Wind 11/SOHO 16, Connecting Sun and Heliosphere*, ser. ESA Special Publication, B. Fleck, T. H. Zurbuchen, and H. Lacoste, Eds., vol. 592, Sep. 2005, p. 393.

[218] G. Mann and A. Klassen, "Electron beams generated by shock waves in the solar corona," *A&A*, vol. 441, no. 1, pp. 319–326, Oct. 2005.

[219] N. Gopalswamy, "Coronal Mass Ejections and Type II Radio Bursts," *Geophysical Monograph Series*, vol. 165, p. 207, Oct. 2006.

[220] K. Saito, A. I. Poland, and R. H. Munro, "A study of the background corona near solar minimum." *Sol. Phys.*, vol. 55, no. 1, pp. 121–134, Nov. 1977.

[221] Y. Leblanc, G. A. Dulk, and J.-L. Bougeret, "Tracing the Electron Density from the Corona to 1au," *Sol. Phys.*, vol. 183, no. 1, pp. 165–180, Nov. 1998.

[222] N. Gopalswamy, P. Mäkelä, H. Xie *et al.*, "CME interactions with coronal holes and their interplanetary consequences," *Journal of Geophysical Research (Space Physics)*, vol. 114, no. A3, p. A00A22, Mar. 2009.

[223] J. Newkirk, Gordon, "The Solar Corona in Active Regions and the Thermal Origin of the Slowly Varying Component of Solar Radio Radiation." *ApJ*, vol. 133, p. 983, May 1961.

[224] S. Koutchmy, "Coronal physics from eclipse observations," *Advances in Space Research*, vol. 14, no. 4, pp. 29–39, apr 1994.

[225] G. Mann, T. Classen, and H. Aurass, "Characteristics of coronal shock waves and solar type II radio bursts." *A&A*, vol. 295, p. 775, Mar. 1995.

[226] G. Mann, A. Klassen, H. T. Classen *et al.*, "Catalogue of solar type II radio bursts observed from September 1990 to December 1993 and their statistical analysis." *A&AS*, vol. 119, pp. 489–498, Nov. 1996.

[227] B. Vršnak, H. Aurass, J. Magdalenić *et al.*, "Band-splitting of coronal and interplanetary type II bursts. I. Basic properties," *A & A*, vol. 377, pp. 321–329, Oct. 2001.

[228] B. Vršnak, J. Magdalenić, H. Aurass *et al.*, “Band-splitting of coronal and interplanetary type II bursts. II. Coronal magnetic field and Alfvén velocity,” *A & A*, vol. 396, pp. 673–682, Dec. 2002.

[229] B. Vršnak, J. Magdalenić, and P. Zlobec, “Band-splitting of coronal and interplanetary type II bursts. III. Physical conditions in the upper corona and interplanetary space,” *A&A*, vol. 413, pp. 753–763, Jan. 2004.

[230] M. Nedal, A. Mahrous, and M. Youssef, “Predicting the arrival time of CME associated with type-II radio burst using neural networks technique,” *Ap & Space Sci.*, vol. 364, no. 9, p. 161, Sep. 2019.

[231] S. Lata Soni, E. Ebenezer, and M. lal Yadav, “Multi-wavelength analysis of CME-driven shock and Type II solar radio burst band-splitting,” *Astrophys Space Sci*, vol. 366, no. 3, p. 31, Mar. 2021.

[232] H. A. S. Reid and H. Ratcliffe, “A review of solar type III radio bursts,” *Research in Astronomy and Astrophysics*, vol. 14, no. 7, pp. 773–804, Jul. 2014.

[233] T. Ndacyayisenga, J. Uwamahoro, K. Sasikumar Raja *et al.*, “A statistical study of solar radio Type III bursts and space weather implication,” *Advances in Space Research*, vol. 67, no. 4, pp. 1425–1435, Feb. 2021.

[234] A. O. Benz, A. Magun, W. Stehling *et al.*, “Electron Beams in the Low Corona,” *Sol. Phys.*, vol. 141, no. 2, pp. 335–346, Oct. 1992.

[235] R. D. Robinson, “A study of solar flare continuum events observed at metre wavelengths.” *Australian Journal of Physics*, vol. 31, pp. 533–545, Dec. 1978.

[236] R. M. Winglee and G. A. Dulk, “The Electron-Cyclotron Maser Instability as a Source of Plasma Radiation,” *ApJ*, vol. 307, p. 808, Aug. 1986.

[237] M. R. Kundu, “Some Aspects of the Type-IV Continuum Radiation on Decimeter Wavelengths,” in *The Solar Spectrum*, ser. Astrophysics and Space Science Library, C. de Jager, Ed., vol. 1, Jan. 1965, p. 408.

[238] H. Aurass, K. L. Klein, E. Y. Zlotnik *et al.*, “Solar type IV burst spectral fine structures . I. Observations,” *A&A*, vol. 410, pp. 1001–1010, Nov. 2003.

[239] E. Y. Zlotnik, V. V. Zaitsev, H. Aurass *et al.*, “Solar type IV burst spectral fine structures. II. Source model,” *A&A*, vol. 410, pp. 1011–1022, Nov. 2003.

[240] J. P. Wild and S. F. Smerd, “Radio Bursts from the Solar Corona,” *Ann. Rev. As. Astrophys.*, vol. 10, p. 159, Jan. 1972.

[241] R. T. Stewart, “Moving type IV bursts.” in *Solar Radiophysics: Studies of Emission from the Sun at Metre Wavelengths*, D. J. McLean and N. R. Labrum, Eds., 1985, pp. 361–383.

[242] T. S. Bastian, M. Pick, A. Kerdraon *et al.*, “The Coronal Mass Ejection of 1998 April 20: Direct Imaging at Radio Wavelengths,” *ApJ Let.*, vol. 558, no. 1, pp. L65–L69, Sep. 2001.

[243] E. P. Carley, N. Vilmer, P. J. A. Simões *et al.*, “Estimation of a coronal mass ejection magnetic field strength using radio observations of gyrosynchrotron radiation,” *A&A*, vol. 608, p. A137, Dec. 2017.

[244] R. Ramesh, P. Kishore, S. M. Mulay *et al.*, “Low-frequency Observations of Drifting, Non-thermal Continuum Radio Emission Associated with the Solar Coronal Mass Ejections,” *ApJ*, vol. 778, no. 1, p. 30, Nov. 2013.

[245] K. Hariharan, R. Ramesh, C. Kathiravan *et al.*, “Simultaneous Near-Sun Observations of a Moving Type IV Radio Burst and the Associated White-Light Coronal Mass Ejection,” *Sol. Phys.*, vol. 291, no. 5, pp. 1405–1416, May 2016.

[246] V. Vasanth, Y. Chen, S. Feng *et al.*, “An Eruptive Hot-channel Structure Observed at Metric Wavelength as a Moving Type-IV Solar Radio Burst,” *ApJ Lett.*, vol. 830, no. 1, p. L2, Oct. 2016.

[247] H. Liu, Y. Chen, K. Cho *et al.*, “A Solar Stationary Type IV Radio Burst and Its Radiation Mechanism,” *Sol. Phys.*, vol. 293, no. 4, p. 58, Apr. 2018.

[248] J. F. Tang, D. J. Wu, and C. M. Tan, “Electron Cyclotron Maser Emission in Coronal Arches and Solar Radio Type V Bursts,” *ApJ*, vol. 779, no. 1, p. 83, Dec. 2013.

[249] R. B. Langley, *Propagation of the GPS Signals*. Berlin, Heidelberg: Springer Berlin Heidelberg, 1998, pp. 111–149.

[250] T. F. Tascione, *Introduction to the Space Environment.*, 2nd ed. Krieger Publishing Company, Malabar, Florida., 1994.

[251] P. Mukhtarov, B. Andonov, and D. Pancheva, “Global empirical model of tec response to geomagnetic activity,” *Journal of Geophysical Research: Space Physics*, vol. 118, no. 10, pp. 6666–6685, 2013.

[252] K. Davies, *Ionospheric Radio*, ser. Electromagnetics and Radar Series. Peregrinus, 1990.

[253] T. Bosinger, J. Labelle, H. J. Opgenoorth *et al.*, *Dynamic Coupling between Earth’s Atmospheric and Plasma Environments*. Springer, 2013.

[254] G. Lu, X. Pi, A. D. Richmond *et al.*, “Correction to “Variations of total electron content during geomagnetic disturbances: A model/observation comparison”,” *Geophys. Res. Lett.*, vol. 25, no. 16, pp. 3107–3107, Aug. 1998.

[255] P. K. Bhuyan and R. R. Borah, "TEC derived from GPS network in India and comparison with the IRI," *Advances in Space Research*, vol. 39, no. 5, pp. 830–840, Jan. 2007.

[256] A. P. Cerruti, P. M. Kintner, D. Gary *et al.*, "Direct Observations of GPS L1 Signal-to-Noise Degradation due to Solar Radio Bursts," in *AGU Spring Meeting Abstracts*, vol. 2007, May 2006, pp. SH53A–07.

[257] C. S. Carrano, C. T. Bridgwood, and K. M. Groves, "Impacts of the December 2006 solar radio bursts on the performance of GPS," *Radio Science*, vol. 44, p. RS0A25, Aug. 2009.

[258] G. W. Prölss, "Perturbations of the upper atmosphere in the cleft region," *Journal of Atmospheric and Solar-Terrestrial Physics*, vol. 70, no. 18, pp. 2374–2380, Dec. 2008.

[259] C. Borries, J. Berdermann, N. Jakowski *et al.*, "Ionospheric storms—A challenge for empirical forecast of the total electron content," *Journal of Geophysical Research (Space Physics)*, vol. 120, no. 4, pp. 3175–3186, Apr. 2015.

[260] Z. Chen, Y. Gao, and Z. Liu, "Evaluation of solar radio bursts' effect on gps receiver signal tracking within international gps service network," *Radio Science*, vol. 40, no. 3, 2005.

[261] A. P. Cerruti, P. M. Kintner Jr., D. E. Gary *et al.*, "Effect of intense december 2006 solar radio bursts on gps receivers," *Space Weather*, vol. 6, no. 10, 2008.

[262] A. Zawari, M. T. Islam, R. Anwar *et al.*, "Callisto radio spectrometer construction at universiti kebangsaan malaysia [antennas and propagation around the world]," *IEEE Antennas and Propagation Magazine*, vol. 56, no. 2, pp. 278–288, Apr. 2014.

[263] M. O. Ali, S. N. U. Sabri, Z. S. Hamidi *et al.*, "e-callisto network system and the observation of structure of solar radio burst type iii," in *2016 International Conference on Industrial Engineering, Management Science and Application (ICIMSA)*, 2016, pp. 1–5.

[264] M. L. Kaiser, T. A. Kucera, J. M. Davila *et al.*, "The STEREO Mission: An Introduction," *Space Sci. Rev.*, vol. 136, no. 1-4, pp. 5–16, Apr. 2008.

[265] J. L. Bougeret, K. Goetz, M. L. Kaiser *et al.*, "S/WAVES: The Radio and Plasma Wave Investigation on the STEREO Mission," *Space Sci. Rev*, vol. 136, no. 1-4, pp. 487–528, Apr. 2008.

[266] B. Lyot, "The study of the solar corona and prominences without eclipses (George Darwin Lecture, 1939)," *Monthly Notices of the Royal Astronomical Society*, vol. 99, p. 580, Jun. 1939.

[267] J. R. Lemen, A. M. Title, D. J. Akin *et al.*, "The Atmospheric Imaging Assembly (AIA) on the Solar Dynamics Observatory (SDO)," *Sol. Phys.*, vol. 275, no. 1-2, pp. 17–40, Jan. 2012.

[268] D. E. Innes, R. H. Cameron, and S. K. Solanki, “EUV jets, type III radio bursts and sunspot waves investigated using SDO/AIA observations,” *A&A*, vol. 531, p. L13, Jul. 2011.

[269] P. H. Scherrer, J. Schou, R. I. Bush *et al.*, “The Helioseismic and Magnetic Imager (HMI) Investigation for the Solar Dynamics Observatory (SDO),” *Sol. Phys.*, vol. 275, no. 1-2, pp. 207–227, Jan. 2012.

[270] J. Schou, P. H. Scherrer, R. I. Bush *et al.*, “Design and Ground Calibration of the Helioseismic and Magnetic Imager (HMI) Instrument on the Solar Dynamics Observatory (SDO),” *Sol. Phys.*, vol. 275, no. 1-2, pp. 229–259, Jan. 2012.

[271] G. K. Seemala and C. E. Valladares, “Statistics of total electron content depletions observed over the south american continent for the year 2008,” *Radio Science*, vol. 46, no. 5, 2011.

[272] J. C. Uwamahoro, N. M. Giday, J. B. Habarulema *et al.*, “Reconstruction of Storm-Time Total Electron Content Using Ionospheric Tomography and Artificial Neural Networks: A Comparative Study Over the African Region,” *Radio Science*, vol. 53, no. 11, pp. 1328–1345, Nov. 2018.

[273] I. Azzouzi, Y. Migoya-Orué, C. Amory Mazaudier *et al.*, “Signatures of solar event at middle and low latitudes in the Europe-African sector, during geomagnetic storms, October 2013,” *Adv. Space Res.*, vol. 56, no. 9, pp. 2040–2055, Nov. 2015.

[274] X. Liu, Y. Yuan, B. Tan *et al.*, “Observational analysis of variation characteristics of gps-based tec fluctuation over china,” *ISPRS International Journal of Geo-Information*, vol. 5, no. 12, 2016.

[275] T. Dugassa, J. B. Habarulema, and M. Nigussie, “Equatorial and low-latitude ionospheric TEC response to CIR-driven geomagnetic storms at different longitude sectors,” *Adv. Space Res.*, vol. 66, no. 8, pp. 1947–1966, Oct. 2020.

[276] V. Habyarimana, J. B. Habarulema, D. Okoh *et al.*, “Single station modelling of ionospheric irregularities using artificial neural networks,” *Astrophysics and Space Science*, vol. 368, no. 12, p. 105, Dec. 2023.

[277] D. Okoh, “Programs to compute rot and roti (https://www.mathworks.com/matlabcentral/fileexchange/1 programs-to-compute-rot-and-roti),” May 2025.

[278] W. Dieminger, G. K. Hartmann, and R. Leitinger, *Geomagnetic Activity Indices*. Berlin, Heidelberg: Springer Berlin Heidelberg, 1996, pp. 887–911.

[279] G. K. Rangarajan, “Indices of geomagnetic activity.” *Geomatik*, vol. 3, pp. 323–384, Jan. 1989.

[280] A. Berthelier, “The Geomagnetic Indices: Derivation, Meaning and Uses in Solar-Terrestrial Physics,” in *Solar-Terrestrial Predictions – IV, Volume 3*, vol. 3, Jan. 1993, p. 3.

[281] M. Menvielle and A. Berthelier, “The K-derived planetary indices - Description and availability,” *Reviews of Geophysics*, vol. 29, pp. 415–432, Aug. 1991.

[282] M. Sugiura, A. Berthelier, and et al., *Equatorial Dst Index, 1957-1986.*, 1991.

[283] J. A. Wanliss and K. M. Showalter, “High-resolution global storm index: Dst versus SYM-H,” *Journal of Geophysical Research (Space Physics)*, vol. 111, no. A2, p. A02202, Feb. 2006.

[284] G. Vichare, N. Thomas, K. Shiokawa *et al.*, “Spatial Gradients in Geomagnetic Storm Time Currents Observed by Swarm Multispacecraft Mission,” *Journal of Geophysical Research (Space Physics)*, vol. 124, no. 2, pp. 982–995, Feb. 2019.

[285] S. I. Akasofu, “Energy coupling between the solar wind and the magnetosphere.” *Space Sci. Rev.*, vol. 28, no. 2, pp. 121–190, Jun. 1981.

[286] G. Lu, D. N. Baker, R. L. McPherron *et al.*, “Global energy deposition during the january 1997 magnetic cloud event,” *Journal of Geophysical Research: Space Physics*, vol. 103, no. A6, pp. 11 685–11 694, 1998.

[287] N. Østgaard, R. R. Vondrak, J. W. Gjerloev *et al.*, “A relation between the energy deposition by electron precipitation and geomagnetic indices during substorms,” *Journal of Geophysical Research: Space Physics*, vol. 107, no. A9, pp. SMP 16–1–SMP 16–7, 2002.

[288] N. E. Turner, W. D. Cramer, S. K. Earles *et al.*, “Geoefficiency and energy partitioning in cir-driven and cme-driven storms,” *Journal of Atmospheric and Solar-Terrestrial Physics*, vol. 71, no. 10, pp. 1023–1031, 2009.

[289] D. Boteler, R. Pirjola, and H. Nevanlinna, “The effects of geomagnetic disturbances on electrical systems at the earth’s surface,” *Advances in Space Research*, vol. 22, no. 1, pp. 17–27, 1998.

[290] R. Pirjola, A. Viljanen, A. Pulkkinen *et al.*, “Space weather risk in power systems and pipelines,” *Physics and Chemistry of the Earth, Part C: Solar, Terrestrial & Planetary Science*, vol. 25, no. 4, pp. 333–337, 2000.

[291] E. J. Oughton, A. Skelton, R. B. Horne *et al.*, “Quantifying the daily economic impact of extreme space weather due to failure in electricity transmission infrastructure,” *Space Weather*, vol. 15, no. 1, pp. 65–83, 2017.

[292] P. Riley, D. Baker, Y. D. Liu *et al.*, “Extreme Space Weather Events: From Cradle to Grave,” *Space Sci. Rev.*, vol. 214, no. 1, p. 21, Feb. 2018.

[293] J. R. Kan and L. C. Lee, “Energy coupling function and solar wind-magnetosphere dynamo,” *Geophysical Research Letters*, vol. 6, no. 7, pp. 577–580, 1979.

[294] V. M. Vasyliunas, J. R. Kan, G. L. Siscoe *et al.*, “Scaling relations governing magnetospheric energy transfer,” *Planetary and Space Science*, vol. 30, no. 4, pp. 359–365, 1982.

[295] W. Gonzalez, “A unified view of solar wind-magnetosphere coupling functions,” *Planetary and Space Science*, vol. 38, no. 5, pp. 627–632, 1990.

[296] P. T. Newell, T. Sotirelis, K. Liou *et al.*, “A nearly universal solar wind-magnetosphere coupling function inferred from 10 magnetospheric state variables,” *Journal of Geophysical Research (Space Physics)*, vol. 112, no. A1, p. A01206, Jan. 2007.

[297] P. Tenfjord and N. Østgaard, “Energy transfer and flow in the solar wind-magnetosphere-ionosphere system: A new coupling function,” *Journal of Geophysical Research (Space Physics)*, vol. 118, no. 9, pp. 5659–5672, Sep. 2013.

[298] C. Wang, J. P. Han, H. Li *et al.*, “Solar wind-magnetosphere energy coupling function fitting: Results from a global MHD simulation,” *Journal of Geophysical Research (Space Physics)*, vol. 119, no. 8, pp. 6199–6212, Aug. 2014.

[299] R. L. McPherron, T.-S. Hsu, and X. Chu, “An optimum solar wind coupling function for the AL index,” *Journal of Geophysical Research (Space Physics)*, vol. 120, no. 4, pp. 2494–2515, Apr. 2015.

[300] P. Perreault and S. I. Akasofu, “A study of geomagnetic storms.” *Geophysical Journal*, vol. 54, pp. 547–573, Sep. 1978.

[301] T. Aoki, “On the validity of Akasofu’s e parameter and of the Vasyliunas et al. general formula for the rate of solar wind-magnetosphere energy input,” *Earth, Planets and Space*, vol. 57, pp. 131–137, Feb. 2005.

[302] E. W. Grimes, N. Hatzigeorgiu, J. W. Lewis *et al.*, “pySPEDAS: Space Physics Environment Data Analysis Software in Python,” in *AGU Fall Meeting Abstracts*, vol. 2019, Dec. 2019, pp. SH41C–3313.

[303] J. Torsti, E. Valtonen, M. Lumme *et al.*, “Energetic Particle Experiment ERNE,” *Sol. Phys*, vol. 162, no. 1-2, pp. 505–531, Dec. 1995.

[304] A. Kouloumvakos, A. Nindos, E. Valtonen *et al.*, “Properties of solar energetic particle events inferred from their associated radio emission,” *A&A*, vol. 580, p. A80, Aug. 2015.

[305] D. Ameri, E. Valtonen, and S. Pohjolainen, “Properties of High-Energy Solar Particle Events Associated with Solar Radio Emissions,” *Sol. Phys.*, vol. 294, no. 9, p. 122, Sep. 2019.

[306] R. Vainio, E. Valtonen, B. Heber *et al.*, “The first SEPServer event catalogue ~68-MeV solar proton events observed at 1 AU in 1996-2010,” *Journal of Space Weather and Space Climate*, vol. 3, p. A12, Mar. 2013.

[307] SILSO World Data Center, "The International Sunspot Number," *International Sunspot Number Monthly Bulletin and online catalogue*, 2024.

[308] T. Ndacyayisenga, J. Uwamahoro, J. C. Uwamahoro *et al.*, "Low-frequency solar radio type ii bursts and their association with space weather events during the ascending phase of solar cycle 25," *Annales Geophysicae*, vol. 42, no. 2, pp. 313–329, 2024.

[309] T. Ndacyayisenga, J. Uwamahoro, K. Sasikumar Raja *et al.*, "An assessment of solar cycle 25 progress through observation of srbs and associated geomagnetic storms," *Advances in Space Research*, vol. 73, no. 12, pp. 6274–6287, 2024.

[310] T. Ndacyayisenga, J. Uwamahoro, J. C. Uwamahoro *et al.*, "Large solar energetic particles and solar radio emissions during cycle 25. a comparative analysis of trends and characteristics with cycles 23 and 24," *Advances in Space Research*, vol. 75, no. 1, pp. 1415–1427, 2024.

[311] J. L. Bougeret and M. Pick, "Solar Radio Emissions," in *Handbook of the Solar-Terrestrial Environment*, Y. Kamide and A. C. L. Chian, Eds., 2007, pp. 133 – 151.

[312] M. J. Aschwanden, *Physics of the Solar Corona. An Introduction with Problems and Solutions (2nd edition).* Praxis Publishing Ltd., Chichester, UK; Springer, New York, Berlin, 2005.

[313] V. N. Mel'nik, A. A. Konovalenko, E. P. Abranin *et al.*, "Solar sporadic radio emission in the decametre waveband," *Astronomical and Astrophysical Transactions*, vol. 24, no. 5, pp. 391–401, Oct. 2005.

[314] M. R. Kundu and L. Vlahos, "Solar microwave bursts — A review," *Space Sci. Rev.*, vol. 32, no. 4, pp. 405–462, Dec. 1982.

[315] A. Kerdraon, M. Pick, G. Trottet *et al.*, "The association of radio noise storm enhancements with the appearance of additional material in the corona," *ApJ Lett.*, vol. 265, pp. L19–L21, Feb. 1983.

[316] I. H. Cairns, S. A. Knock, P. A. Robinson *et al.*, "Type II Solar Radio Bursts: Theory and Space Weather Implications," *Space Sci. Rev.*, vol. 107, no. 1, pp. 27–34, Apr. 2003.

[317] D. E. Morosan, E. P. Carley, L. A. Hayes *et al.*, "Multiple regions of shock-accelerated particles during a solar coronal mass ejection," *Nature Astronomy*, vol. 3, pp. 452–461, Feb. 2019.

[318] D. E. Morosan, A. Kumari, E. K. J. Kilpua *et al.*, "Moving solar radio bursts and their association with coronal mass ejections," *A&A*, vol. 647, p. L12, Mar. 2021.

[319] J. T. Gosling, "The solar flare myth," *J Geophys. Res.*, vol. 98, no. A11, pp. 18 937–18 950, Nov. 1993.

[320] D. V. Reames, “Particle acceleration at the Sun and in the heliosphere,” *Space Sci. Rev.*, vol. 90, pp. 413–491, Oct. 1999.

[321] H. V. Cane, R. E. McGuire, and T. T. von Rosenvinge, “Two Classes of Solar Energetic Particle Events Associated with Impulsive and Long-Duration Soft X-Ray Flares,” *ApJ*, vol. 301, p. 448, Feb. 1986.

[322] D. V. Reames, “The Two Sources of Solar Energetic Particles,” *Space Sci. Rev.*, vol. 175, no. 1-4, pp. 53–92, Jun. 2013.

[323] D. V. Reames, “Four Distinct Pathways to the Element Abundances in Solar Energetic Particles,” *Space Sci. Rev.*, vol. 216, no. 2, p. 20, Feb. 2020.

[324] H. V. Cane, W. C. Erickson, and N. P. Prestage, “Solar flares, type III radio bursts, coronal mass ejections, and energetic particles,” *Journal of Geophysical Research (Space Physics)*, vol. 107, no. A10, p. 1315, Oct. 2002.

[325] R. Bučík, “^{3}He-Rich Solar Energetic Particles: Solar Sources,” *Space Sci. Rev.*, vol. 216, no. 2, p. 24, Mar. 2020.

[326] S. W. Kahler, “Radio burst characteristics of solar proton flares,” *ApJ*, vol. 261, pp. 710–719, Oct. 1982.

[327] I. M. Chertok, “On the correlation between the solar gamma-ray line emission, radio bursts and proton fluxes in the interplanetary space,” *Astronomische Nachrichten*, vol. 311, no. 6, pp. 379–381, Oct. 1990.

[328] R. P. Lin, “The Emission and Propagation of 40 keV Solar Flare Electrons. I: The Relationship of 40 keV Electron to Energetic Proton and Relativistic Electron Emission by the Sun,” *Sol. Phys.*, vol. 12, no. 2, pp. 266–303, May 1970.

[329] Z. Švestka and L. Fritzová-Švestková, “Type II Radio Bursts and Particle Acceleration,” *Sol. Phys.*, vol. 36, no. 2, pp. 417–431, Jun. 1974.

[330] N. Gopalswamy, S. Yashiro, S. Akiyama *et al.*, “Coronal mass ejections, type II radio bursts, and solar energetic particle events in the SOHO era,” *Annales Geophysicae*, vol. 26, no. 10, pp. 3033–3047, Oct. 2008.

[331] E. W. Cliver, S. W. Kahler, and D. V. Reames, “Coronal Shocks and Solar Energetic Proton Events,” *ApJ*, vol. 605, no. 2, pp. 902–910, Apr. 2004.

[332] E. W. Cliver and A. G. Ling, “Low-Frequency Type III Bursts and Solar Energetic Particle Events,” *ApJ*, vol. 690, no. 1, pp. 598–609, Jan. 2009.

[333] N. Gopalswamy, “Solar and geospace connections of energetic particle events,” *Geophys. Res. Lett.*, vol. 30, no. 12, p. 8013, Jun. 2003.

[334] E. W. Cliver and A. G. Ling, “Electrons and Protons in Solar Energetic Particle Events,” *ApJ*, vol. 658, no. 2, pp. 1349–1356, Apr. 2007.

[335] R. Miteva, K. L. Klein, S. W. Samwel *et al.*, “Radio signatures of solar energetic particles during the 23rd solar cycle,” *arXiv: Solar and Stellar Astrophysics*, 2014.

[336] A. Papaioannou, I. Sandberg, A. Anastasiadis *et al.*, “Solar flares, coronal mass ejections and solar energetic particle event characteristics,” *Journal of Space Weather and Space Climate*, vol. 6, p. A42, Dec. 2016.

[337] A. C. Umuhire, N. Gopalswamy, J. Uwamahoro *et al.*, “Properties of High-Frequency Type II Radio Bursts and Their Relation to the Associated Coronal Mass Ejections,” *Sol. Phys.*, vol. 296, no. 1, p. 27, Jan. 2021.

[338] R. D. Cunha-Silva, F. C. R. Fernandes, and C. L. Selhorst, “Solar type II radio bursts associated with CME expansions as shown by EUV waves,” *A& A*, vol. 578, p. A38, Jun. 2015.

[339] F. N. Minta, S. Nozawa, K. Kamen *et al.*, “Assessing the spectral characteristics of band splitting type II radio bursts observed by CALLISTO spectrometers,” *arXiv e-prints*, p. arXiv:2301.13839, Jan. 2023.

[340] N. Gopalswamy, N. Nitta, S. Akiyama *et al.*, “Coronal magnetic field measurement from euv images made by the solar dynamics observatory,” *The Astrophysical Journal*, vol. 744, no. 1, p. 72, dec 2011.

[341] B. Tan, N. Chen, Y.-H. Yang *et al.*, “Solar Fast-drifting Radio Bursts in an X1.3 Flare on 2014 April 25,” *ApJ*, vol. 885, no. 1, p. 90, Nov. 2019.

[342] S. F. Smerd, K. V. Sheridan, and R. T. Stewart, “Split-Band Structure in Type II Radio Bursts from the Sun,” *Astrophys. Lett.*, vol. 16, p. 23, Feb. 1975.

[343] C. E. Navia, M. N. de Oliveira, and C. R. A. Augusto, “The highest geomagnetic storms of the solar cycle observed at ground level,” in *Extreme Weather*, P. J. Sallis, Ed. Rijeka: IntechOpen, 2018, ch. 3.

[344] N. Gopalswamy, S. Akiyama, P. Mäkelä *et al.*, “On the Directivity of Low-Frequency Type IV Radio Bursts,” *arXiv e-prints*, p. arXiv:1605.02223, May 2016.

[345] V. N. Mel’nik, H. O. Rucker, and A. A. Konovalenko, “Solar Type IV Bursts at Frequencies 10-30 MHz,” in *Solar Physics Research Trends*, 2008, pp. 287–325.

[346] A. Vourlidas, L. A. Balmaceda, G. Stenborg *et al.*, “Multi-viewpoint Coronal Mass Ejection Catalog Based on STEREO COR2 Observations,” *ApJ*, vol. 838, no. 2, p. 141, Apr. 2017.

[347] H. E. J. Koskinen and E. I. Tanskanen, “Magnetospheric energy budget and the epsilon parameter,” *Journal of Geophysical Research (Space Physics)*, vol. 107, no. A11, p. 1415, Nov. 2002.

[348] M. Regi, L. Perrone, A. Del Corpo *et al.*, “Space Weather Effects Observed in the Northern Hemisphere during November 2021 Geomagnetic Storm: The Impacts on Plasmasphere, Ionosphere and Thermosphere Systems,” *Remote Sensing*, vol. 14, no. 22, p. 5765, Nov. 2022.

[349] R. T. Stewart and K. V. Sheridan, “Evidence of Type II and Type IV Solar Radio Emission from a Common Flare-Induced Shock Wave,” *Sol. Phys.*, vol. 12, no. 2, pp. 229–239, May 1970.

[350] L. Barnard and M. Lockwood, “A survey of gradual solar energetic particle events,” *Journal of Geophysical Research: Space Physics*, vol. 116, no. A5, 2011.

[351] H. V. Cane, I. G. Richardson, and T. T. von Rosenvinge, “A study of solar energetic particle events of 1997-2006: Their composition and associations,” *Journal of Geophysical Research (Space Physics)*, vol. 115, no. A8, p. A08101, Aug. 2010.

[352] J. Park, Y.-J. Moon, and N. Gopalswamy, “Dependence of solar proton events on their associated activities: Coronal mass ejection parameters,” *Journal of Geophysical Research: Space Physics*, vol. 117, no. A8, 2012.

[353] K.-L. Klein, “Radio astronomical tools for the study of solar energetic particles ii.time-extended acceleration at subrelativistic and relativistic energies,” *Front. Astron. Space Sci*, vol. 7, 2021.

[354] A. Kouloumvakos, R. Y. Kwon, L. Rodríguez-García *et al.*, “The first widespread solar energetic particle event of solar cycle 25 on 2020 November 29. Shock wave properties and the wide distribution of solar energetic particles,” *A&A*, vol. 660, p. A84, Apr. 2022.

[355] K.-L. Klein, “Radio astronomical tools for the study of solar energetic particles I. Correlations and diagnostics of impulsive acceleration and particle propagation,” *Front. Astron. Space Sci*, vol. 7, p. 105, Feb. 2021.

[356] B. Tan, “Multi-timescale solar cycles and the possible implications,” *Astrophysics and Space Science*, vol. 332, no. 1, pp. 65–72, Mar. 2011.

[357] S. W. Kahler, “The correlation between solar energetic particle peak intensities and speeds of coronal mass ejections: Effects of ambient particle intensities and energy spectra,” *Journal of Geophysical Research: Space Physics*, vol. 106, no. A10, pp. 20 947–20 955, 2001.

[358] J. Zhang, N. Temmer, M.and Gopalswamy, O. Malandraki *et al.*, “Earth-affecting solar transients: a review of progresses in solar cycle 24,” *Prog Earth Planet Sci*, vol. 8, p. 56, 2021.

[359] J. Lintunen and R. Vainio, “Solar energetic particle event onset as analyzed from simulated data,” *A&A*, vol. 420, pp. 343–350, Jun. 2004.

[360] S. Kahler and B. R. Ragot, “Near-relativistic Electron c/v Onset Plots,” *ApJ*, vol. 646, no. 1, pp. 634–641, Jul. 2006.

[361] H. Xie, P. Mäkelä, N. Gopalswamy *et al.*, “Energy dependence of SEP electron and proton onset times,” *Journal of Geophysical Research (Space Physics)*, vol. 121, no. 7, pp. 6168–6183, Jul. 2016.

[362] M. Hilchenbach, H. Sierks, B. Klecker *et al.*, “Velocity Dispersion Of Energetic Particles Observed By SOHO/CELIAS/STOF,” in *Solar Wind Ten*, ser. American Institute of Physics Conference Series, M. Velli, R. Bruno, F. Malara *et al.*, Eds., vol. 679, Sep. 2003, pp. 106–109.

[363] C. C. Balch, “Updated verification of the space weather prediction center’s solar energetic particle prediction model,” *Space Weather*, vol. 6, no. 1, 2008.

[364] I. G. Richardson, T. T. von Rosenvinge, H. V. Cane *et al.*, “¿ 25 MeV Proton Events Observed by the High Energy Telescopes on the STEREO A and B Spacecraft and/or at Earth During the First $\sim$ Seven Years of the STEREO Mission,” *Sol. Phys*, vol. 289, no. 8, pp. 3059–3107, Aug. 2014.

[365] K.-L. Klein, S. Musset, N. Vilmer *et al.*, “The relativistic solar particle event on 28 October 2021: Evidence of particle acceleration within and escape from the solar corona,” *A&A*, vol. 663, p. A173, Jul. 2022.

[366] Y. Wang and J. Zhang, “A Comparative Study between Eruptive X-Class Flares Associated with Coronal Mass Ejections and Confined X-Class Flares,” *ApJ*, vol. 665, no. 2, pp. 1428–1438, Aug. 2007.

[367] A. Papaioannou, R. Vainio, O. Raukunen *et al.*, “The probabilistic solar particle event forecasting (PROSPER) model,” *Journal of Space Weather and Space Climate*, vol. 12, p. 24, May 2022.

[368] A. Kouloumvakos, A. Papaioannou, C. O. G. Waterfall *et al.*, “The multi-spacecraft high-energy solar particle event of 28 October 2021,” *A&A*, vol. 682, p. A106, Feb. 2024.

[369] C. Lopate, “Fifty Years of Ground Level Solar Particle Event Observations,” *Geophysical Monograph Series*, vol. 165, p. 283, Oct. 2006.

[370] I. C. Jebaraj, J. Magdalenic, and S. Poedts, “On the fine structures in interplanetary radio emissions,” in *EGU General Assembly Conference Abstracts*, ser. EGU General Assembly Conference Abstracts, May 2020, p. 1025.

[371] T. Laitinen, K. L. Klein, L. Kocharov *et al.*, “Solar energetic particle event and radio bursts associated with the 1996 July 9 flare and coronal mass ejection,” *Astron. Astrophys*, vol. 360, pp. 729–741, Aug. 2000.

[372] M. Pick and N. Vilmer, “Sixty-five years of solar radioastronomy: flares, coronal mass ejections and Sun Earth connection,” *A&A Rev.*, vol. 16, pp. 1–153, Oct. 2008.

[373] R. Schwenn, “Space Weather: The Solar Perspective,” *Living Reviews in Solar Physics*, vol. 3, p. 2, Aug. 2006.

[374] C. A. Maguire, E. P. Carley, J. McCauley *et al.*, “Evolution of the Alfvén Mach number associated with a coronal mass ejection shock,” *A & A*, vol. 633, p. A56, Jan. 2020.

[375] E. P. Carley, B. Cecconi, H. A. Reid *et al.*, “Observations of Shock Propagation through Turbulent Plasma in the Solar Corona,” *ApJ*, vol. 921, no. 1, p. 3, Nov. 2021.

[376] R. Vainio, L. Desorgher, D. Heynderickx *et al.*, “Dynamics of the Earth’s Particle Radiation Environment,” *Space Sci. Rev.*, vol. 147, no. 3-4, pp. 187–231, Nov. 2009.

[377] D. J. Knipp and N. A. Gross, “Understanding Space Weather and the Physics Behind It,” in *AGU Fall Meeting Abstracts*, vol. 2011, Dec. 2011, pp. ED13B–0815.

[378] N. A. Schwadron, J. F. Cooper, M. Desai *et al.*, “Particle Radiation Sources, Propagation and Interactions in Deep Space, at Earth, the Moon, Mars, and Beyond: Examples of Radiation Interactions and Effects,” *Space Sci. Rev*, vol. 212, no. 3-4, pp. 1069–1106, Nov. 2017.

[379] O. E. Malandraki and N. B. Crosby, *Solar Energetic Particles and Space Weather: Science and Applications*. Cham: Springer International Publishing, 2018, pp. 1–26.

[380] T. Pulkkinen, “Space Weather: Terrestrial Perspective,” *Living Reviews in Solar Physics*, vol. 4, no. 1, p. 1, May 2007.

[381] T. Dang, X. Li, B. Luo *et al.*, “Unveiling the space weather during the starlink satellites destruction event on 4 february 2022,” *Space Weather*, vol. 20, no. 8, p. e2022SW003152, 2022.

[382] R. Kataoka, D. Shiota, H. Fujiwara *et al.*, “Unexpected space weather causing the reentry of 38 Starlink satellites in February 2022,” *Journal of Space Weather and Space Climate*, vol. 12, p. 41, Oct. 2022.

[383] C. Amory-Mazaudier, M. Menvielle, J.-J. Curto *et al.*, “Recent Advances in Atmospheric, Solar-Terrestrial Physics and Space Weather From a North-South network of scientists [2006-2016] PART A: TUTORIAL,” *Sun and Geosphere*, vol. 12, pp. 1–19, Dec. 2017.

[384] J. B. Habarulema, M. Tshisaphungo, Z. T. Katamzi-Joseph *et al.*, “Ionospheric response to the m- and x-class solar flares of 28 october 2021 over the african sector,” *Space Weather*, vol. 20, no. 8, p. e2022SW003104, 2022.

[385] H. Ranta, A. Ranta, S. M. Yousef *et al.*, “D-region observations of polar cap absorption events during the EISCAT operation in 1981-1989.” *Journal of Atmospheric and Terrestrial Physics*, vol. 55, no. 4-5, pp. 751–766, Apr. 1993.

[386] A. P. Mitra, *Polar Cap Absorption Events*. Dordrecht: Springer Netherlands, 1974, pp. 252–278.

[387] A. Kavanagh, S. Marple, F. Honary *et al.*, “On solar protons and polar cap absorption: constraints on an empirical relationship,” *Annales Geophysicae*, vol. 22, no. 4, pp. 1133–1147, Apr. 2004.

[388] L. Perrone, L. Alfonsi, V. Romano *et al.*, “Polar cap absorption events of November 2001 at Terra Nova Bay, Antarctica,” *Annales Geophysicae*, vol. 22, no. 5, pp. 1633–1648, May 2004.

[389] M. A. Shea and D. F. Smart, “Solar proton event patterns: the rising portion of five solar cycles,” *Advances in Space Research*, vol. 29, no. 3, pp. 325–330, Jan. 2002.

[390] A. Kumari, R. Ramesh, C. Kathiravan *et al.*, “Direct estimates of the solar coronal magnetic field using contemporaneous extreme-ultraviolet, radio, and white-light observations,” *The Astrophysical Journal*, vol. 881, no. 1, p. 24, aug 2019.

[391] F. B. McDonald, B. J. Teegarden, J. H. Trainor *et al.*, “The interplanetary acceleration of energetic nucleons.” *ApJ Let.*, vol. 203, pp. L149–L154, Feb. 1976.

[392] M. A. I. Van Hollebeke, F. B. McDonald, J. H. Trainor *et al.*, “The radial variation of corotating energetic particle streams in the inner and outer solar system,” *Journal of Geophysical Research: Space Physics*, vol. 83, no. A10, pp. 4723–4731, 1978.

[393] B. T. Tsurutani, O. P. Verkhoglyadova, A. J. Mannucci *et al.*, “A brief review of “solar flare effects” on the ionosphere,” *Radio Science*, vol. 44, no. A5, p. RS0A17, Jul. 2009.

[394] J. Liu, W. Wang, L. Qian *et al.*, “Solar flare effects in the Earth’s magnetosphere,” *Nature Physics*, vol. 17, no. 7, pp. 807–812, Jan. 2021.

[395] J. Liu, L. Qian, A. Maute *et al.*, “Electrodynamical coupling of the geospace system during solar flares,” *Journal of Geophysical Research: Space Physics*, vol. 126, no. 1, p. e2020JA028569, 2021.

[396] R. Oran, B. P. Weiss, M. De Soria Santacruz-Pich *et al.*, “Maximum energies of trapped particles around magnetized planets and small bodies,” *Geophysical Research Letters*, vol. 49, no. 13, p. e2021GL097014.

[397] J. Laštovička, “Effects of geomagnetic storms in the lower ionosphere, middle atmosphere and troposphere,” *Journal of Atmospheric and Terrestrial Physics*, vol. 58, no. 7, pp. 831–843, 1996, geomagnetic Storms: Their Origin, Mechanism and Ionospheric/Atmospheric Effects.

[398] T. J. Fuller-Rowell, M. V. Codrescu, R. G. Roble *et al.*, “How does the thermosphere and ionosphere react to a geomagnetic storm?” *Geophysical Monograph Series*, vol. 98, pp. 203–225, Jan. 1997.

[399] M. J. Buonsanto, “Ionospheric Storms — A Review,” *Space Sci. Rev.*, vol. 88, pp. 563–601, Apr. 1999.

[400] L. F. Chernogor, “Statistical Characteristics of Geomagnetic Storms in the 24th Cycle of Solar Activity,” *Kinematics and Physics of Celestial Bodies*, vol. 37, no. 4, pp. 193–199, Jul. 2021.

[401] D. Lin, W. Wang, V. G. Merkin *et al.*, “Origin of dawnside subauroral polarization streams during major geomagnetic storms,” *AGU Advances*, vol. 3, no. 4, p. e2022AV000708, 2022.

[402] Q. Al Shidi, T. Pulkkinen, G. Toth *et al.*, “A large simulation set of geomagnetic storms—can simulations predict ground magnetometer station observations of magnetic field perturbations?” *Space Weather*, vol. 20, no. 11, p. e2022SW003049, 2022.

[403] C.-T. Hsu and N. M. Pedatella, “Effects of forcing uncertainties on the thermospheric and ionospheric states during geomagnetic storm and quiet periods,” *Space Weather*, vol. 21, no. 4, p. e2022SW003216, 2023.

[404] S. Tulasi Ram, B. Veenadhari, A. P. Dimri *et al.*, “Super-intense geomagnetic storm on 10–11 may 2024: Possible mechanisms and impacts,” *Space Weather*, vol. 22, no. 12, p. e2024SW004126, 2024.

[405] V. Pierrard, T. G. W. Verhulst, J.-M. Chevalier *et al.*, “Effects of the geomagnetic superstorms of 10–11 may 2024 and 7–11 october 2024 on the ionosphere and plasmasphere,” *Atmosphere*, vol. 16, no. 3, 2025.

[406] E. Danilchuk, Y. Yasyukevich, A. Vesnin *et al.*, “Impact of the may 2024 extreme geomagnetic storm on the ionosphere and gnss positioning,” *Remote Sensing*, vol. 17, no. 9, 2025.

[407] J. A. Gonzalez-Esparza, E. Sanchez-Garcia, M. Sergeeva *et al.*, “The mother’s day geomagnetic storm on 10 may 2024: Aurora observations and low latitude space weather effects in mexico,” *Space Weather*, vol. 22, no. 11, p. e2024SW004111, 2024.

[408] E. Lawrence, C. D. Beggan, G. S. Richardson *et al.*, “The geomagnetic and geoelectric response to the may 2024 geomagnetic storm in the united kingdom,” *Frontiers in Astronomy and Space Sciences*, vol. Volume 12 - 2025, 2025.

[409] D. M. Oliveira, E. Zesta, and D. Nandy, “The 10 october 2024 geomagnetic storm may have caused the premature reentry of a starlink satellite,” *Frontiers in Astronomy and Space Sciences*, vol. Volume 11 - 2024, 2025.

[410] I. Zakharenkova, I. Cherniak, J. J. Braun *et al.*, “Multi-instrument observations of ionospheric super plasma bubbles in the European longitude sector during the 23–24 April 2023 severe geomagnetic storm,” *Journal of Space Weather and Space Climate*, vol. 15, p. 5, Jan. 2025.

[411] R. Hajra, B. T. Tsurutani, Q. Lu *et al.*, “The April 2023 SYM-H = -233 nT Geomagnetic Storm: A Classical Event,” *Journal of Geophysical Research (Space Physics)*, vol. 129, no. 10, p. e2024JA032986, Oct. 2024.

[412] S. Oyama, H. Vanhamäki, L. Cai *et al.*, “Thermospheric wind response to march 2023 storm: Largest wind ever observed with a fabry-perot interferometer in tromsø, norway since 2009,” *Space Weather*, vol. 22, no. 3, p. e2023SW003728, 2024.

[413] G. Nykiel, A. Ferreira, F. Günzkofer *et al.*, “Large-scale traveling ionospheric disturbances over the european sector during the geomagnetic storm on march 23–24, 2023: Energy deposition in the source regions and the propagation characteristics,” *Journal of Geophysical Research: Space Physics*, vol. 129, no. 3, p. e2023JA032145, 2024.

[414] Q. Gan, R. W. Eastes, Y.-J. Wu *et al.*, “Thermospheric responses to the 3 and 4 november 2021 geomagnetic storm during the main and recovery phases as observed by nasa’s gold and icon missions,” *Geophysical Research Letters*, vol. 51, no. 1, p. e2023GL106529, 2024.

[415] A. Sharon, V. Habyarimana, P. Mungufeni *et al.*, “Ground and space-based response of the ionosphere during the geomagnetic storm of 02–06 november 2021 over the low-latitudes across different longitudes,” *Advances in Space Research*, vol. 73, no. 6, pp. 3014–3032, 2024.

[416] C. I. Uga, E. Uluma, B. Adhikari *et al.*, “Impact of the October 28, 2021 Solar Flare and the November 4, 2021 Geomagnetic Storm on the Low, Middle, and High-Latitude Ionosphere,” *Discover Space*, vol. 128, no. 1, p. 4, Dec. 2024.

[417] M. Reznychenko, D. Kotov, O. Bogomaz *et al.*, “Ionospheric response to the february 27, 2023 intense geomagnetic storm over kharkiv and the akademik vernadsky station,” *Ukrainian Antarctic Journal*, vol. 22, no. 1(28), pp. 40–50, Sep. 2024.

[418] T. Li, D. Zheng, C. He *et al.*, “Ionospheric response to the 24–27 february 2023 solar flare and geomagnetic storms over the european region using a machine learning–based tomographic technique,” *Space Weather*, vol. 23, no. 1, p. e2024SW004146, 2025.

[419] P. Baki, B. Rabiu, C. Amory-Mazaudier *et al.*, “The status of space weather infrastructure and research in africa,” *Atmosphere*, vol. 14, no. 12, 2023.